Title
A high-resolution numerical investigation of beach groundwater and swash interactions

Author
Delisle, Marie-Pierre Chloe

Publication Date
2023

Peer reviewed|Thesis/dissertation

UNIVERSITY OF CALIFORNIA

Los Angeles

A high-resolution numerical investigation of beach groundwater and swash interactions

A dissertation submitted in partial satisfaction
of the requirements for the degree
Doctor of Philosophy in Civil Engineering

by

Marie-Pierre Chloe Delisle

2023

ABSTRACT OF THE DISSERTATION

A high-resolution numerical investigation of
beach groundwater and swash interactions

by

Marie-Pierre Chloe Delisle
Doctor of Philosophy in Civil Engineering
University of California, Los Angeles, 2023
Professor Timu Gallien, Chair

Coastal flooding is a growing socioeconomic and humanitarian hazard. Sea level rise will raise beach groundwater levels, potentially inundating low–lying areas from groundwater exposure while simultaneously propagating swash impacts onto higher beach and backshore elevations. Generally, coastal flood modeling efforts characterize only surface flows, neglecting swash zone processes such as infiltration and porous media flow. Swash zone processes are multi-phase, shallow, and transient presenting numerous modeling and observational challenges. In this dissertation, a novel numerical model, SedOlaFlow, is developed by integrating the free-surface resolving Reynolds-averaged Eulerian two-phase sediment transport model, SedWaveFoam, with the surface wave solver, olaFlow, in the OpenFOAM framework. This tightly–coupled, surface–subsurface model enables the direct investigation of interactions between swash surface and subsurface flows and is validated with laboratory flume observations. Swash-groundwater interface dynamics are analyzed to determine the mechanisms modulating the bi-directional swash–beach groundwater relationship. Elevated beach groundwater levels amplify wave runup extent through beach face saturation and turbulence

dampening. Environmental conditions (e.g., beach characteristics, wave conditions) influence the beach groundwater impact on wave runup. The swash–groundwater relationship increases and alters the timing of coastal vulnerability. Sea level rise will further exacerbate coastal flooding impacts through beach groundwater–swash interactions. Inclusion of the swash–groundwater relationship in coastal hazard planning and modeling is fundamental to accurate wave runup predictions and assessment of coastal flooding risk.

The dissertation of Marie-Pierre Chloe Delisle is approved.

Marcelo Chamecki

Scott J. Brandenberg

Steven A. Margulis

Yeulwoo Kim

Timu Gallien, Committee Chair

University of California, Los Angeles

2023

pour Maman et Papa

TABLE OF CONTENTS

LIST OF FIGURES

LIST OF TABLES

ACKNOWLEDGMENTS

This research in this dissertation was partially supported by the California Department of Parks and Recreation Division of Boating and Waterways (C1670006), the US Coastal Research Program (W912HZ-20-200-004), the Barbara Streisand Foundation, the Basic Science Research Program through the National Research Foundation of Korea (NRF) funded by the Ministry of Education (NRF-2021R1F1A1062223), the Robert L. Wiegel Scholarship, and Anchor QEA Scholarship. Numerical simulations presented in this dissertation were carried out using computational and storage services associated with the Hoffman2 Shared Cluster provided by the Institute for Digital Research and Education's Research Technology Group at the University of California, Los Angeles.

This dissertation would not have been possible without my advisor, Professor Timu Gallien, whose passion and enthusiasm for coastal science are contagious. Thank you for taking a chance on a time-starved student-athlete and helping me navigate the complexities of research and life. Your efforts to cultivate an inclusive and collaborative community within the Coastal Flood Lab enabled me to thrive. To my CFL labmates, thank you for sharing this experience with me and bringing a smile to my face even when everything inevitably went wrong during field work.

I have been fortunate to have many mentors in my life, not all of whom can be thanked here. I am immensely grateful to Dr. Nikos Kalligeris and Dr. Yeulwoo Kim, who took me under their wings and empowered me to become an independent researcher. Your guidance and friendship have been integral to my growth and success. I would also like to express my heartfelt appreciation to Scott Shea, for his unwavering support and guidance through life's many obstacles extending far beyond the pool.

There are three teachers that have had a particularly profound impact on my life. Thank you to Mr. Robert Geddes for nurturing my creativity and love for learning; I fondly remember making chocolate-chip banana pancakes to learn division. Mr. Steve Lewis, your

unbounded enthusiasm for teaching infused excitement into the classroom, and I thank you for cultivating my leadership abilities and work ethic. And thank you to Mr. Ron Nicoletti, your encouragement and belief in my abilities inspired me to strive beyond my self-imposed limits without fear.

Joseph – thank you for riding this Ph.D. roller coaster with me; there isn't anyone else I would have wanted to do this with. James – thank you for never letting me lose sight of my goals, encouraging me during setbacks, and being my biggest fan and advocate. Thank you to my siblings – Guillaume, Laurence, and Jérémie – for inspiring and challenging me to be the best version of myself. And finally, thank you Maman et Papa, for stimulating my curiosity, modeling tenacity, and being incredible role models. Your unconditional love is the foundation of all my achievements.

VITA

EDUCATION

University of California, Los Angeles

M.S., Civil & Environmental Engineering 2018 – 2020

B.S., *cum laude*, Civil & Environmental Engineering 2014 – 2018

PUBLICATIONS

Delisle, M.P.C., Kim, Y., & Gallien, T.W. (in prep). Beach groundwater impacts on wave runup: mechanisms and implications. *Journal of Geophysical Research: Oceans.*

Delisle, M.P.C., Kim, Y., & Gallien, T.W. (in revision). A numerical study of swash and beach groundwater interactions. *Journal of Geophysical Research: Oceans*.

Delisle, M.P.C., Kim, Y., & Gallien, T.W. (2023). A numerical study of swash-groundwater interactions using OpenFOAM. *Coastal Sediments 2023: The Proceedings of the Coastal Sediments 2023*. 305-313.

Delisle, M.P.C., Kim, Y., Mieras, R.S., & Gallien, T.W. (2022). Numerical investigation of sheet flow driven by a near-breaking transient wave using SedFoam. *European Journal of Mechanics – B/Fluids*, 96, 51-64.

Brandenberg, S.J., Stewart, J.P., Wang, P., Nweke, C.C., Hudson, K., Goulet, C.A., Meng, X., Davis, C.A., Ahdi, S.K., Hudson, M.B., Donnellan, A., Lyzenga, G., Pierce, M., Wang, J., Winters, M.A., Delisle, M.P.C., Lucey, J., Kim, Y., Gallien, T.W., Lyda, A., Yeung, J.S., Issa, O., Buckreis, T., & Yi, Z. (2020). Ground Deformation Data from GEER Investigations of Ridgecrest Earthquake Sequence. *Seismological Research Letters*, 91(4), 2024-2034.

Winters, M.A., Delisle, M.P.C., Lucey, J.T., Kim, Y., Hudson, K., Liu, Z., Brandenberg, S., & Gallien, T.W. (2019). "UCLA UAV Imaging", in Ridgecrest, CA earthquake sequence, July 4 and 5, 2019. *DesignSafe-CI.*

Gallien, T.W., Kalligeris, N., Delisle, M.P.C., Tang, B.X., Lucey, J.T., & Winters, M.A. (2018). Coastal flood modeling challenges in defended urban backshores. *Geosciences*, 8(12), 450.

INVITED TALKS

Swash-groundwater flow interactions and impacts on wave runup

Woods Hole Oceanographic Institution, Applied Ocean Physics & Engineering, October 28, 2022.

United States Naval Academy, Naval Architecture & Ocean Engineering, February 22, 2023.

SELECTED PRESENTATIONS

Delisle, M.P.C., Kim, Y., Gallien, T.W., A numerical study of swash-groundwater interactions using OpenFOAM. Coastal Sediments, New Orleans, Louisiana, April 12, 2023.

Delisle, M.P.C., Kim, Y., Gallien, T.W., Beach groundwater impacts on wave overtopping flooding. 37th International Conference on Coastal Engineering, Sydney, Australia, December 9, 2022.

Delisle, M.P.C, Kim, Y., Gallien, T.W., A numerical study of swash and beach groundwater interactions. American Geophysical Union Ocean Sciences Meeting, virtual, March 1, 2022.

Delisle, M.P.C, Kim, Y., Mieras, R.S., Gallien, T.W., Investigating sheet flow under a near-breaking transient wave using a two-phase eulerian sediment transport model. Coastal Dynamics 2021 Congress, virtual, June 30, 2021.

TEACHING EXPERIENCE

UCLA Civil & Environmental Engineering

CEE 158/258: Coastal Engineering — Spring 2021, 2022

CEE 129L: Engineering Geomatics — Spring 2020

UCLA Center for Excellence in Engineering and Diversity

E87: Introduction to Engineering Disciplines — Fall 2019

CHAPTER 1

Introduction

1.1 Sea level rise and coastal flooding

Global sea levels are projected to increase by 0.46 to 1.89 m by 2100 (Fox-Kemper et al., 2021), and under medium to medium-high greenhouse-gas emissions scenarios, California's mean sea level is expected to rise by 1.0 to 1.4 m (Heberger et al., 2009; Church et al., 2013). Southern California, in particular, is extremely vulnerable to small changes in sea level. For example, a $\sim$5 cm increase in coastal water levels doubles the odds of the 50-year flooding event (i.e., becomes a 25-year flooding event; Taherkhani et al., 2020). Sea level rise impacts are a fundamental concern in California where coastal resources are central to recreation, economic activity, and culture. Notably, 87% of the state's population (as of 2014) lives in coastal communities (Census, 2015b).

Population densities in coastal regions are significantly higher than in inland areas (Crossett et al., 2013; Neumann et al., 2015). An estimated 10 million people a year were exposed to coastal flooding in the past few decades (Nicholls, 2004); the actual value is likely much higher as significant components (e.g., waves) were not accounted for in this approximation. Population trends forecast that more than one billion people will live in coastal communities by 2050 (Merkens et al., 2016). When projected population growth and coastal migration are accounted for, approximately 4.2 million people in the continental United States will be at risk of inundation with 0.9 m of sea level rise by 2100; the number increases to 13.1 million people if the sea level rises 1.8 m (Hauer et al., 2016).

Sea level rise will substantially increase both the frequency and intensity of extreme coastal events, i.e., energetic waves, high spring tides, storm surge (Cayan et al., 2008; Heberger et al., 2009; Mastrandrea and Luers, 2012). The compounding effects of sea level rise, dynamic water level components, and coastal changes (e.g., beach erosion, cliff retreat) can disproportionately amplify coastal risk and flood extent (Prime et al., 2015; Vitousek et al., 2017). By the end of the 21st century, extreme once-in-a-century sea levels of the recent past are projected to occur 160 – 530 times more frequently (i.e., 1.6 - 5.3 times a year; Fox-Kemper et al., 2021). Coastal processes, especially wave runup and overtopping, have been the focus of numerous regional-scale (or smaller) studies to examine the potential effects of sea level rise on coastal flooding (e.g., Hunter, 2012; Gallien, 2016; Hsu et al., 2017). Wave runup and overtopping have been shown to be more sensitive to sea level rise than tides (Arns et al., 2017), making the understanding of coastal processes of greater concern (Cayan et al., 2008).

Coastal flood assessment and planning typically focus only on overland flow and neglect beach groundwater contributions to coastal flood risk (Rotzoll and Fletcher, 2013). Coastal groundwater levels will increase at approximately the same rate as the sea level (Horn, 2006; Bjerklie et al., 2012; Rotzoll and Fletcher, 2013; Hoover et al., 2017) and rising groundwater levels will inevitably breach submerged infrastructure (i.e., basements, water, sewage, and electricity lines) and pose water management complications. Beach groundwater tables can rise more than 1 m during large wave and surge events (Housego et al., 2021). In especially low-lying coastal communities, groundwater flood damage and emergence is not only possible, but expected (Habel et al., 2017). Notably, including groundwater inundation dynamics in modeling increases flooding extent more than twice, compared to modeling overland, marine flooding alone (Rotzoll and Fletcher, 2013). Improved knowledge of the bi-directional relationship between surface and subsurface flows is fundamental to quantifying and characterizing swash zone response to evolving ocean levels and wave climatology.

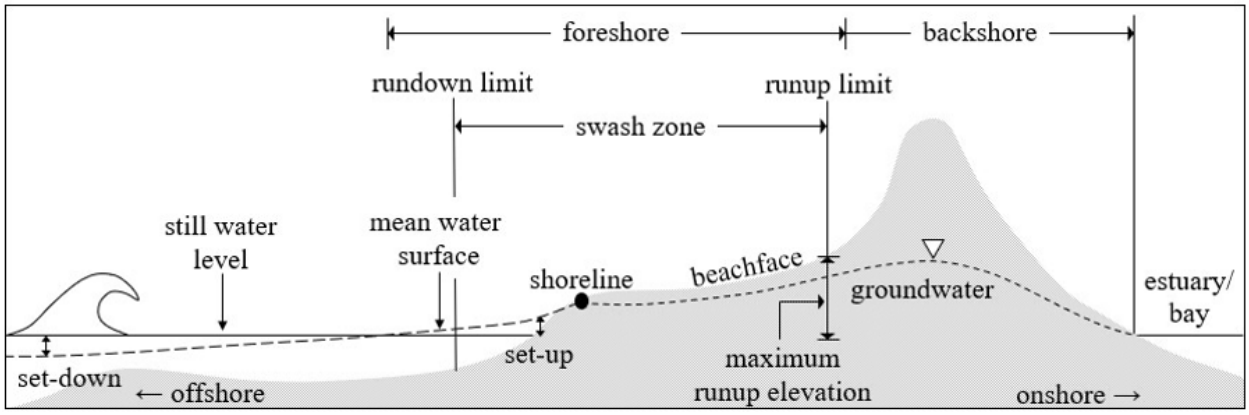

Figure 1.1: Definition sketch of the swash zone.

1.2 Swash zone terminology

Improved understanding of dynamic coastal processes is essential for sea level rise adaptation. The swash zone is the coastal region where the sea meets the land; it is the intermittently wet and dry section of the beach which migrates up and down the beach face over a tidal cycle (Fig. 1.1). Within this zone, the shoreline is the location where the mean water surface (which includes the effects of wave set-down and set-up) meets the beach face and beach groundwater is linked with tidal fluctuations. Swash is the wave-driven flow that initially travels landward as uprush (or runup) along the beach face, reaches its maximum extent, and then returns downslope as backwash (or rundown). The offshore (seaward) and onshore (landward) edges of the swash zone are the minimum rundown and maximum runup limits, respectively. The maximum runup elevation is calculated as the vertical difference between the maximum onshore swash extent (runup limit) and the still water level (i.e., offshore water level). The foreshore is loosely defined as the region bounded by the rundown limit at low tide and the runup limit at high tide; it encompasses the entirety of the moving swash zone. The backshore exists landward of the foreshore and typically only interacts with swash during storm or extreme wave events.

Beneath the swash zone surface, the beach groundwater system is categorized as a shallow,

unconfined aquifer in which tides, waves, and swash are the primary drivers of flow through unsaturated and saturated sediments. The groundwater table, or phreatic surface, is where pore water pressure is equivalent to atmospheric pressure (Fig. 1.2). The saturated (or phreatic) zone exists beneath the groundwater table; all voids are filled with water and pore water pressure increases with depth. The capillary fringe exists immediately above the saturated zone; it is the result of cohesion between water molecules and adhesion of water molecules to the surrounding sediment (Price, 1996). The vertical extent of the capillary fringe generally increases as sediment size decreases and can vary greatly in thickness from a few millimeters to meters, even extending all the way to the beach face (Horn, 2002). All pore spaces within the capillary fringe are saturated, however unlike the saturated zone, the pore water pressure is less than atmospheric. The region extending from the capillary fringe to the beach face is the unsaturated (or vadose) zone where voids are filled with primarily air and pore water pressure is less than atmospheric. Hydrodynamic forces (e.g., swash, tides, rainfall) and beach sediment characteristics (e.g., size, shape, porosity, hydraulic conductivity) largely determine the elevation of the beach groundwater table (Gourlay, 1992). The beach groundwater table oscillates in response to both low-frequency (e.g., tide, storm surge) and high-frequency (e.g., individual swash events) fluctuations and is generally not flat. The beach groundwater elevation generally decreases with distance from the shoreline (Rotzoll and El-Kadi, 2008; Housego et al., 2021). In regions where the backshore is a body of water (e.g., bay or estuary backed beaches, sand spits, barrier islands), the groundwater table is constrained to connect with the backshore surface water elevation (as shown in Fig. 1.1). Tidally-induced beach-groundwater variation is typically time-skewed; infiltration occurs abruptly as the tide rises followed by significantly lagged exfiltration (i.e., rate of groundwater rise significantly exceeds rate of decline; Nielsen, 1990). Overheight of the beach groundwater table above tidal elevations can occur due to hydrologic infiltration or tidal variation (e.g., Kang et al., 1995; Turner et al., 1997a). In low-lying areas, groundwater table overheight caused by energetic wave overtopping events may migrate landward and seep

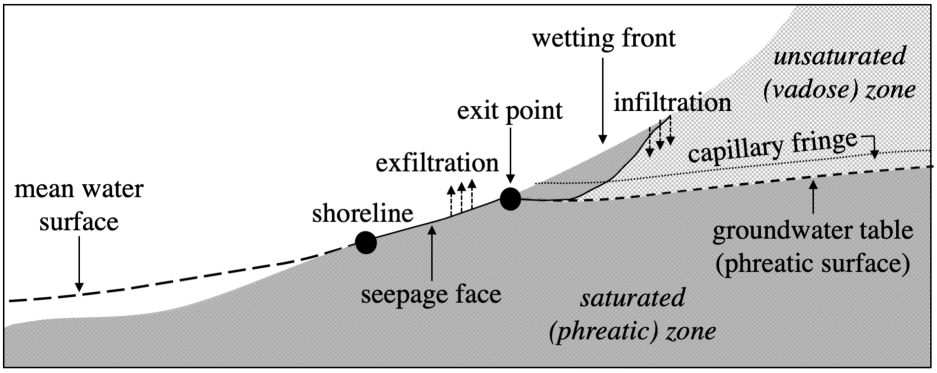

Figure 1.2: Definition sketch of the beach groundwater system when the mean water surface is decoupled from the groundwater table.

out the backshore causing significant damage to subterranean infrastructure (Ludka et al., 2018). While the beach groundwater table is generally considered an extension of the mean water surface, decoupling between the the ocean and beach groundwater occurs when the tide falls faster than the beach exfiltration rate (Steenhauer et al., 2011; Heiss et al., 2015). When this happens, a seepage face develops along the beach face and the groundwater table exit point is above the mean water surface. Until sufficient beach face exfiltration occurs or the exit point is overtaken by a rising tide, the discontinuity between the ocean surface and beach groundwater table will exist. When the exit point is equivalent to the shoreline or when runup surpasses the seepage face, swash infiltration creates a wetting front that may cause air to become entrapped between the wetting front and groundwater table.

1.3 Swash zone hydrodynamics

The surface-subsurface dynamics occurring in the swash zone create a highly complex region characterized by multi-phase, transient, and interdependent processes. Swash zone hydrodynamics consist of three primary components: surface flows, surface-subsurface flow interactions, and beach groundwater. Surface flow behavior is largely the result of offshore conditions (e.g., wave height/frequency/shape, currents) and beach attributes (e.g., slope,

sediment composition, permeability; e.g., Waddell, 1976; Elfrink and Baldock, 2002; Ruggiero et al., 2004; Bakhtyar et al., 2009; Heiss et al., 2014). Swash is typically generated by both non-breaking standing waves at infragravity frequencies and high-frequency broken waves (i.e., bores) that collapse at the shoreline (e.g., Waddell, 1976; Hibberd and Peregrine, 1979; Packwood, 1983; Raubenheimer and Guza, 1996; Madsen et al., 1997; Baldock and Holmes, 1999). Swash evolution is therefore dependent on the inundation intermittency of standing waves and bores, as well as the interaction between successive swash events (e.g., Jackson et al., 2004; Brocchini and Dodd, 2008). Swash merging occurs if a larger swash event captures a proceeding uprush (i.e., overtakes) or if backwash from a larger swash event inhibits uprush from a successive, wave (i.e., absorption; Kubota et al., 1993). Rapidly varying depths and velocities characteristic of the swash zone lead to difficulty in measuring and quantifying swash zone dynamics (Elfrink and Baldock, 2002; Puleo et al., 2012). Infragravity-induced swash velocities are near-symmetric relative to maximum runup whereas bore-driven swash exhibits rapid acceleration during uprush that creates diverging flow (e.g., Hibberd and Peregrine, 1979; Masselink and Hughes, 1998). Supercritical flow during backwash, however, is a feature of both infragravity and bore-driven swash motions (Elfrink and Baldock, 2002). While largely influenced by offshore and beach conditions, the behavior and magnitude of surface swash flows is intrinsically linked to the beach groundwater system through infiltration/exfiltration processes.

A key characteristic of the swash zone is the exchange of water between the surface and subsurface through infiltration/exfiltration. Swash infiltration and exfiltration depend on a variety of beach and hydrodynamic factors (e.g., Duncan, 1964; Packwood, 1983; Gourlay, 1992; Turner and Nielsen, 1997; Bakhtyar et al., 2011; Heiss et al., 2014). Swash zone infiltration/exfiltration research has primarily focused on characterizing and quantifying sediment transport impacts (e.g., Bagnold, 1940; Duncan, 1964; Harrison, 1969; Waddell, 1976; Packwood, 1983; Turner, 1993; Turner and Nielsen, 1997; Turner and Masselink, 1998; Butt et al., 2001; Nielsen et al., 2001; Austin and Masselink, 2006a; Masselink and Turner, 2012; Jamal

et al., 2014). Infiltration (exfiltration) in the swash zone causes vertical fluid drag that alters the effective weight of surface sediment and stabilizes (destabilizes) the bed (e.g., Martin and Aral, 1971; Nielsen, 1992; Baldock and Holmes, 1999; Nielsen et al., 2001). When air becomes entrapped between the infiltrating wetting front and the beach groundwater table, infiltration is reduced (Horn, 2002, 2006; Steenhauer et al., 2011). Boundary layer thinning (thickening) due to infiltration (exfiltration) leads to increased (decreased) bed shear stress (Conley and Inman, 1994; Turner and Masselink, 1998; Puleo and Holland, 2001; Pintado-Patiño et al., 2015). Experimental studies on the influence of infiltration/exfiltration on sediment transport have demonstrated conflicting results, likely because the effects of vertical fluid drag and boundary layer thinning oppose one another (Nielsen et al., 2001). Infiltration reduces runup and must be considered to accurately reproduce swash observations (Pintado-Patiño et al., 2015). Infiltration, exfiltration, and beach characteristics significantly impact boundary layer dynamics and runup, but the role and relative dominance of these processes is uncertain (Horn, 2006; McCall et al., 2012; Jamal et al., 2014; Briganti et al., 2016).

Infiltration and exfiltration rates on a beach are largely determined by the swash flow and sediment characteristics, however a growing body of research suggests that the beach groundwater table is critically important (e.g., Gillham, 1984; Turner, 1993; Masselink and Li, 2001; Bakhtyar et al., 2011; Masselink and Turner, 2012; Rotzoll and Fletcher, 2013; Sous et al., 2013; Befus et al., 2020). A shallow (deep) groundwater table lends to exfiltration (infiltration) and promotes erosion/offshore (accretion/onshore) sediment transport (e.g., Bagnold, 1940; Turner and Masselink, 1998; Baldock and Holmes, 1999; Masselink and Li, 2001; Bakhtyar et al., 2011). The capillary fringe impacts groundwater table oscillations over a range of frequencies, including those of wave and tidal fluctuations (Waddell, 1976; Turner and Nielsen, 1997; Nielsen and Perrochet, 2000; Werner and Lockington, 2003; Horn, 2006). A capillary fringe limits beach groundwater storage capacity and can cause a disproportionate and near-instantaneous groundwater table response to infiltration in cases where the capillary fringe reaches the surface (i.e., reverse Wieringermeer effect; Gillham, 1984; Turner, 1993).

Models that do not characterize groundwater and capillarity over-estimate infiltration, which in turn may lead to the misrepresentation and underprediction of swash runup (Li et al., 1999; Pintado-Patiño et al., 2015).

1.4 Swash zone numerical modeling

The swash zone is a region of critical importance as swash processes control final wave energy dissipation, beach morphology (e.g., erosion, accretion), and play a significant role in coastal flooding (Elfrink and Baldock, 2002; Larson et al., 2004; Horn, 2006; Bakhtyar et al., 2009; Chardón-Maldonado et al., 2016; Ruessink et al., 2016; Habel et al., 2017; Dalya et al., 2021). However most coastal hazard models (i.e., flooding, erosion) do not explicitly consider swash-zone flows due to the complexity of the region (e.g., Hubbard and Dodd, 2002; Hunt, 2005; Brown et al., 2007; Gallien, 2016). Swash zone modeling poses significant challenges including: (1) a moving land-water boundary, (2) shallow, high velocity, rapidly varying flow, (3) sediment motion, (4) infiltration/exfiltration, and (5) process time scales ranging from fractions of seconds to days (Hughes and Turner, 1999; Horn, 2002). The difficulty in modeling discontinuous swash zone mechanisms frequently results in simplifying assumptions such as neglecting the two-way feedback between surface flows and beach groundwater.

1.4.1 Surface flows

Low and high-frequency waves that develop in the nearshore are a driving force in the swash zone. A popular nearshore surface flow modeling method relies on the Non-Linear Shallow Water (NLSW) equations, a depth-integrated, wave-resolving method that assumes viscosity and vertical velocities are negligible (i.e., vertical pressure distribution is hydrostatic). Nearshore numerical modeling based on the NLSW equations have successfully reproduced swash motions, runup, overtopping, and coastal flooding (e.g., Hibberd and Peregrine, 1979; Titov and Synolakis, 1995; Dodd, 1998; Hu et al., 2000; Hubbard and Dodd, 2002; Shi-

ach et al., 2004; Brocchini and Dodd, 2008; Gallien, 2016). More recently, a number of nonhydrodstatic NLSW models have been developed. XBeach (Roelvink et al., 2009), a hydro-morphodynamic model is based on the NLSW equations and may be run in either a hydrostatic mode to model infragravity and sediment transport or alternatively, in non-hydrostatic mode, where individual wave may be simulated. XBeach has been widely used to predict storm-induced overtopping and erosion (e.g., Roelvink et al., 2009; McCall et al., 2010, 2012; Elsayed and Oumeraci, 2016; Gallien, 2016). SWASH (Zijlema et al., 2011) partitions flow in multiple layers to account for vertical flow and allow intermediate depth boundaries (water depth to wavelength ratio up to $\sim$2.6) and is commonly used to model wave overtopping (e.g., Smit et al., 2014; Suzuki et al., 2017; Fiedler et al., 2018). NLSW models are generally capable of predicting wave overtopping processes, however, cannot resolve boundary layer processes critical to the accurately characterizing surface-subsurface beach face exchange.

The classical Boussinesq equations, originally developed by Peregrine (1967), represent an alternative depth-integrated, wave-resolving method widely used to model nearshore surface flows. Initially, Boussinesq models were reliable only offshore of the swash zone in intermediate depths prior to wave-breaking. Boussinesq models provide an improvement over the NLSW equations in that frequency dispersion at intermediate depths is preserved. However, Boussinesq models are limited by their inability to realistically simulate wave-breaking. The Boussinesq approach has since been extended to allow accurate simulation of surface flow into both deep water and the swash zone (e.g., Madsen et al., 1991; Nwogu, 1993; Beji and Nadaoka, 1996; Kennedy et al., 2000; Madsen et al., 2002; Lynett, 2006; Tissier et al., 2012). Boussinesq-type models are an attractive approach to simulate dispersive waves, however they omit or idealize swash zone processes (e.g., wave breaking) and other approaches may be more advantageous. A hybrid approach copuling Boussinesq-type and NLSW models is growing more common (e.g., Watson et al., 1995; Stansby, 2003; Tonelli and Petti, 2009; Shi et al., 2012; Tonelli and Petti, 2012; Orszaghova et al., 2012). However, the NLSW limita-

tions still exist and important small-scale bottom boundary layer (BBL) processes cannot be resolved.

The Navier-Stokes equations provide a detailed and accurate description of flow structure, regardless of water depth. Unlike the NLSW or Boussinesq equations, depth-resolving Navier-Stokes approaches impose no limiting vertical flow assumptions. Navier-Stokes based approaches can accurately simulate both bulk flow characteristics and small-scale swash dynamics including wave breaking, runup, and boundary layer processes (e.g., Lin and Liu, 1998b; Watanabe and Saeki, 1999; Zhao and Tanimoto, 1999; Christensen and Deigaard, 2001; Puleo et al., 2002; Dalrymple and Rogers, 2006; Bakhtyar et al., 2009; Kim et al., 2017). Another advantage of Navier-Stokes models is the ability to include turbulence, critical to accurately describe swash zone kinematics (Hughes et al., 1997). In the Lagrangian framework, Smooth Particle Hydrodynamics (SPH) methods to approximate the Navier-Stokes equations based on a set of moving particles have gained traction as they are mesh-less and require no special surface tracking (Dalrymple and Rogers, 2006). SPH methods show good (though limited) agreement with observations (e.g., Shao et al., 2006; Khayyer et al., 2008), however their extraordinary computational demands render them impractical for swash zone numerical modeling. Similarly, Direct Numerical Simulation (DNS) methods, which resolve all scales of motion, are currently only feasible for laminar flows due to high computational demand. Large Eddy Simulation (LES) methods model nearly all but the smallest turbulence eddies, and have shown success in swash zone modeling (e.g., Watanabe and Saeki, 1999; Zhao and Tanimoto, 1999; Christensen and Deigaard, 2001; Puleo et al., 2002; Kim et al., 2017). However, LES turbulence closure is sensitive to grid sizing and a grid-independent solution may be difficult to obtain.

Reynolds-Averaged Navier-Stokes (RANS) methods describe the average motion of flow and turbulence through the computation of Reynolds stresses and are widely used in swash zone modeling (e.g., Lin and Liu, 1998b; Puleo et al., 2007; Zhang and Liu, 2008; Bakhtyar et al., 2009; Torres-Freyermuth et al., 2013; Pintado-Patiño et al., 2015). RANS meth-

ods are more computationally efficient than SPH, DNS, or LES methods because only mean turbulence characteristics are described rather than directly calculated. Notably, high-resolution RANS methods can still sufficiently resolve boundary layer processes (e.g., Torres-Freyermuth et al., 2013; Briganti et al., 2016; Cheng et al., 2017). COBRAS (Cornell Breaking Waves and Structures; Lin and Liu, 1998b,a) is a RANS model with k-ε turbulence closure that has been extended and validated to a variety of swash zone applications (e.g., Lin et al., 1999; Liu et al., 1999; Hsu et al., 2002; Amoudry et al., 2008; Zhang and Liu, 2008; Pintado-Patiño et al., 2015). The computational fluid dynamics toolbox OpenFOAM provides a framework to solve the Navier-Stokes equations and apply the volume-of-fluid method to determine the free water surface (Hirt and Nichols, 1981). OpenFOAM has been widely applied to coastal problems as it is a modular framework that includes a variety of hydrodynamic solvers and turbulence models (e.g., Jacobsen et al., 2012; Higuera et al., 2013; Chen et al., 2014; Cheng et al., 2017; Kim et al., 2019).

1.4.2 Subsurface flows

Numerical modeling of the beach groundwater system requires consideration of tidal and wave forcings, capillarity, and infiltration/exfiltration. For an unconfined, homogenous, and isotropic aquifer, Darcy's Law governs the rate of subsurface flow. In combination with mass conservation, the general Boussinesq equation for groundwater flow through a porous medium is defined. The main assumptions embedded in the Boussinesq equation are that flow is saturated and laminar (i.e., Darcy's Law is valid) and that horizontal flow dominates over vertical flow (i.e., the Dupuit-Forcheimer approximation is valid). Boussinesq-type equations are commonly used in beach groundwater models and have been shown to be sufficient in describing the groundwater table response to tidal forcing (e.g., Dominick et al., 1971; Kang and Nielsen, 1997; Baird et al., 1998; Raubenheimer et al., 1999). However, the beach groundwater system includes both unsaturated and saturated zones and vertical and horizontal flows can be of similar magnitude (i.e., nonhydrostatic conditions exist; Robinson

et al., 2006). When wave forcing is important, (i.e., in the swash zone), using the Boussinesq equation for beach groundwater flow leads to the underprediction of groundwater table elevations (e.g., Dominick et al., 1971; Baird et al., 1998; Raubenheimer et al., 1999). Nielsen et al. (1997) derived an analytical solution to the second order Bousinessq equation to describe the periodic groundwater table, but results deviated from experimental data. Nielsen (1988) simulated the beach groundwater table response to wave fluctuations by including a term representing the swash infiltration/exfiltration velocity per unit area. Without the Dupuit-Forcheimer assumption of hydrostatic pressure, the groundwater Boussinesq equation becomes the Laplace equation. The Laplace equation provides small improvements over the Boussinesq equation, however it is still typically limited to saturated flow. Li et al. (1997) developed a boundary element model to solve the Laplace equation that incorporates the effects of swash flows on groundwater through a modified kinematic boundary condition. Model results were qualitatively compared to experimental data however Li et al. (1997) indicated that qualitative analysis is necessary to fully validate the model.

Capillarity is not represented in either the Boussinesq or Laplace groundwater equations. Parlange and Brutsaert (1987) modified the groundwater Boussinesq equation using the Green and Ampt equation (Green and Ampt, 1911) to account for capillarity. This simplified infiltration model assumes a completely saturated capillary fringe with a constant suction head at the capillary fringe surface. The Green and Ampt equation presents an idealized capillary fringe formulation, but still provides improvement over the groundwater models neglecting capillary effects altogether. The Laplace equation was modified to include capillary effects on saturated flow and demonstrated good agreement with analytical predictions and experimental data (e.g., Li et al., 1997; Li and Barry, 2000). The inclusion of capillarity in modeling is critical to accurately reproduce high-frequency oscillations observed in beach groundwater tables (Barry et al., 1996; Li et al., 1997). Resolving the variably saturated beach groundwater system while concurrently incorporating swash zone transient boundary conditions remains a numerical modeling challenge.

1.4.3 Coupled surface-subsurface flows

To model the entirety of the swash zone, vertical flow between swash and the beach groundwater table must be included (e.g., Elfrink and Baldock, 2002). The phase-resolving numerical model BeachWin (Li et al., 1997, 2002) simulates the effect of wave motion on groundwater flow using the NLSW equations for surface flow and the Laplace equation or groundwater flow. The model is able to reproduce high-frequency water table fluctuations but is limited in that only saturated groundwater flow is considered. Similarly, Perera et al. (2019) weakly coupled the NLSW and Laplace equations for surface and subsurface flow, respectively; the model agreed reasonably well with experimental groundwater table elevations, however infiltration effects on the BBL could not be resolved. Desombre et al. (2012) simulated flow through a beach using the RANS equations for surface flow and the Darcy-Brinkman-Forcheimer formulation for groundwater flow however, capillarity was neglected and only the main subsurface flow characteristics were reasonably reproduced. Bakhtyar et al. (2011) loosely coupled the Navier-Stokes equations for surface flow with a groundwater flow model based on SEAWAT-2000 (Guo and Langevin, 2002); differences between the numerical model and experimental data were attributed to the simulation not including the capillary fringe. The volume-averaged RANS model COBRAS was extended by Hsu et al. (2002) to include both surface and subsurface flow; porous flow is characterized with the semi-empirical Forcheimer equation. Pintado-Patiño et al. (2015) showed that modified COBRAS is capable of simulating the influence of beach permeability and porosity on swash infiltration/exfiltration, however it does not fully represent groundwater flow phenomena. Several OpenFOAM solvers can simulate free surface water waves over porous media using the volume of fluid approach (e.g., olaFlow (Higuera et al., 2013), waves2Foam (Jacobsen et al., 2012)); these models rely on porosity to simplify subsurface flow processes and cannot capture the complete influence of sediment on surface-subsurface exchange. Two-phase models that can explicitly model high-frequency free-surface fluctuations, directly account for sediment, and include bi-directional surface-subsurface feedback are necessary to accurately

replicate swash-groundwater interactions in the swash zone.

1.5 Objective of the dissertation

Comprehensive investigation of beach infiltration/exfiltration processes is a critical research need to improve the characterization, quantification, and understanding of swash zone behavior (Horn, 2006; Heiss et al., 2014; Elko et al., 2015; Chardón-Maldonado et al., 2016; Perera et al., 2019). Significant research efforts have focused on swash zone processes but are either limited to surface flows, consider only a one-way impact of surface flows on subsurface behavior, and/or make limiting assumptions and simplifications that prevent an accurate physical understanding of swash zone surface-subsurface interactions. Considering that (1) beach groundwater levels will rise with the sea level (e.g., Rotzoll and Fletcher, 2013; Hoover et al., 2017), (2) swash infiltration decreases as groundwater levels increase (Bakhtyar et al., 2011), and (3) swash infiltration reduces maximum runup extent (i.e., runup extent increases as infiltration decreases; Bakhtyar et al., 2011; Pintado-Patiño et al., 2015), the potential impacts of shoaling beach groundwater on swash flows and coastal flooding are an urgent concern.

Significant progress has been made in understanding infiltration/exfiltration impacts on sediment transport, BBL, and beach groundwater dynamics. Critically however, the fundamental question of how beach groundwater dynamics influence swash flows (i.e., runup, overtopping) remains unanswered. Investigating the bi-directional relationship between swash zone processes and beach groundwater is of critical importance to improve our understanding and prediction of coastal flooding processes, especially in the context of sea level rise. The objective of this dissertation is to address this fundamental knowledge gap through:

1. Numerical modeling and validation of multi-phase swash zone models
2. Developing and validating a tightly-coupled, surface-subsurface numerical model

3. Characterizing and quantifying the impact of antecedent beach groundwater levels on runup

4. Determining the fundamental physical processes influencing the bi-directional relationship between swash and beach groundwater flows

1.6 Organization of the dissertation

This dissertation is organized into 6 Chapters. Chapter 1 presents the motivation, background, and objectives for this work. Numerical modeling methodology, including a description of a newly developed model for surface and subsurface flows in the swash zone, called SedOlaFlow, is described in Chapter 2 (adapted from Delisle et al. (2022) and Delisle et al. (in revision)). Chapter 3 investigates sediment transport driven by sheet flow under a transient wave using SedFoam (adapted from Delisle et al. (2022)). SedOlaFlow is applied to a dam-break driven swash event in Chapter 4 to examine the impact of antecedent beach groundwater levels on swash (adapted from Delisle et al. (in revision)). Chapter 5 analyzes the fundamental physics controlling the bi-directional relationship between swash and beach groundwater using SedOlaFlow. Concluding remarks and future work are provided in Chapter 6.

CHAPTER 2

Multi-phase Eulerian models

2.1 SedFoam

Based on a two-phase flow approach where sediment is modeled as a continuum, the sediment transport model, SedFoam (e.g., Cheng et al., 2017; Chauchat et al., 2017; Mathieu et al., 2019), concurrently resolves the full profiles of bottom boundary layer (BBL) flow and sediment transport processes without the conventional bedload and suspended load assumptions of single-phase models. SedFoam does not model the free surface or include the air phase. Although continuum models are more limited than particle-based models such as smoothed-particle hydrodynamics (SPH) or the discrete element method (DEM), Reynolds-Averaged Navier-Stokes (RANS) models have been shown to sufficiently resolve boundary layer processes without the extraordinary computational burden of particle methods (e.g., Torres-Freyermuth et al., 2013; Briganti et al., 2016; Cheng et al., 2017; Chauchat, 2018).

2.1.1 Governing equations

Based on the Eulerian two-phase flow equations, the Reynolds-averaged mass conservation equations for fluid (superscript "f") and sediment (superscript "s") phases are written as:

$$\frac{\partial \phi^f}{\partial t} + \frac{\partial \phi^f u_i^f}{\partial x_i} = 0, \tag{2.1}$$

$$\frac{\partial \phi^s}{\partial t} + \frac{\partial \phi^s u_i^s}{\partial x_i} = 0, \tag{2.2}$$

where u is the velocity and ϕ is the volumetric concentration of each phase. Total mass conservation requires $\phi^f + \phi^s = 1$. A subscript, i, represents streamwise ($i = 1$) and vertical ($i = 2$) components, respectively. The Reynolds-averaged momentum equations for fluid and sediment phases are expressed as:

$$\frac{\partial \rho^f \phi^f u_i^f}{\partial t} + \frac{\partial \rho^f \phi^f u_i^f u_j^f}{\partial x_j} = -\phi^f \frac{\partial p^f}{\partial x_i} + \phi^f f_i + \phi^f \rho^f g \delta_{i3} + \frac{\partial \tau_{ij}^f}{\partial x_j} + M_i^{fs}, \tag{2.3}$$

$$\frac{\partial \rho^s \phi^s u_i^s}{\partial t} + \frac{\partial \rho^s \phi^s u_i^s u_j^s}{\partial x_j} = -\phi^s \frac{\partial p^f}{\partial x_i} + \phi^s f_i + \phi^s \rho^s g \delta_{i3} - \frac{\partial p^s}{\partial x_i} + \frac{\partial \tau_{ij}^s}{\partial x_j} + M_i^{sf}, \tag{2.4}$$

where p^f is the fluid pressure and f_i is the external pressure gradient that drives the flow. The fluid and sediment density are $\rho^f = 1{,}000$ kg/m^3 and $\rho^s = 2{,}650$ kg/m^3, respectively. The variable $g = 9.81$ m/s^2 is gravitational acceleration and δ_{i2} is the Dirac delta function. The fluid stress, τ_{ij}^f, includes grain-scale viscous stress and turbulent Reynolds stress calculated with a two-equation k-ε turbulence model (see Section 2.1.1.1). The particle pressure, p^s, and particle shear stress, τ_{ij}^s, are modeled with the kinetic theory of granular flow (Jenkins and Savage, 1983; Ding and Gidaspow, 1990) and a phenomenological closure of frictional contact stresses (Johnson and Jackson, 1987) (see Section 2.1.1.2). The inter-phase momentum transfer between the fluid and sediment phases follows Newton's 3rd Law, $M_i^{fs} = -M_i^{sf}$, and is defined as (Cheng et al., 2017):

$$M_i^{fs} = -\phi^s \phi^f K(u_i^f - u_i^s) + K\phi^f \frac{\nu^{ft}}{\sigma_c} \frac{\partial \phi^s}{\partial x_i}, \tag{2.5}$$

where K is the drag parameter. The first term in Eq. (2.5) represents the Reynolds-averaged drag force resulting from the mean velocity difference and the second term represents fluid turbulent suspension, or drift velocity (Simonin, 1991). The turbulent viscosity of the fluid phase, ν^{ft}, is calculated via turbulence closure (see Section 2.1.1.1) and $\sigma_c = 1.0$ is the Schmidt number. The Schmidt number is not well defined for non-dilute conditions; a value of unity is adopted following Cheng et al. (2017). K is calculated as (Ding and Gidaspow,

1990):

$$K = \left\{ \begin{array}{ll} \dfrac{\alpha\phi^s\nu^f\rho^f}{\phi^f d^2} + \dfrac{\beta\rho^f|u^f - u^s|}{d}, & \phi^s \geq 0.2 \\ \dfrac{0.75C_d\rho^f|u^f - u^s|(\phi^f)^{-1.65}}{d}, & \phi^s < 0.2 \end{array} \right\}, \tag{2.6}$$

where the kinematic viscosity is $\nu^f = 10^{-6}\ m^2/s$, $\alpha = 150$ and $\beta = 1.75$ are chosen as the Darcy-Forchheimer drag coefficients, and d is the sediment diameter. The drag coefficient C_d is calculated as:

$$C_d = \left\{ \begin{array}{ll} \dfrac{24(1 + 0.15Re_p^{0.687})}{Re_p}, & Re_p \leq 1000 \\ 0.44, & Re_p > 1000 \end{array} \right\}, \tag{2.7}$$

and the particle Reynolds number is $Re_p = \phi^s|u^f - u^s|d/\nu^f$.

2.1.1.1 Fluid turbulence closures

The k-ε turbulence model described by Hsu et al. (2004) and Yu et al. (2010) is used as the basis for fluid turbulence closure in this study. The modified k-ε turbulence model accounts for the presence of dispersed particles in two-phase flow and is expected to provide improvements in predicting sediment suspension over a wide range of sediment types (Kranenburg et al., 2014). The fluid stress, τ_{ij}^f, in Eq. (2.3) is composed of large-scale Reynolds stress, R_{ij}^{ft}, and grain-scale stress, r_{ij}^f, the latter of which includes viscous stress. The total fluid stress is written as:

$$\tau_{ij}^f = R_{ij}^{ft} + r_{if}^f = \rho^f\phi^f[2(\nu^{ft} + \nu^f)S_{ij}^f - \frac{2}{3}k^f\delta_{ij}], \tag{2.8}$$

where ν^{ft} is calculated as:

$$\nu^{ft} = C_\mu\frac{(k^f)^2}{\varepsilon^f}. \tag{2.9}$$

The empirical coefficient $C_\mu = 0.09$ is consistent with standard clear fluid flow modeling, k^f is the fluid turbulent kinetic energy (TKE), and ε^f is the turbulent dissipation rate. The

deviatoric part of the fluid phase strain rate, S_{ij}^f, is defined as:

$$S_{ij}^f = \frac{1}{2}(\frac{\partial u_i^f}{\partial x_j} + \frac{\partial u_j^f}{\partial x_i}) - \frac{1}{3}\frac{\partial u_k^f}{\partial x_k}\delta_{ij}. \tag{2.10}$$

Fluid TKE is calculated by the balance equation for sand particles in water (Yu et al., 2010) as:

$$\frac{\partial k^f}{\partial t} + u_j^f\frac{\partial k^f}{\partial x_j} = \frac{R_{ij}^{ft}}{\rho^f}\frac{\partial u_i^f}{\partial x_j} + \frac{\partial}{\partial x_j}[(v^f + \frac{v^{ft}}{\sigma_k})\frac{\partial k^f}{\partial x_j}] \\ - \varepsilon^f - \frac{2\beta(1-\alpha_c)\phi^s k^f}{\rho^f\phi^f} - \frac{1}{\phi^f}\frac{v^{ft}}{\sigma_c}\frac{\partial \phi^s}{\partial x_j}(s-1)g\delta_{j2}, \tag{2.11}$$

where $\sigma_k = 1.0$ is the Schmidt number for TKE (e.g., Rodi, 1993) and $s = \rho^s/\rho^f$ is the specific gravity of the sediment. TKE attenuation due to particle inertial (f_i) and buoyancy (f_b) effects are represented in the fourth and last terms on the right-hand side of Eq. (2.11), respectively. The particle-fluid correlation variable, α_c, represents the level of correlation between fluid and sediment velocity fluctuations and is calculated as (Danon et al., 1977; Chen and Wood, 1985):

$$\alpha_c = e^{-B\cdot St}, \tag{2.12}$$

where $St = t_p/t_l$ is the Stokes number defined by the particle response time, $t_p = \rho^s/\beta$, and the characteristic timescale of energetic eddies, $t_l = k^f/(6\cdot\varepsilon^f)$ (Cheng et al., 2017). An empirical coefficient, $B = 0.16$, is obtained from Kim et al. (2018, 2019).

The balance equation for the turbulent dissipation rate, ε^f, is written as:

$$\frac{\partial \varepsilon^f}{\partial t} + u_j^f\frac{\partial \varepsilon^f}{\partial x_j} = C_{1\varepsilon}\frac{\varepsilon^f}{k^f}\frac{R_{ij}^{ft}}{\rho^f}\frac{\partial u_i^f}{\partial x_j} + \frac{\partial}{\partial x_j}[(v^f + \frac{v^{ft}}{\sigma_\varepsilon})\frac{\partial \varepsilon^f}{\partial x_j}] - C_{2\varepsilon}\frac{\varepsilon^f}{k^f}\varepsilon^f \\ - C_{3\varepsilon}\frac{\varepsilon^f}{k^f}\frac{2\beta(1-\alpha_c)\phi^s k^f}{\rho^f\phi^f} - C_{4\varepsilon}\frac{\varepsilon^f}{k^f}\frac{1}{\phi^f}\frac{v^{ft}}{\sigma_c}\frac{\partial \phi^s}{\partial x_j}(s-1)g\delta_{j2}, \tag{2.13}$$

where $\sigma_\varepsilon = 1$ (Rodi, 1993) and the empirical coefficients are selected as $C_{1\varepsilon} = 1.44$, $C_{2\varepsilon} = 1.92$, $C_{3\varepsilon} = 1.2$, and $C_{4\varepsilon} = 0$ for stable density stratification or $C_{4\varepsilon} = 1$ for unstable density stratification (Cheng et al., 2017). Similar to Eq. (2.11), damping effects due to particle inertia and buoyancy effects resulting from density stratification are represented in the fourth and last term on the right-hand side of Eq. (2.13).

2.1.1.2 Particle stress closures

Particle stresses are induced by intermittent collision and enduring contact/frictional forces. In concentrated regions of sediment transport, momentum exchanges exert dispersive stresses on a collection of particles; the particle stresses can be split into the particle pressure, p^s, and the particle shear stress, τ_{ij}^s. Following Hsu et al. (2004), the particle pressure and shear stress each consist of the collisional component (superscript "sc") (Jenkins and Savage, 1983; Ding and Gidaspow, 1990) and the frictional contact component (superscript "sf"), written in component form as (Johnson and Jackson, 1987):

$$p^s = p^{sc} + p^{sf}, \tag{2.14}$$

$$\tau_{ij}^s = \tau_{ij}^{sc} + \tau_{ij}^{sf}. \tag{2.15}$$

The collisional-kinetic components of both particle pressure, p^{sc}, and particle shear stress, τ_{ij}^{sc}, are modeled by the granular temperature obtained from the kinetic theory of granular flow (Jenkins and Savage, 1983; Ding and Gidaspow, 1990):

$$p^{sc} = p^s \phi^s \left[1 + 2\left(1 + e\right) g_{s0}\right] \Theta \tag{2.16}$$

$$\tau_{ij}^{sc} = 2\mu^{sc} S_{ij}^s + \lambda \frac{\partial u_k^s}{\partial x_k} \delta_{ij} \tag{2.17}$$

where e is the restitution coefficient and g_{s0} is the radial distribution function (Carnahan and Starling, 1969). The balance equation for granular temperature, Θ, accounts for inelastic collision and particle-induced fluctuations that cause advection, diffusion, shear production, and dissipation (Ding and Gidaspow, 1990; Cheng et al., 2017). The particle shear viscosity, μ^{sc}, and bulk viscosity, λ, are functions of Θ and calculated by kinetic theory (Gidaspow, 1994). The deviatoric part of the sediment phase strain rate, S_{ij}^s, is defined as:

$$S_{ij}^s = \frac{1}{2}\left(\frac{\partial u_i^s}{\partial x_j} + \frac{\partial u_j^s}{\partial x_i}\right) - \frac{1}{3}\frac{\partial u_k^s}{\partial x_k}\delta_{ij}. \tag{2.18}$$

In low to moderate sediment concentration ($\phi^s \lesssim 8\%$), binary collisions dominate intergranular interactions. Under high sediment concentrations, enduring contact/frictional

forces are the primary contributor to particle pressure/shear stress and the granular temperature decreases. In these regions of high sediment concentration, a phenomenological closure is implemented for the frictional contact components of particle pressure, p^{sf}, and particle shear stress, τ_{ij}^{sf}, following Johnson and Jackson (1987):

$$p^{sf} = \left\{ \begin{array}{rl} 0, & \phi^s < \phi_f^s \\ F\frac{\left(\phi^s - \phi_f^s\right)^a}{\left(\phi_{\max}^s - \phi^s\right)^b}, & \phi^s \geq \phi_f^s \end{array} \right\}, \tag{2.19}$$

$$\tau_{ij}^{sf} = -2\mu^{sf} S_{ij}^s \tag{2.20}$$

where $F = 0.05$, $a = 3$, and $b = 5$ are empirical coefficients. Enduring contact becomes dominant at the threshold concentration of $\phi^s = 0.57$ and $\phi_{\max}^s = 0.635$ is specified (Cheng et al., 2017). The frictional viscosity, μ^{sf}, is calculated following (Srivastava and Sundaresan, 2003):

$$\mu^{sf} = \frac{\sqrt{2} p^{sf} \sin\left(\theta_f\right)}{2\sqrt{S_{ij}^s S_{ij}^s}} \tag{2.21}$$

where $\theta_f = 28^\circ$ is the angle of repose for sand.

2.1.2 Numerical implementations

The standard PIMPLE (i.e., PISO-SIMPLE) algorithm is used to solve the fluid and sediment momentum equations (i.e., Eqs. (2.3) and (2.4)). Intermediate velocities are calculated from the previous time-step (or initial condition) without pressure correction and then corrected with pressure gradients (Rusche, 2003; Passalacqua and Fox, 2012). After solving for pressure, the velocities are updated again with the restrictions of mass conservation. These final velocities are used to update the fluid and sediment volumetric concentrations, turbulence quantities, and stresses.

The convection terms are converted into surface integrals for each cell using the Gauss theorem. The sediment fluxes are then calculated using a second-order total variation diminishing scheme based on the Sweby limiter (Sweby, 1984). Mixture fluxes are solved using the

upwind scheme. For the diffusion terms, a central difference scheme with a nonorthogonal correction (Jasak, 1996) is applied to discretize and solve the resulting fluxes.

Time integration is evaluated using the implicit second-order backward scheme, where the time step of the model satisfies the Courant-Friedrichs-Lewy condition:

$$C_0 = \left\{ \begin{array}{ll} \dfrac{U^f \Delta t}{\Delta} \leq C_{max}, & U^f > U^s \\ \dfrac{U^s \Delta t}{\Delta} \leq C_{max}, & U^f \leq U^s \end{array} \right\}, \tag{2.22}$$

where C_0 is the courant number, U is the absolute velocity magnitude, Δ is the grid size characteristic length, Δt is the automatically updated time step, and $C_{max} = 0.2$ to optimize numerical stability and calculation time. Readers are directed to Cheng et al. (2017) and Chauchat et al. (2017) for additional details regarding SedFoam.

2.2 SedOlaFlow

In this section, a novel numerical modeling strategy capable of simultaneously resolving surface and subsurface flows is presented. Generally, beach groundwater numerical modeling efforts rely on hydrostatic and/or saturated flow assumptions (e.g., Li et al., 1997; Perera et al., 2019). Although these simplifications and approximations have lead to satisfactory results in simulating the groundwater table response to swash events (Pintado-Patiño et al., 2015), these assumptions fundamentally omit capillary fringe and groundwater impacts on swash flows. A more robust subsurface-surface flow description is necessary to accurately characterize variably-saturated flow and capillary fringe processes occurring at the swash-groundwater interface. The OpenFOAM numerical toolbox provides a robust basis for model development; it is an advanced, open-source computational fluid dynamics library that is widely used, well documented, and can be modified. A significant advantage of OpenFOAM is its modular and flexible nature that enables capabilities of existing solvers (e.g., for wave generation, sediment transport) to be merged, reducing development cost.

To simulate tightly-coupled surface-subsurface interactions in the swash zone, a free surface resolving Eulerian two-phase numerical model is developed in the OpenFOAM framework by modifying the existing solver olaFlow (Higuera et al., 2014) and combining it with elements (primarily the drag term) of SedWaveFoam (Kim et al., 2018). SedWaveFoam, developed by merging SedFoam (Chauchat et al., 2017; Cheng et al., 2017), InterFoam (Berberović et al., 2009; Klostermann et al., 2012) and waves2Foam (Jacobsen et al., 2012), resolves the free surface wave field and full vertical profiles of fluid and sediment transport processes using the Reynolds-averaged Eulerian two-phase flow equations. It has been validated for monochromatic non-breaking waves (Kim et al., 2018), asymmetric near-breaking waves (Kim et al., 2019), and shoaling waves (Kim et al., 2021). However, SedWaveFoam is currently only capable of modeling flows over saturated sediment beds. The widely-used, comprehensive solver, olaFlow, enables wave generation and absorption and the ability to simulate porous media; olaFlow does not explicitly model the sediment phase and approximates sediment properties through porosity. SedOlaFlow is a novel numerical modeling strategy capable of simultaneously resolving the free surface and porous media flow without restricting assumptions or approximations with regards to surface-subsurface interactions in the swash zone.

2.2.1 Governing equations

The three phases (i.e., air, water, and sediment) involved with swash zone flows are explicitly included in model development. The mass conservation equations for air, water, and sediment phases are written as (Drew, 1983):

$$\frac{\partial \phi^a}{\partial t} + \frac{\partial \phi^a u_i^a}{\partial x_i} = 0, \tag{2.23}$$

$$\frac{\partial \phi^w}{\partial t} + \frac{\partial \phi^w u_i^w}{\partial x_i} = 0, \tag{2.24}$$

$$\frac{\partial \phi^s}{\partial t} + \frac{\partial \phi^s u_i^s}{\partial x_i} = 0, \tag{2.25}$$

where u is velocity and ϕ is the volumetric concentration of each phase. The superscripts "a", "w", and "s" represent air, water, and sediment phases, respectively. The subscript "i" indicates streamwise ($i = 1$), spanwise ($i = 2$), and vertical ($i = 3$) components.

The beach is made immobile (i.e., $u^s = 0$ m/s) to focus directly on infiltration/exfiltration processes. This simplification enables direct analysis of surface-subsurface water exchange without confounding factors such as seepage effects on the effective weight of sediment. Additionally, the impacts of the groundwater table on swash flows over various beach sediment sizes and slopes can be compared directly without the complicating influence of erosion/accretion. The sediment phase is modeled as a miscible solid while the fluid phases (i.e., air and water) are modeled as immiscible fluids. The superscript "f" represents this air-water mixture phase where $\phi^a + \phi^w = \phi^f$ and $u^f = (u^a\phi^a + u^w\phi^w)/\phi^f$. Total mass conservation requires $\phi^f + \phi^s = 1$. The mass conservation equations for air and water are combined into the fluid phase as:

$$\frac{\partial \phi^f u_i^f}{\partial t} = \frac{\partial U_i^f}{\partial x_i} = 0. \tag{2.26}$$

where $U_i^f = \phi^f u_i^f$. The interface compression method is applied to minimize diffusion at the air-water interface (Berberović et al., 2009; Klostermann et al., 2012):

$$\frac{\partial}{\partial t}\left(\frac{\phi^w}{\phi^f}\right) + \frac{1}{\phi^f}\frac{\partial}{\partial x_i}\left[\frac{\phi^w}{\phi^f}U_i^f + \frac{\phi^w}{\phi^f}\left(1 - \frac{\phi^w}{\phi^f}\right)U_i^r\right] = 0. \tag{2.27}$$

where U^r represents the relative velocity between air and water (e.g., $U_i^r = U_i^w - U_i^a$) calculated with an iterative method. A Reynolds-average approach to describe the momentum equation for the fluid mixture phase is adopted (Kim et al., 2018):

$$\frac{1 + C_m}{\phi^f}\frac{\partial \rho^f U_i^f}{\partial t} + \frac{1}{\phi^f}\frac{\partial}{\partial x_j}\left(\frac{\rho^f U_i^f U_j^f}{\phi^f}\right) = -\frac{\partial p^f}{\partial x_i} - \rho^f g\delta_{i3} + \sigma_t\gamma\frac{\partial}{\partial x_i}\left(\frac{\phi^w}{\phi^f}\right) + \frac{1}{\phi^f}\frac{\partial \tau_{ij}^f}{\partial x_j} + \frac{1}{\phi^f}M_i^{fs} \tag{2.28}$$

where C_m is the added mass coefficient (set to 0), $g = 9.81$ m^2/s is gravitational acceleration, and δ_{i3} is the Dirac delta function. The mixture fluid density satisfies $\rho^f = (\rho^a\phi^a + \rho^w\phi^w)/\phi^f$ where $\rho^a = 1$ kg/m^3 and $\rho^w = 1{,}000$ kg/m^3 (only single-density flow is considered). The

third term on the right-hand side of Equation (2.28) represents surface tension where σ_t is the surface tension coefficient and γ is the surface curvature. The fluid stress, τ_{ij}^f, includes grain-scale viscous stress and turbulent Reynolds stress calculated with a two-equation k-ε turbulence model (see Cheng et al. (2017) for details). The inter-phase momentum transfer between the fluid and sediment phases follows Newton's 3rd Law, $M_i^{fs} = -M_i^{sf}$, and is defined for immobile sediment as:

$$M_i^{fs} = -(1-\phi^f)KU_i^f + K\phi^f \frac{\nu^{ft}}{\sigma_c}\frac{\partial \phi^f}{\partial x_i}, \tag{2.29}$$

where K is the drag parameter. The turbulent viscosity of the fluid phase, ν^{ft}, is calculated via turbulence closure and $\sigma_c = 1.0$ is the Schmidt number. K is calculated for immobile sediment as (Ding and Gidaspow, 1990):

$$K = \left\{ \begin{array}{ll} \alpha \dfrac{\left(1-\phi^f\right)\nu^f}{\left(\phi^f d\right)^2} + \beta \dfrac{\rho^f |U_i^f|}{d\left(\phi^f\right)^2}, & \phi^f \leq 0.8 \\ \dfrac{0.75 C_d \rho^f |U_i^f| (\phi^f)^{-3.65}}{d}, & \phi^f > 0.8 \end{array} \right\}, \tag{2.30}$$

where the fluid molecular viscosity is $\nu^f = 10^{-6}$ m^2/s, d is the sediment diameter, and α and β are the Darcy-Forchheimer drag coefficients. The drag coefficient C_d is calculated as (Ding and Gidaspow, 1990):

$$C_d = \left\{ \begin{array}{ll} \dfrac{24(1+0.15Re_p^{0.687})}{Re_p}, & Re_p \leq 1000 \\ 0.44, & Re_p > 1000 \end{array} \right\}. \tag{2.31}$$

2.2.1.1 Fluid turbulence closures

Fluid stress, τ_{ij}^f, in Eq. (2.28) is composed of large-scale Reynolds stress, R_{ij}^{ft}, and grain-scale stress (which includes viscous stress), r_{ij}^f. The total fluid stress is written as:

$$\tau_{ij}^f = R_{ij}^{ft} + r_{if}^f = \rho^f \phi^f [2(\nu^{ft} + \nu^f) S_{ij}^f - \frac{2}{3} k^f \delta_{ij}], \tag{2.32}$$

where ν^{ft} is calculated as:

$$\nu^{ft} = C_\mu \frac{(k^f)^2}{\varepsilon^f}. \tag{2.33}$$

The empirical coefficient $C_\mu = 0.09$ is consistent with standard clear fluid flow modeling, k^f is the fluid turbulent kinetic energy (TKE), and ε^f is the turbulent dissipation rate. The deviatoric part of the strain rate, S_{ij}^f, is defined as:

$$S_{ij}^f = \frac{1}{2}(\frac{\partial u_i^f}{\partial x_j} + \frac{\partial u_j^f}{\partial x_i}) - \frac{1}{3}\frac{\partial u_k^f}{\partial x_k}\delta_{ij}. \tag{2.34}$$

Fluid TKE is calculated by the balance equation for immobile particles in water as (Yu et al., 2010) :

$$\frac{\partial k^f}{\partial t} + u_j^f\frac{\partial k^f}{\partial x_j} = \frac{R_{ij}^{ft}}{\rho^f}\frac{\partial u_i^f}{\partial x_j} + \frac{\partial}{\partial x_j}[(v^f + \frac{v^{ft}}{\sigma_k})\frac{\partial k^f}{\partial x_j}] - \varepsilon^f - \frac{2\beta(1-\alpha_c)\phi^s k^f}{\rho^f\phi^f}, \tag{2.35}$$

where $\sigma_k = 1.0$ is the Schmidt number for TKE (e.g., Rodi, 1993) and $s = \rho^s/\rho^f$ is the specific gravity of the sediment. The particle-fluid correlation variable, α_c, represents the level of correlation between fluid and sediment velocity fluctuations.

The turbulent dissipation rate, ε^f, is calculated as:

$$\frac{\partial \varepsilon^f}{\partial t} + u_j^f\frac{\partial \varepsilon^f}{\partial x_j} = C_{1\varepsilon}\frac{\varepsilon^f}{k^f}\frac{R_{ij}^{ft}}{\rho^f}\frac{\partial u_i^f}{\partial x_j} + \frac{\partial}{\partial x_j}[(v^f + \frac{v^{ft}}{\sigma_\varepsilon})\frac{\partial \varepsilon^f}{\partial x_j}] - C_{2\varepsilon}\frac{\varepsilon^f}{k^f}\varepsilon^f - C_{3\varepsilon}\frac{\varepsilon^f}{k^f}\frac{2\beta(1-\alpha_c)\phi^s k^f}{\rho^f\phi^f}, \tag{2.36}$$

where $\sigma_\varepsilon = 1$ (Rodi, 1993) and the empirical coefficients are selected as $C_{1\varepsilon} = 1.44$, $C_{2\varepsilon} = 1.92$, and $C_{3\varepsilon} = 1.2$ (Cheng et al., 2017). TKE and ε^f attenuation due to particle inertial effects are represented in the last terms on the right-hand side of Eqs. (2.35) and (2.36), respectively.

2.2.2 Numerical implementation

The standard PIMPLE (i.e., PISO-SIMPLE) algorithm (Passalacqua and Fox, 2011) is used to solve the fluid momentum equation (i.e., Eq. (2.28)). Intermediate velocities are calculated from the previous time-step (or initial condition) without pressure correction and then corrected with pressure gradients (Rusche, 2003; Passalacqua and Fox, 2012). After

solving for pressure, the velocities are updated to satisfy mass conservation. These final velocities are used to update the fluid volumetric concentrations, turbulence quantities, and stresses. The convection terms are converted into surface integrals for each cell using the Gauss theorem. The upwind scheme is chosen to solve for the mixture fluxes. For the diffusion terms, a central difference scheme with a non-orthogonal correction (Jasak, 1996) is applied to discretize and solve the resulting fluxes. The explicit OpenFOAM solver MULES (Weller, 2008) which imposes strict bounds of $0 \leq \phi \leq 1$ for all phases is used to solve for the free surface (i.e., Eq. (2.27)).

Time integration is evaluated using the implicit second-order backward scheme, where the time step of the model satisfies the Courant-Friedrichs-Lewy condition:

$$C_0 = \left\{ \begin{array}{l} \dfrac{U^f \Delta t}{\Delta} \leq C_{\max}, \quad U^f > U^s \\ \\ \dfrac{U^s \Delta t}{\Delta} \leq C_{\max}, \quad U^f \leq U^s \end{array} \right\}, \tag{2.37}$$

where C_0 is the courant number, U is the absolute velocity magnitude, Δ is the grid size characteristic length, Δt is the automatically updated time step, and $C_{max} = 0.2$ to optimize numerical stability and calculation time.

CHAPTER 3

Sheet flow driven by a near-breaking transient wave

3.1 Background

Complex sediment transport mechanisms largely define nearshore morphological evolution. Generally, sediment transport is divided into two regimes, the upper suspended load-dominant layer and the lower bedload-dominant sheet flow layer (Bagnold, 1956; Bailard, 1981; Dally and Dean, 1984; Roelvink and Brøker, 1993; Van Rijn, 2007). Suspended load occupies the majority of the water column and results from turbulent fluid motions. Sheet flow is the mobilized layer of sediment grains in a thin ($\sim$10 mm), highly-concentrated region immediately above the immobile bed and occurs when strong fluid flow or large bed shear stress is exerted on the sediment bed. In the sheet flow regime, ripples are washed out and the sediment bed becomes relatively flat. Sheet flow exists under a variety of flow conditions, such as steady-uniform flow in streams and rivers (e.g., Whiting et al., 1988; Dinehart, 1992), tidal flow in estuaries (e.g., Miller and Gardner, 1981), and unsteady-oscillatory flow in coastal environments (e.g., Dingler and Inman, 1976; Yu et al., 1990; Masselink and Hughes, 1998). Strong bed shear stress associated with sheet flow can transport significant volumes of sediment. Accurately resolving sediment transport processes in the coastal zone has been identified as a fundamental research need (e.g., Dohmen-Janssen et al., 2001; Van Rijn et al., 2013).

Sheet flow is affected by various factors including velocity skewness (e.g., Hsu et al., 2006; Ruessink et al., 2007), acceleration skewness (e.g., Flores and Sleath, 1998; Drake and Calantoni, 2001; Hoefel and Elgar, 2003; Foster et al., 2006; Kim et al., 2019), boundary

layer streaming (e.g., Longuet-Higgins, 1953; Trowbridge and Young, 1989; Henderson et al., 2004; Nielsen, 2006; Yu et al., 2010; Kim et al., 2018), and wave-breaking turbulence (e.g., Scott et al., 2009; Zhou et al., 2017). Positive velocity skewness drives onshore-directed sediment transport (Ruessink et al., 2007). Large acceleration skewness amplifies the mobilized sediment layer thickness and, in combination with large bed shear stress, can lead to momentary bed failure (Foster et al., 2006; Kim et al., 2019). Kim et al. (2018) suggested that progressive wave streaming, a component of boundary layer streaming, enhances suspended load sediment transport. The interaction between wave-breaking turbulence and the sediment bed can also enhance sediment transport (Scott et al., 2009) and was shown to induce large sediment suspension (Zhou et al., 2017). Notably, the impact of wave forcing on sheet flow remains unresolved.

A primary driver of sheet flow is bed shear stress. Non-dimensionalized bed shear stress (i.e., Shields parameter; Shields, 1936) is conventionally used to characterize sediment transport processes in both steady and unsteady flows (e.g., Madsen and Grant, 1976; Ribberink, 1998). In the absence of direct measurements, the quasi-steady approach is typically used to describe bed shear stress as a function of the free stream velocity (e.g., Madsen and Grant, 1976; Dohmen-Janssen et al., 2002; Nielsen and Callaghan, 2003; Wang, 2007; Mieras et al., 2017). The underlying assumption that the free stream velocity is in phase with bed shear stress can lead to errors imparted by temporal phase shifts (e.g., Flores and Sleath, 1998; Nielsen and Callaghan, 2003). To extend the applicability of the quasi-steady approach to asymmetric and skewed waves, a variable friction factor incorporating wave shape effects has been proposed (Gonzalez-Rodriguez and Madsen, 2007). Nevertheless, in relying on the free stream velocity to parameterize bed shear stress, detailed boundary layer processes may be neglected. For example, density stratification induced by fine particle suspension dampens near-bed turbulence (e.g., Dohmen-Janssen et al., 2001; Wilson, 2005; Ozdemir et al., 2010; Egan et al., 2020), which in turn may lead to decreased bed shear stress.

A number of studies have attempted to observe and quantify sheet flow sediment trans-

port. Wave-driven sheet flow has been measured through oscillating water tunnel experiments (e.g., Sleath, 1987; Dibajnia and Watanabe, 1992; Ribberink and Al-Salem, 1994, 1995; Flores and Sleath, 1998; Fredsøe et al., 2003; O'Donoghue and Wright, 2004a), prototype scale wave flume experiments (e.g., Dohmen-Janssen and Hanes, 2002, 2005; Schretlen, 2012; Van Der Zanden et al., 2015; Anderson et al., 2017; Mieras et al., 2017, 2019), and field observations (e.g., Gallagher et al., 1998). Ribberink and Al-Salem (1994, 1995) demonstrated that the majority of sediment transport occurs within the bedload-dominant sublayer under asymmetric-oscillatory flows. In contrast, suspended load was found to be of roughly the same order of magnitude as bedload sediment transport under skewed-asymmetric waves (Mieras et al., 2019). On a natural beach, Gallagher et al. (1998) observed that suspended load driven by oscillatory mean currents dominated the total sediment transport. However, the relative contributions of bedload and suspended load to sediment transport remain ambiguous. The commonly used criterion partitioning bedload load (i.e., the elevation at which grain-grain interactions become important) and suspended load (i.e., the elevation at which the average distance between spherical grains is equal or larger than one grain diameter) varies in application (Bagnold, 1956). Identifying the mechanisms controlling sediment transport under a range of flow conditions is fundamental to elucidating detailed bed responses and a comprehensive understanding of coastal morphology.

A series of wave flume observations from the sandBAR SEDiment transport experiment (BARSED) investigated the impacts of skewed-asymmetric wave forcing on sheet flow layer dynamics (Anderson et al., 2017; Mieras et al., 2017, 2019). The maximum sheet flow layer thickness was well correlated with the estimated maximum bed shear stress under skewed-asymmetric waves (Mieras et al., 2017). Acceleration skewness at the time of flow reversal coincided with momentary bed failure and resulted in enhanced sheet flow layer thickness (Anderson et al., 2017). Mieras et al. (2019) quantified bedload and suspended load sediment transport rates under a range of skewed-asymmetric wave forcing conditions and found that net suspended load and bedload sediment transport rates were generally offshore and onshore

directed, respectively.

In addition to the periodic wave cases, transient wave (i.e., an asymmetric long wave with a solitary peak) simulations were conducted in the BARSED experiment (Mieras et al., 2018). An advantage of the transient wave case is simplified sheet flow dynamics where complex sediment transport mechanisms can be decomposed (e.g., the effect of progressive wave streaming can be excluded). In addition, the sheet flow layer thickness is sustained ∼65% longer in comparison to periodic cases, facilitating the study of suspended sediment-induced density stratification. BARSED provides extensive in-situ observations of surface elevations, sediment concentration, and velocity above the sheet flow layer. However, numerical models are needed in combination with observations to examine the interactions between bed shear stress, near-bed velocity, and sediment transport.

The first numerical models capable of replicating sheet-flow sediment transport consisted of only a single-phase (e.g., Kaczmarek, 1991; Nadaoka and Yagi, 1991). For example, Nadaoka and Yagi (1991) produced a computational scheme for collision-dominated sediment transport based on Bagnold (1954). Single-phase models, however, provide an incomplete description of sediment transport, consequently two-phase models were developed to provide a more detailed understanding of sediment transport (e.g., Dong and Zhang, 1999; Hsu et al., 2004; Amoudry et al., 2008; Cheng et al., 2017; Chauchat, 2018; Nagel et al., 2020). Chauchat et al. (2017) created a two phase model capable of modeling complex, multidimensional sediment transport problems with various intergranular stress (i.e., kinetic theory of granular flows or dense granular-flow rheology) and turbulence theories (i.e., mixing length, k-ε, or k-ω). Recently, two-phase sediment transport models explicitly resolving the free surface have been proposed (Kim et al., 2018; Ouda and Toorman, 2019). Kim et al. (2018) and Ouda and Toorman (2019) developed unique models that track the interfaces among air, water, and sediment phases, enabling detailed investigation of free surface effects (e.g., progressive wave streaming) on sediment transport. Two-phase models with and without free surface capabilities eliminate the bedload/suspended load assumptions required for

single-phase models and facilitate detailed sheet flow layer investigations.

The purpose of this study is to investigate the near-bed sediment transport response to hydrodynamic forcing mechanisms under a near-breaking transient wave. SedFoam, a two-phase sediment transport model widely validated for sheet flow (e.g., Chauchat et al., 2017), is adopted to simulate sediment transport on the sandbar crest of the BARSED experiment. The description of the numerical model used is described in Section 3.2.1. Section 3.2 outlines the experimental and model setup. Section 3.3 presents model validation and the main flow and sediment results. Discussion of bed shear stress, the profile shape parameter for near-bed velocity, and the corresponding impact on predictions of sediment transport are included in Section 3.4. Section 3.5 summarizes the main conclusions of this study.

3.2 Methods

3.2.1 Numerical model

In this study, the two-phase sediment transport model, SedFoam (e.g., Cheng et al., 2017; Chauchat et al., 2017; Mathieu et al., 2019), is utilized to simulate sheet flow driven by a near-breaking transient wave. Based on a two-phase flow approach where sediment is modeled as a continuum, the numerical model concurrently resolves the full profiles of bottom boundary layer (BBL) flow and sediment transport processes without the conventional bedload and suspended load assumptions of single-phase models. Although continuum models are more limited than particle-based models such as smoothed-particle hydrodynamics (SPH) or the discrete element method (DEM), Reynolds-Averaged Navier-Stokes (RANS) models have been shown to sufficiently resolve boundary layer processes without the extraordinary computational burden of particle methods (e.g., Torres-Freyermuth et al., 2013; Briganti et al., 2016; Cheng et al., 2017; Chauchat, 2018). A description of the numerical model can be found in Section 2.1 with more detailed description in (Cheng et al., 2017).

3.2.2 Experimental setup

The BARSED experiment was conducted at the O.H. Hinsdale Wave Research Laboratory (Oregon State University) in a 104 m × 3.7 m × 4.6 m (length × width × depth) wave flume (Anderson et al., 2017; Mieras et al., 2017, 2018). A fixed, near-field scale barred beach profile was constructed at roughly 1:3 scale based on observed beach profiles during the Duck94 experiment (Faria et al., 1996; Gallagher et al., 1998; Scott et al., 2005). Concrete slabs (3.66 m × 3.66 m) were used to construct the piecewise continuous profile. On the sandbar crest, a sediment pit was installed (rather than a concrete slab) with dimensions of 3.66 m × 3.66 m × 0.17 m (length × width × depth) and was filled with sediment of median grain diameter $d_{50} = 0.17$ mm ($d_{16} = 0.10$ mm, $d_{84} = 0.26$ mm). The still water depth during the experimental trial presented was 2.00 m at the wave maker (Fig. 3.1a).

Cross-shore variation of free surface elevation was measured at 100 Hz with 11 resistance-type wave gauges (offshore and surf zone) and six ultrasonic wave gauges (inner-surf and swash zones). An array of sensors located at the center of the sandbar crest ($x = 45.14$ m) measured velocity and sediment concentration profiles. The velocity profiles spanning the water column from 0.12 m to 0.72 m above the initial sediment bed level were measured by a vertical array of four Acoustic Doppler Velocimeters (ADVs; 100 Hz) spaced 0.2 m apart. The near-bed velocity profiles from -0.003 m to 0.022 m above the sediment bed were measured with Acoustic Doppler Profiling Velocimeters (ADPVs; 100 Hz) at 0.001 m resolution. Linear interpolation was used to approximate velocities between the elevation of the highest ADPV and lowest ADV (Mieras et al., 2019). Two Fiber Optic Backscatter Sensors (FOBS; 8 Hz) measured the suspended sediment concentration (<200 g/L) over the sandbar with vertical resolution ranging from 0.01 to 0.07 m. Measurements spanned the initial bed level up to roughly 0.47 m above the bed, comprising a 20-point concentration profile. Sediment concentration profiles were measured from the elevation of the immobile bed up to 0.02 m above the initial bed level using Conductivity Concentration Profilers (CCPs, Lanckriet et al. (2013); 8 Hz) with 0.001 m vertical resolution.

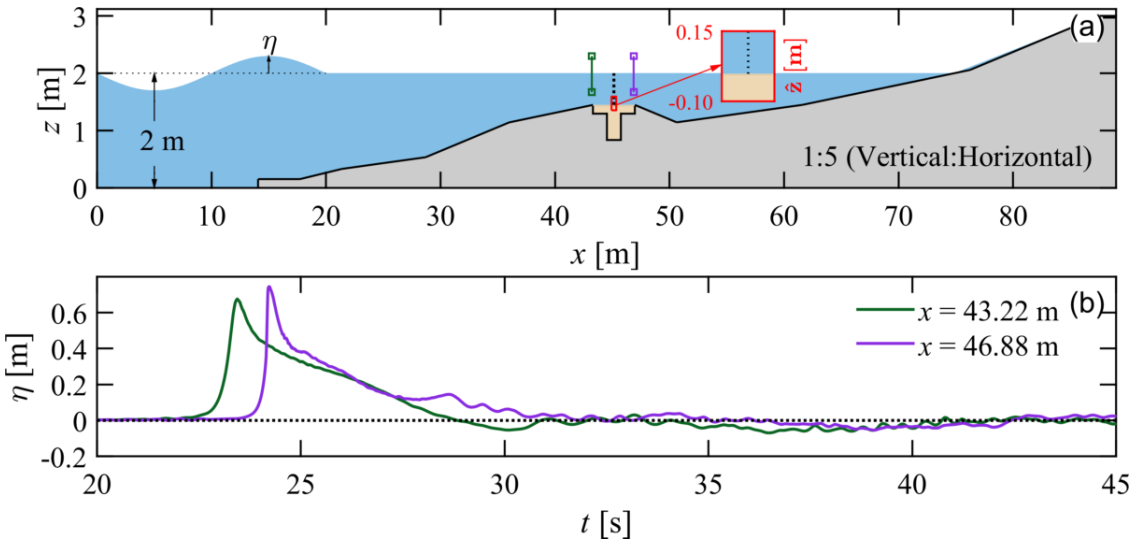

Figure 3.1: (a) Experimental setup of the barred beach profile with a sediment pit. The black vertical dotted line on the sandbar crest indicates the cross-shore deployment location of the sensors for velocity and sediment concentration profiles. The green and purple markers indicate the cross-shore location of two wave gauges. The red inset indicates the numerical model domain; the 1DV model includes only a single grid cell in the spanwise and streamwise directions. (b) Time series of Run 92 (S1TR10) measured free surface elevation (η) at the wave gauges corresponding to the cross-shore locations shown in (a) with colored, vertical markers.

The BARSED experiment consisted of various test conditions, including both monochromatic and transient wave cases. Model validation and further discussion in this study is conducted using observations from Run 92 of the single transient wave case, referred to as S1TR10. Similar to previous simulations of transient waves (e.g., Baldock et al., 2009; Thomas and Cox, 2012; Park et al., 2017), S1TR10 was generated through an error function implemented for the wave maker displacement:

$$\mathrm{erf}(\frac{T}{5} \cdot t) \equiv \frac{2}{\sqrt{\pi}} \int_0^{\frac{t \cdot T}{5}} e^{-\tau^2} d\tau, \tag{3.1}$$

where $T = 10$ s is the time for the paddle to travel the full 4-m stroke, after which, the wave maker returns at a constant speed to its initial position. The resulting wave maker motion generated an asymmetric, long transient wave with a solitary peak that shoaled to a wave height of 0.68 m and 0.74 m at the offshore ($x = 43.22$ m) and onshore ($x = 46.88$ m) edges of the sandbar crest, respectively, as shown by the measured free surface elevations (η) in Fig. 3.1b. The onset of wave breaking was observed between 46.88 m $< x <$ 50.53 m and 24 s $< t <$ 25 s. The transient wave induced highly turbulent flow with a Reynolds number ($Re = u_\infty^f h/\nu^f$; u_∞^f is the free stream fluid velocity (see Sec. 3.3) and h is the flow depth) greater than 10^6, substantially larger than the accepted threshold of 2000 for turbulent flows.

3.2.3 Model setup

A one-dimensional-vertical (1DV) model domain was created to numerically study the processes within the BBL at the streamwise center of the sediment pit ($x = 45.14$ m), coinciding with the sensor locations in the physical experiment. The model used in this study, SedFoam, includes only water and sediment phases, thus lacking the capability to resolve the air-water interface (i.e., free surface). For a transient wave, however, free surface effects are expected to be minor as behaviors such as progressive wave streaming exist only under wave trains. Previously, Kim et al. (2019) showed that under the BARSED monochromatic periodic waves, flow and sediment transport quantities were in a quasi-equilibrium state across

a 0.77 m streamwise span centered in the middle of the sediment pit (x = 45.14 m). Thus, no edge effects (e.g., scour, accumulation of sediment) are expected at the center of the sediment pit in this study. The simplified 1DV model (excluding the free surface) is adopted to simulate the sheet flow assumed to be statistically homogeneous in both streamwise and spanwise directions, consistent with Cheng et al. (2017).

The modeled vertical coordinate system, $\hat{z}$, is a linear shift of the fixed flume vertical coordinate system, z (i.e., $\hat{z} = z - 1.447$ m). The $\hat{z}$-coordinate system is defined as positive upward and $\hat{z} = 0$ m is the elevation of the initial model sediment bed. The total numerical domain height is 0.244 m with an initial sediment depth of 0.096 m (inset, Fig. 3.1a). The vertical extent of the computational domain is sufficient to capture sediment transport processes occurring in the BBL (Fig. 3.3). A single grid cell was applied to the horizontal-spanwise (x-y) plane. Various mesh setups with uniform grid spacing of $dz = 1$ mm ($\sim 6d_{50}$), 0.5 mm ($\sim 3d_{50}$), and 0.2 mm ($\sim d_{50}$) were generated to check sensitivity to the grid resolution. The sensitivity tests showed that modeled velocity and concentration results converged to similar solutions using $dz \leq 0.5$ mm. The $dz = 1$ mm case over-predicted the maximum streamwise velocity (u^f) at $\hat{z} \approx 11$ mm by 5.5% and the maximum bed shear stress (τ_b) by 40.4% compared to the modeled $dz = 0.2$ mm case (Fig. 3.2). Thus, the 0.2 mm grid resolution case (1220 grid cells) is selected for further analysis. An initial model timestep of 10^{-6} s is used and then dynamically adjusted by the Courant-Friedrichs-Lewy condition with a Courant number of 0.2. The numerical model required a wall-clock time of less than 12 hours using a single processor (3.7 GHz Intel W-2145 Xeon) for the approximately 50 s run.

The flow in the model was driven by the streamwise pressure gradient, $f_1 = \partial p/\partial x$ (Eq. (3.2)). The ADV-measured u^f at $z = 1.57$ m ($\hat{z} = 120$ mm) (i.e., slightly above the maximum modeled BBL elevation of 107.32 mm; see Section 3.4.2) was used to impose f_1

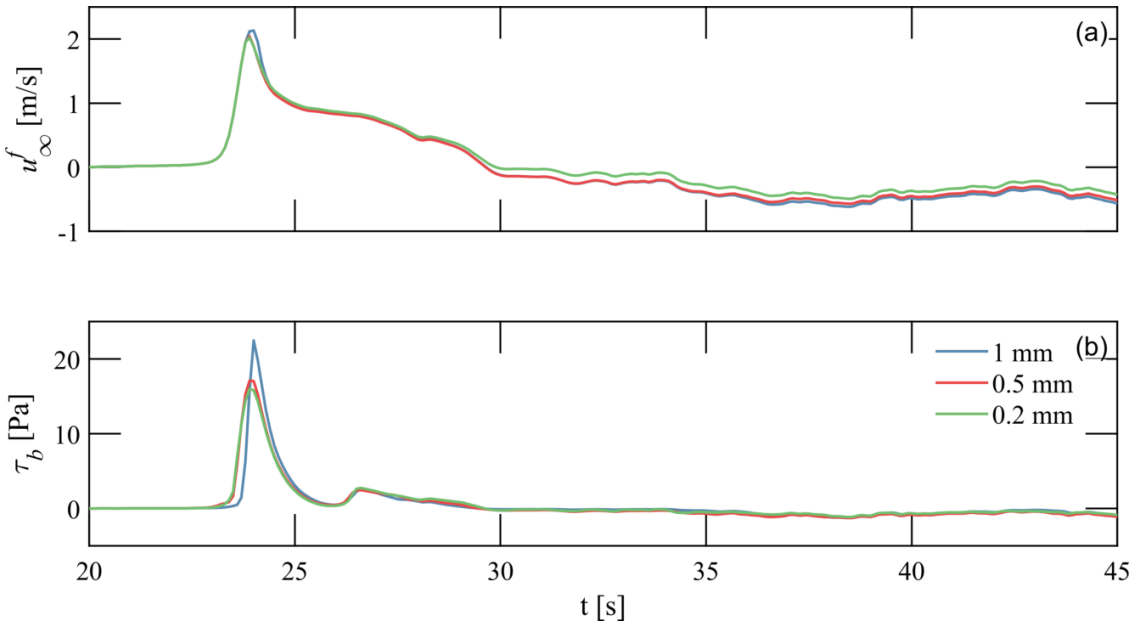

Figure 3.2: Time series of modeled (a) free stream fluid velocity (u^f_∞) and (b) bed shear stress (τ_b) for grid resolutions of 1 mm (blue solid curve), 0.5 mm (red solid curve), and 0.2 mm (green solid curve).

with the boundary approximation:

$$f_1 = \frac{\partial p}{\partial x} = -\frac{1}{\rho^f}\frac{\partial u^f}{\partial t}. \tag{3.2}$$

A wall boundary condition is imposed on the bottom boundary of the computational domain. A no-flux boundary condition is applied for scalar and bottom-normal velocity components. For bottom-parallel velocities, a no-slip condition is applied. It should be noted that the no-slip boundary condition is of minor importance as it exists below the 0.096 m deep sediment layer. On the top boundary, a zero-gradient boundary condition is applied for scalar quantities. For velocities, the plane-normal component is specified to be zero and a free-slip condition is applied to the plane-parallel component. OpenFOAM periodic and empty boundary conditions are imposed on the inlet/outlet (y-z) planes and lateral (x-z) planes, respectively.

3.3 Results

Model results are evaluated based on the normalized root mean square error, NRMSE, and the index of agreement, IA. The NRMSE represents the mean of squared errors with reference to the absolute maximum of the measured data. The index of agreement represents the ratio of the mean squared error and the potential error (Willmott, 1981):

$$IA = 1 - \frac{\sum_{i=1}^{N}\left(x_{O,i} - x_{P,i}\right)^2}{\sum_{i=1}^{N}\left[\left(\left|x_{O,i} - \overline{x}_P\right|\right) + \left(\left|x_{P,i} - \overline{x}_P\right|\right)\right]^2}, \tag{3.3}$$

where N is the number of comparison points and x_P and x_O are the predicted and observed values, respectively. Values of zero and unity for IA correspond to no agreement and complete agreement, respectively.

The initial sediment bed level associated with each trial during the BARSED experiment varied due to non-zero net sediment transport (i.e., the elevation of the sediment bed was not exactly at the horizontal level connecting the tops of the adjacent concrete slabs on the bar;

Mieras et al., 2017, 2019). It is necessary to define a local coordinate system to ensure that measured and modeled vertical profiles are referenced to the same local sediment bed level. Following O'Donoghue and Wright (2004a) and Lanckriet et al. (2014), the inflection point of ϕ^s (i.e., $\partial^2\phi^s/\partial z^2 = 0$) is identified based on a best-fit curve to the sediment concentration profile. The local coordinate $z^* = 0$ is defined for both measured data and model results as the elevation of the inflection point at $t = 22$ s (roughly 2 s prior to the passing the transient wave over the center of the sediment pit). Further details regarding the z^* coordinate system can be found in Mieras et al. (2019).

SedFoam is capable of modeling sheet flow driven by a transient wave. The temporal evolution of modeled ϕ^s is shown in Fig. 3.3. The black dotted and dashed curves correspond to the lower (defined by a threshold u^s value) and upper (i.e., $\phi^s = 8\%$) bounds of the sheet flow layer, respectively, while the black solid curve indicates $\phi^s = 1\%$ (see Section 3.3). To confirm assumptions of sheet flow homogeneity in the streamwise direction are valid, two-dimensional clear fluid modeling of the entire wave flume for case S1TR10 was conducted (not shown here). Results demonstrated homogeneous streamwise velocity profiles (i.e., $IA > 0.999$) in the sediment pit between 44.40 m $< x <$ 46.38 m, indicating quasi-equilibrium in the x-direction. This 1.98 m streamwise span exists between 1.18 m onshore of the green wave gauge and 0.50 m offshore of the purple wave gauge (i.e., between the two wave gauges) shown in Fig. 3.1a. Thus, a 1DV model is adopted to compare measured data to model results at the center of the sediment pit (i.e., $x = 45.14$ m).

The measured streamwise velocity at $z^* = 98.38$ mm is used to impose f_1 in SedFoam (Eq. (3.2)). Above the BBL, it is assumed that the streamwise velocity is independent of elevation. The vertical elevation of the top of the BBL (z_w^*) is defined as the elevation where the maximum u^f is observed (e.g., Jensen et al., 1989; O'Donoghue and Wright, 2004b; Kim et al., 2018, 2019). The maximum modeled z_w^* in the present case is 107.32 mm (see Section 3.4.2), thus u^f at $z^* = 107.32$ mm is defined as the free stream velocity, u_∞^f. The modeled velocity showed a nearly uniform profile from $z^* = 70.12$ mm to the top of the model domain

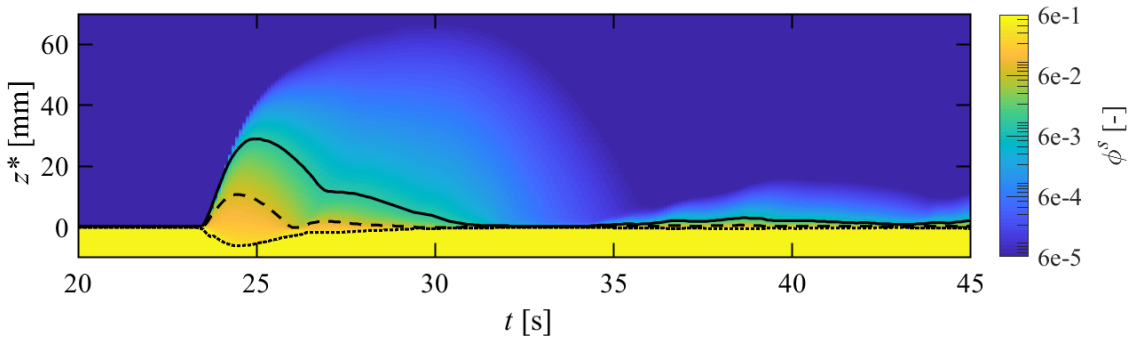

Figure 3.3: Modeled temporal evolution of volumetric sediment concentration (ϕ^s). The black dotted, dashed, and solid curves represent the immobile bed elevation (defined by a threshold u^s value), the top of sheet flow layer (i.e., $\phi^s = 8\%$), and $\phi^s = 1\%$, respectively (see Section 3.3).

at $z^* = 143.72$ mm with $IA > 0.999$ and NRMSE $< 0.5\%$ (not shown here). The comparison between measured u^f at $z^* = 98.38$ mm and modeled u^f_∞ indicates that the model forcing is well incorporated into the model ($IA > 0.999$, NRMSE $= 1.0\%$; Fig. 3.4a).

The instantaneous vertical profiles of u^f at different times are further compared (Figs. 3.4b - g). ADPV signals are quickly attenuated in highly concentrated regions (i.e., $\phi^s \gtrsim 8\%$), therefore ADPV measurements in the sheet flow layer are discarded. Overprediction of u^f is observed when high local acceleration occurs (i.e., $\partial u^f/\partial t > 2$ m/s^2; Fig. 3.4a), leading to less satisfactory agreement at $t = 23.5$ s (NRMSE $= 31.3\%$; Fig. 3.4b). When u^f is small (i.e., $|u^f| < 0.1$ m/s), the NRMSE is inflated by the near-zero velocity used to normalize the error measurement such as at $t = 31$ s (NRMSE $= 32.0\%$; Fig. 3.4f), though good qualitative agreement exists. Otherwise, the model reproduces the u^f profiles well, with NRMSE of 3.6%, 6.3%, 8.5%, and 16.3% at $t = 24$, 25.5, 27.5, and 40 s, respectively (Figs. 3.4c - e, g).

The modeled vertical profiles of normalized volumetric sediment concentration (ϕ^s/ϕ^s_{max}) are compared to measured data in Fig. 3.5 at the same six instants shown in Fig. 3.4. The greatest discrepancy in ϕ^s/ϕ^s_{max} is observed at $t = 23.5$ s, prior to the arrival of the wave

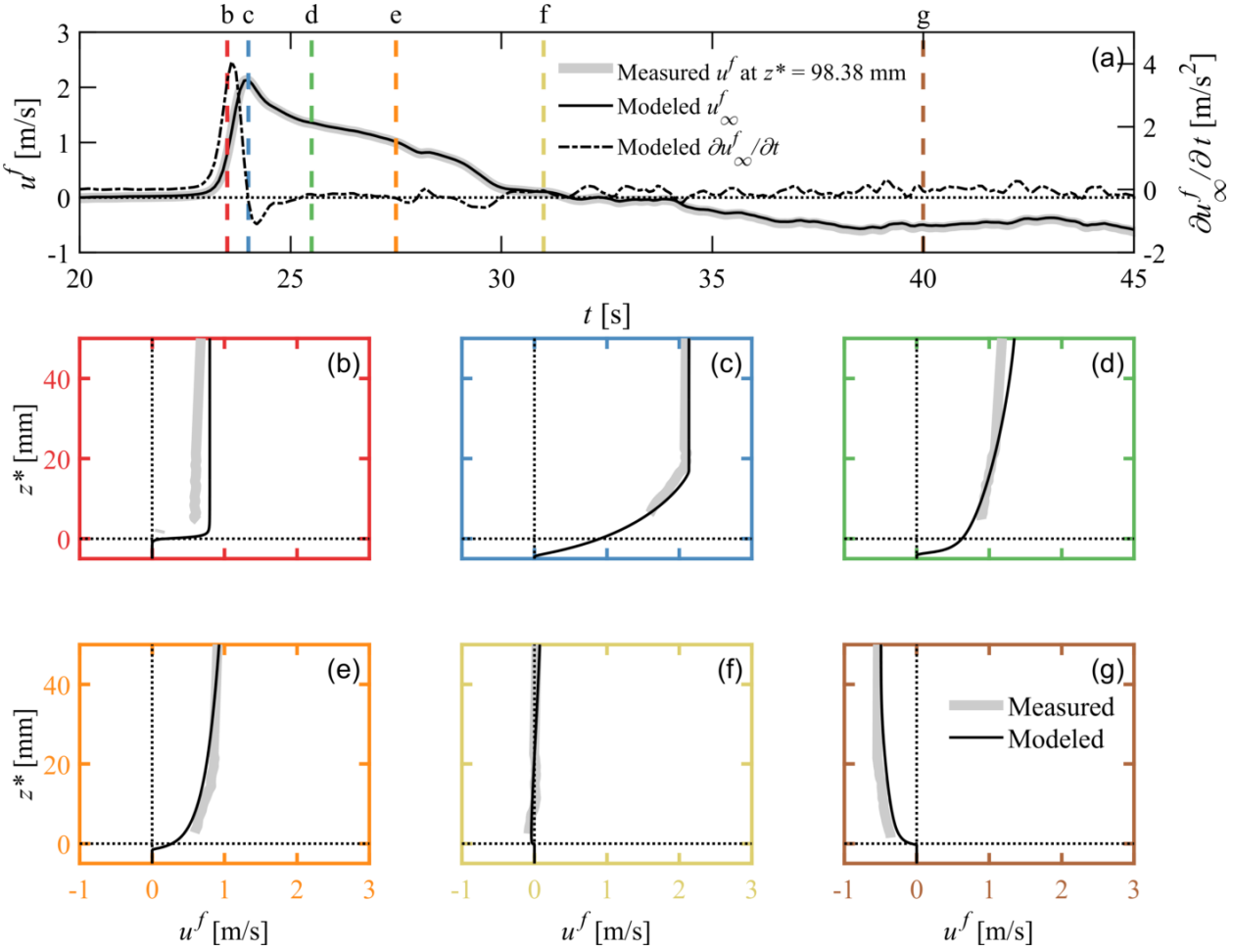

Figure 3.4: (a) Time series of measured streamwise fluid velocity (u^f) at $z^* = 98.38$ mm (grey solid curve), modeled free stream velocity (u^f_∞; black solid curve) and modeled streamwise fluid acceleration ($\partial u^f_\infty/\partial t$; black dash-dotted curve). (b) - (g) are measured (grey curves) and modeled (black curves) vertical profiles of u^f at (b) $t = 23.5$ s (red), (c) $t = 24$ s (blue), (d) $t = 25.5$ s (green), (e) $t = 27.5$ s (orange), (f) $t = 31$ s (yellow), and (g) $t = 40$ s (brown), as marked in (a) using the corresponding colored, vertical dashed lines.

crest at $t \sim 23.8$ s, though the agreement is still satisfactory ($IA = 0.977$, NRMSE = 13.0%; Fig. 3.4b). Noticeably, the disagreement in Fig. 3.4b is largest below $z^* = 0$ and may be attributed to differences between the initial sand configuration of the model and physical experiment. The agreement of ϕ^s / ϕ^s_{max} at the maximum u^f_∞ (i.e., $t = 24$ s) is good ($IA = 0.989$, NRMSE = 7.7%; Fig. 3.4c). Disagreement between measured and modeled ϕ^s/ϕ^s_{max} at $t = 25.5$ s shows that the model slightly over-predicts sediment erosion, however satisfactory agreement is still obtained (IA = 0.978, NRMSE = 10.8%; Fig. 3.5d). Discrepancies when the flow magnitude is relatively low (Figs. 3.5f - g) occur because the CCP sensor used in the physical experiment (measuring $\phi^s/\phi^s_{max} > 0.03$) tends to smooth out sharp gradients in the concentration profile. Nevertheless, overall agreement between measured data and model results remains good, with IA (NRMSE) of 0.996 (5.3%), 0.991 (7.9%), and 0.987 (9.5%) at $t = 27.5$, 31, and 40 s, respectively. The measured suspended sediment concentration data show vertically uniform profiles might arise from wash load and uncertainties in capturing very dilute sediment concentrations ($\phi^s/\phi^s_{max} < 0.01$).

The temporal evolution of the measured and modeled sheet flow layer thickness is compared (Fig. 3.6). The instantaneous vertical location of the top of the sheet flow layer, z^*_s, is defined as the elevation where $\phi^s = 0.08$, the concentration where intergranular forces become negligible (e.g., Dohmen-Janssen et al., 2001; O'Donoghue and Wright, 2004a; Hsu et al., 2004; Ribberink et al., 2008). The modeled sediment bed location, z^*_{bed}, is defined as the instantaneous elevation where the streamwise sediment velocity is smaller than a threshold value, $|u^s| < 10^{-3}$ m/s, which represents a nearly immobile bed and falls within the range of threshold values used in previous studies (e.g., Chauchat, 2018; Kim et al., 2019). Notably, this criterion matches well with the alternate approach that defines z^*_{bed} at the threshold value of $\phi^s = 0.57$ (Hsu et al., 2004) with $IA = 0.995$ and NRMSE = 4.4% (not shown here). The measured z^*_{bed} is estimated as the intersection point between the linear extension from the $\phi^s(z^*)$ inflection point (following the slope based on a composite power law) and a vertical straight line through ϕ^s_{max} (Mieras et al., 2017). The sheet flow layer

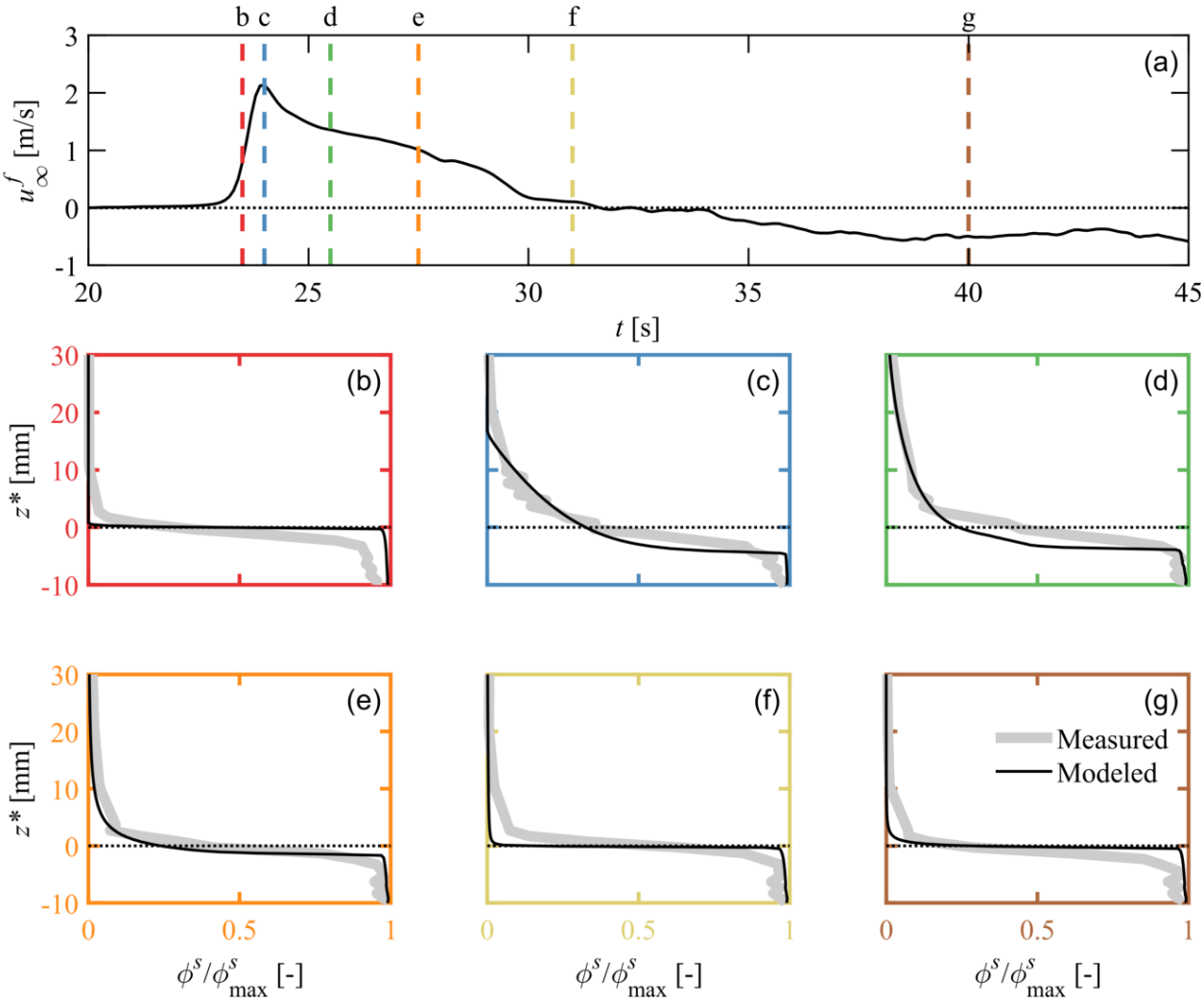

Figure 3.5: (a) Time series of modeled free stream velocity (u^f_∞). (b) - (g) are measured (grey curves) and modeled (black curves) vertical profiles of normalized volumetric sediment concentration (ϕ^s/ϕ^s_{max}) at (b) t = 23.5 s (red), (c) t = 24 s (blue), (d) t = 25.5 s (green), (e) t = 27.5 s (orange), (f) t = 31 s (yellow), and (g) t = 40 s (brown), as marked in (a) using the corresponding colored, vertical dashed lines.

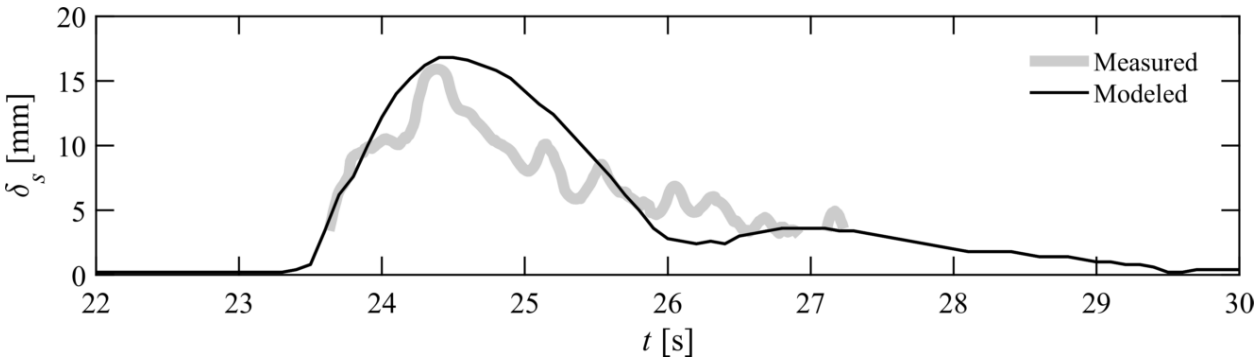

Figure 3.6: Time series of measured (grey curve) and modeled (black curve) sheet flow layer thickness (δ_s).

thickness is:

$$\delta_s = z_s^* - z_{bed}^*. \tag{3.4}$$

A correction formula is applied to the in-situ δ_s to obtain the true measured δ_s and eliminate any over-prediction of the sheet flow layer thickness as a result of CCP smoothing effects (Lanckriet et al., 2013). The minimum reliable sheet flow layer thickness which can be resolved by the CCP is about 5 mm (Lanckriet et al., 2014). SedFoam is able to reproduce the measured sheet flow layer thickness with acceptable agreement (IA = 0.886, NRMSE = 17.40%; Fig. 3.6). The maximum measured sheet flow layer thickness of 15.91 mm is over-predicted by 5.60% in SedFoam. According to Kim et al. (2019), when momentary bed failure occurs, a 1DV model significantly under-predicts the sheet flow layer thickness as compared to both measured data and a free surface resolving sediment transport model. In this study, the model generally over-predicts the sheet flow layer thickness. Thus, momentary bed failure is unlikely in this case.

3.4 Discussion

3.4.1 Bed shear stress

Bed shear stress, τ_b, is a primary driver of bedload-dominant sheet flow and is typically used to parameterize sediment transport in moderate wave conditions (Ribberink, 1998; Van Rijn, 1984). Accurate prediction of τ_b is essential for resolving sediment transport processes. The conventional parameterization of time-dependent τ_b is based on a quasi-steady approach (e.g., Madsen and Grant, 1976; Nielsen and Callaghan, 2003; Wang, 2007; Mieras et al., 2017):

$$\tau_b(t) = \frac{1}{2}\rho^f f_{ws} u_\infty^f(t)|u_\infty^f(t)|, \tag{3.5}$$

where f_{ws} is the wave friction factor (Swart, 1974). Madsen (1994) proposed an explicit solution for f_{ws}:

$$f_{ws} = \begin{cases} \exp(7.0X^{-0.078} - 8.8) & \text{for } 0.2 < X < 10^2 \\ \exp(5.6X^{-0.109} - 7.3) & \text{for } 10^2 < X < 10^4 \end{cases}, \tag{3.6}$$

based on the linearized boundary layer equations and assuming a time-invariant, linearly varying eddy viscosity. For a non-periodic transient wave, the formulation for X can be employed from Gonzalez-Rodriguez and Madsen (2007):

$$X = \frac{u_{\infty,c}^f T_{cp}}{2\pi k_s}, \tag{3.7}$$

where $u_{\infty,c}^f$ is the free stream velocity at the wave crest, k_s is the equivalent Nikuradse roughness of the bed, and $T_{cp}/4$ is the characteristic time between $u_\infty^f = 0$ m/s and $u_\infty^f = u_{\infty,c}^f$ (Fig. 3.7a). The k_s has been shown to be proportional to the Shields parameter (Wilson, 1989) and is typically characterized by the sediment grain size (e.g., Van Rijn, 1984; Ribberink, 1998). Values including $k_s = d_{65}$ (e.g., Einstein, 1950), $k_s = 2d_{65}$ (e.g., Engelund and Hansen, 1967), and $k_s = 2.5d_{50}$ (e.g., Nielsen, 1992) have been suggested in the literature. A value of $k_s = 5d_{50}$ is adopted in this study to incorporate large roughness

induced by the thick sheet flow layer (maximum modeled $\delta_s = 16.80$ mm), as suggested by Wilson (1989).

Modeled τ_b consists of fluid and particle shear stress (i.e., $\tau_b = \tau_b^f + \tau_b^s$; see Section 2.1.1.2). The modeled τ_b is extracted at the initial bed level ($z^* = 0$ mm), consistent with the choice in existing numerical modeling work of mobile beds (e.g., Kim et al., 2018) and typical single-phase suspended load models (e.g., Van Rijn, 1987). Notably, the elevation $z^* = 0$ mm exists within the sheet flow layer for the duration of the wave. Extracting τ_b at a constant elevation may impart error due to a time-evolving bed level. However, this method is adopted to exclude a sudden elevation change between cell centers in discrete grids. The maximum bed level change is ∼6 mm, less than ∼1% of the water column depth, thus making comparisons to bed shear stress parameterizations commensurable. The parameterized τ_b, calculated using Eqs. (3.5) - (3.7), is compared to the modeled τ_b and shows good agreements up to $t \sim 24$ s (Fig. 3.7b). In contrast, there is a significant discrepancy at $t > 24.5$ s. The conventional quasi-steady approach utilizes only the free stream velocity, thus the effect of intense sediment suspension cannot be captured. The solid black curve (i.e., $\phi_s = 1\%$) in Figure 3.7c illustrates that dilute sediment suspension continues past $t = 26$ s where near-zero τ_b is observed. The peak of u_∞^f and τ_b occur simultaneously at $t = 24$ s; a phase shift between u_∞^f and τ_b has a negligible effect in this case.

The particle-fluid correlation variable, α_c (Eq. (2.12)), is quantified by the Stokes number, St, and indicates the extent that particles follow fluid velocity fluctuations. If a particle has very small inertia ($St << 1$), the particle will closely follow eddy motion, act as a tracer (e.g., Ferry and Balachandar, 2001; Ferry et al., 2003), and α_c will approach a value of 1, denoting completely passive particles (i.e., no drag-induced turbulence damping; Kranenburg et al., 2014). It is generally accepted that when $St \lesssim 0.2$, corresponding to $\alpha_c \gtrsim 0.97$ (using $B = 0.16$; see Section 2.1.1.1), sediment motion is dictated only by the surrounding fluid (e.g., Balachandar and Eaton, 2010). When $St \gtrsim 0.2$, momentum and energy exchanges between the fluid and sediment phases become important due to particle-fluid interactions.

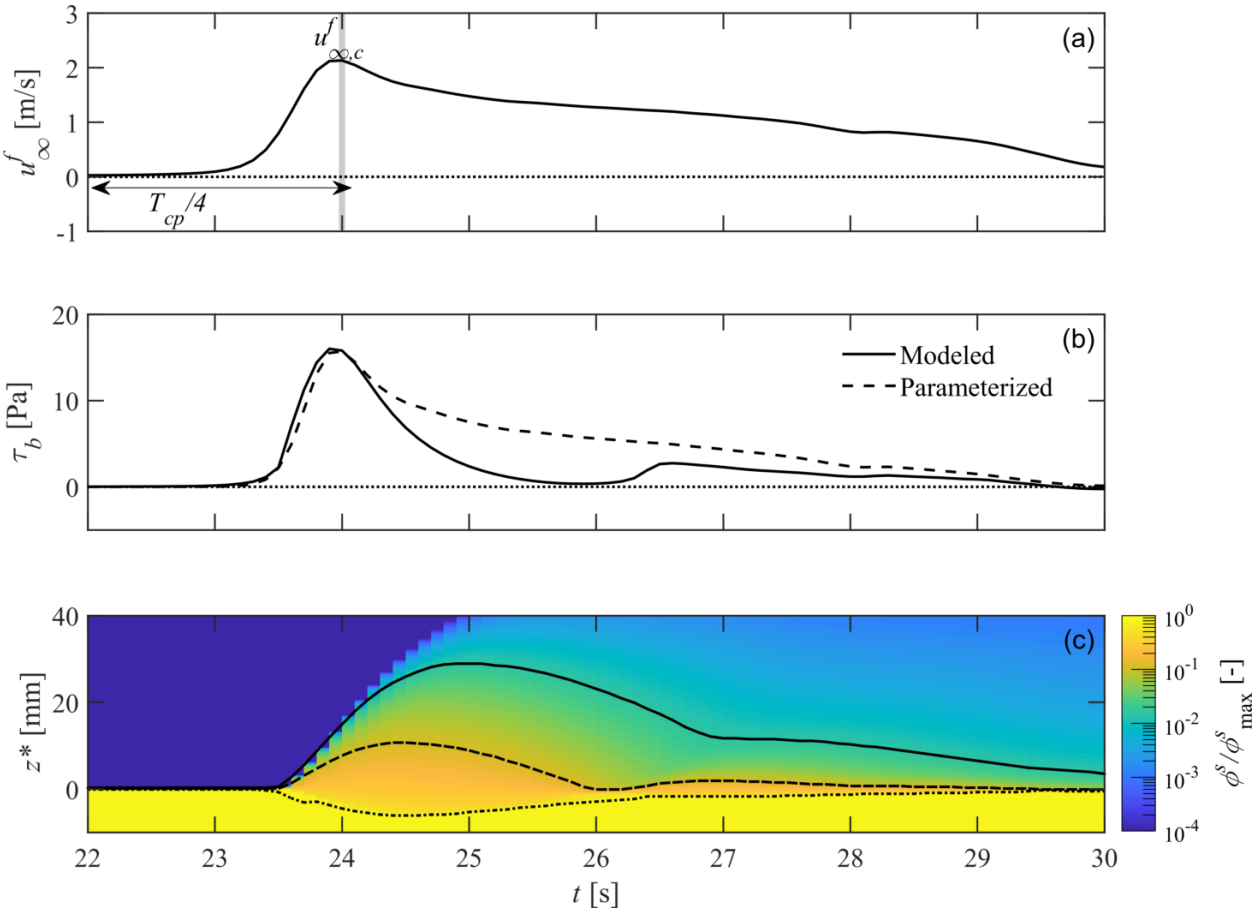

Figure 3.7: (a) Time series of free stream velocity (u^f_∞). The grey vertical line corresponds to the time of maximum free stream velocity ($u^f_{\infty,c}$) and defines T_{cp} in Eq. (3.7). (b) Time series of modeled (black solid curve) and parameterized (i.e., Eqs. (3.5) - (3.7)) (black dashed curve) bed shear stress (τ_b). (c) Time series of modeled, normalized volumetric sediment concentration (ϕ^s/ϕ^s_{max}) shown on a log color scale. The black dotted, dashed, and solid curves represent the immobile bed elevation (defined by a threshold u^s value), the top of sheet flow layer (i.e., $\phi^s = 8\%$), and $\phi^s = 1\%$, respectively.

Within the modeled sheet flow layer (i.e., $z^*_{bed} < z^* < z^*_s$), $St < 0.2$ ($\alpha_c > 0.97$) except between 23.2 s $< t <$ 23.9 s when sediment first begins to move at the bed level and the sheet flow layer thickness is less than 10 mm (Figs. 3.8a - d). Both the maximum St (0.61) and minimum α_c (0.91) occur at $t = 23.5$ s (Figs. 3.8c - d). Notably, the maximum St is significantly higher than the average value of 0.09 within the entire sheet flow layer. These results suggest that turbulence exists in both the fluid and sediment phases and buoyancy effects cannot immediately be neglected. It should be mentioned that the equation for α_c adopted in this study (Eq. (2.12)) may yield larger values compared to the methods shown in Kranenburg et al. (2014).

The gradient Richardson number, Ri, represents the ratio of buoyant to shear turbulent production:

$$Ri = -\frac{g}{\rho^f}\frac{\partial \rho^*}{\partial z}\left(\frac{\partial u^f}{\partial z}\right)^{-2}, \tag{3.8}$$

where ρ^* is the mass averaged density (i.e., $\rho^* = \rho^f\phi^f + \rho^s\phi^s$). When the flux Richardson number (i.e., $R_f = Ri/\sigma_c$) exceeds the threshold value of 0.25, turbulence damping becomes significant due to density stratification (Miles, 1961; Geyer and Smith, 1987; Trowbridge and Kineke, 1994), commonly observed in fine particle flows (e.g., Van Der Ham et al., 2001; Ozdemir et al., 2010; Egan et al., 2020). Applying the flux Richardson number to turbulent, non-dilute, two-phase flows under wave forcing using $\sigma_c = 1$ (see Section 2.1.1.1) is not straightforward and its applicability is not well studied. Thus, R_f is used only as an investigative (proxy) tool in this work to provide insight into the effects of buoyancy and density stratification on turbulence suppression, in combination with analysis of α_c and buoyant/inertial fluxes.

At the peak of modeled τ_b (i.e., $t = 24$ s), the near-bed R_f is below the critical threshold for turbulence damping (Fig. 3.9b5), the inertial flux dominates TKE attenuation relative to the buoyant flux (Fig. 3.9b4), and k^f is on the order of 10^{-2} (Fig. 3.9b3). As the dilute sediment suspension increases, the near-bed R_f continues to increase and exceeds 0.25 at t

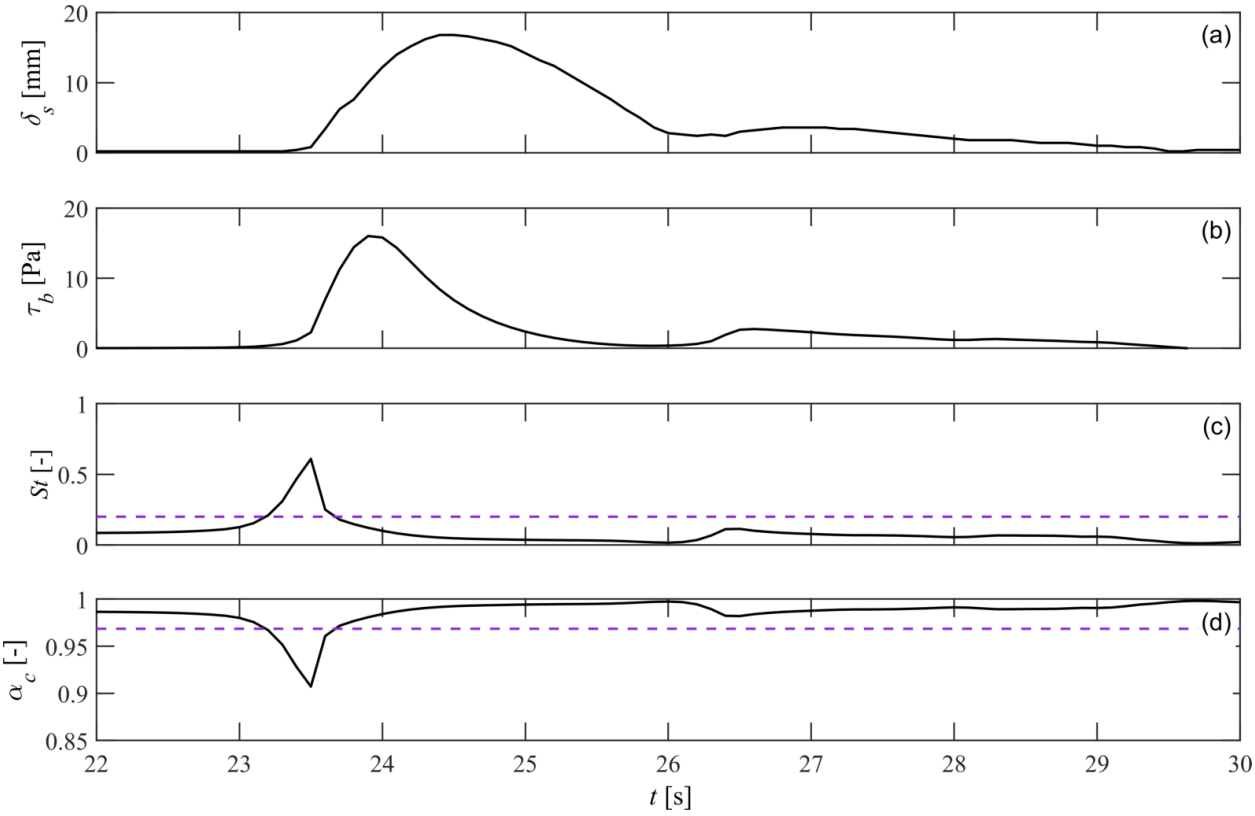

Figure 3.8: Time series of (a) modeled sheet flow layer thickness (δ_s), (b) modeled bed shear stress (τ_b), (c) modeled Stokes number (St) at $z^* = 0$ mm, and (d) modeled particle-fluid correlation variable (α_c) at $z^* = 0$ mm. The purple horizontal dashed lines in (c) and (d) indicate the threshold St and α_c values of 0.2 and 0.97, respectively.

$\sim$ 25.6 s. At $t = 26$ s, R_f remains above 0.25 (Fig.3.9c5), non-negligible u^f still exists (Fig. 3.9c1), and k^f falls by more than an order of magnitude in comparison to its value at the time of peak bed shear stress (Fig. 3.9c3). The drop in k^f leads to reduced turbulent viscosity (not shown here), resulting in near-zero τ_b (Eqs. (2.9), (2.11); Fig 3.9a). At this time of near-zero τ_b, contributions to total TKE dissipation are $f_b \approx 46.1\%$, $f_i \approx 17.8\%$, and $\varepsilon^f \approx 36.1\%$; the buoyant TKE attenuation exceeds inertial effects by more than a factor of 2.5 (Fig. 3.9c4). As the amount of suspended sediment decreases (Fig. 3.9d2), the inertial flux rebounds in dominance relative to the buoyant flux (Fig. 3.9d4), R_f returns below 0.25 (Fig. 3.9d5), and the bed shear stress recovers (Figs. 3.9a). Notably, u^f is similar in magnitude at $t = 26.5$ s (Fig. 3.9d1) compared to $t = 26$ s (Fig. 3.9c1). In considering the balance of buoyant to inertial fluxes, in combination with the flux Richardson number, the results suggest that intense sediment suspension (through density stratification) increases turbulence dampening and contributes to the decrease of bed shear stress to near-zero while a significant velocity gradient still exists. It is worthwhile to mention that energy dissipation is also caused by other mechanisms such as particle-particle interactions (e.g., friction, collisions); however, density stratification plays an important role when significant sediment suspension exists and should not be neglected. The impact of extreme sediment suspension on bed shear stress is not captured by the conventional bed shear stress parameterization following the quasi-steady approach (i.e., Eq. (3.5)). Density stratification effects on τ_b deserve consideration when intense sediment suspension is expected.

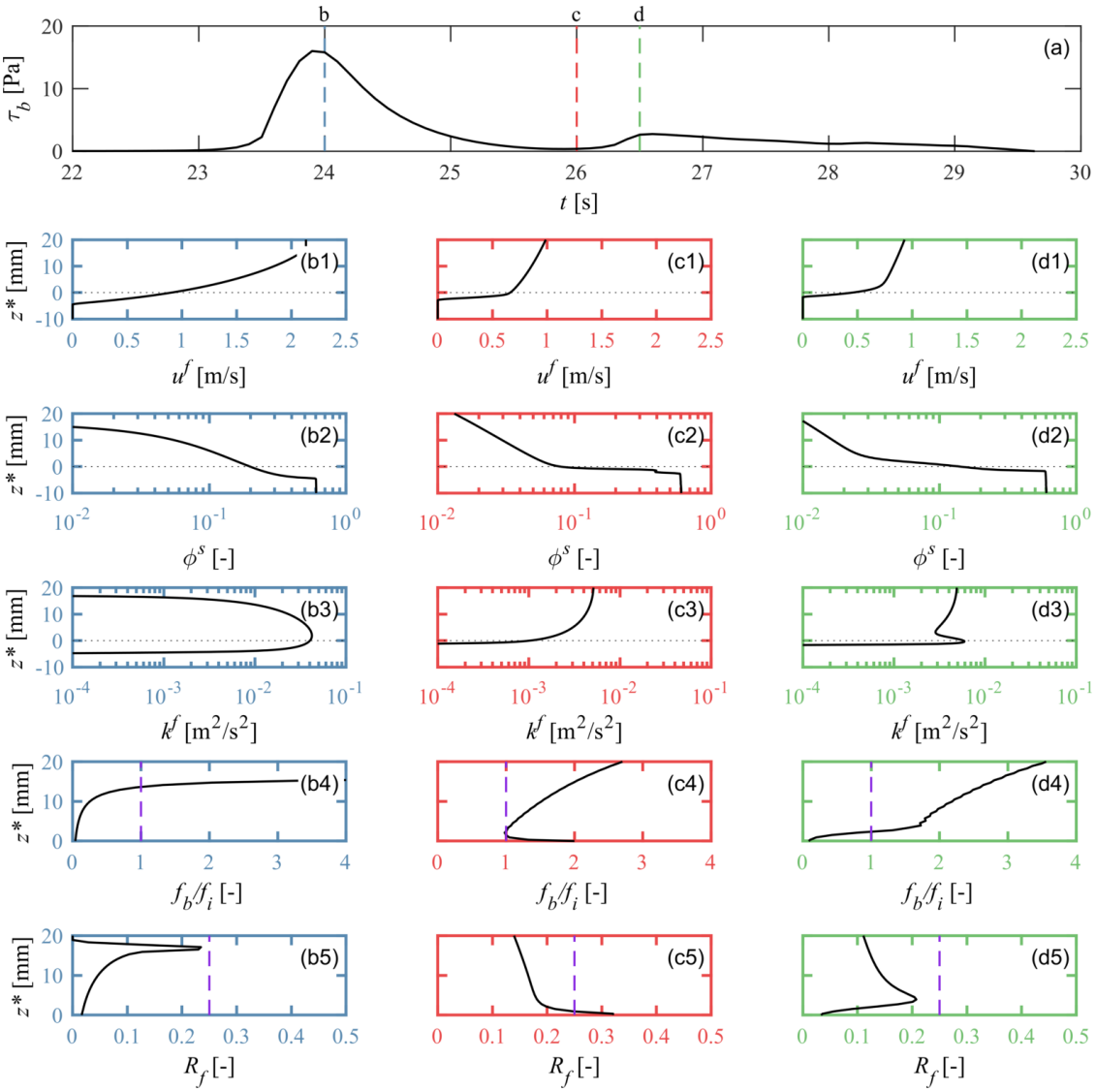

Figure 3.9: (a) Time series of modeled bed shear stress (τ_b). (b) - (d) are modeled profiles of (1) streamwise fluid velocity (u^f), (2) volumetric sediment concentration (ϕ^s), (3) turbulent kinetic energy (k^f), (4) ratio of buoyant to inertial TKE attenuation (f_b/f_i; see Eq. (2.11)), and (5) flux Richardson number (R_f) at (b) $t = 24$ s (blue), (c) $t = 26$ s (red), and (d) $t = 26.5$ s (green), as marked in (a) using the corresponding colored, vertical dashed lines. The purple vertical dashed lines in (b4) - (d4) and (b5) - (d5) indicate the threshold ratio of 1 and $R_f = 0.25$, respectively.

3.4.2 Near-bed velocity

Near-bed sediment velocity profiles are critical in estimating the time-dependent sediment transport rate, $q^s(t)$ (e.g., Wang and Yu, 2007; Kim et al., 2019). However, measured velocities within the sheet flow layer of the BARSED experiment are unusable (Mieras et al. (2019); see Section 3.3). To approximate the sediment velocity within the sheet flow layer, a method to extrapolate the measured u^f at z_s^* to u^s between z_s^* and z_{bed}^* is often adopted (e.g., Sumer et al., 1996; Puleo et al., 2017; Mieras et al., 2019; Kim et al., 2019):

$$u^s(t, z^*) = u^f(t, z_s^*) \left(\frac{z^*(t) - z_{bed}^*(t)}{\delta_s(t)} \right)^{\alpha}, \tag{3.9}$$

where α is a profile shape parameter ($0 < \alpha \leq 1$) and $\alpha = 1$ corresponds to a linear profile. Embedded in this formula is the assumption that u^s at z_s^* is equal to the measured u^f at z_s^*. Model results confirm that u^f and u^s at the maximum δ_s (i.e., $z^* = 10.72$ mm) are nearly identical ($IA > 0.999$, NRMSE = 0.1%; Fig. 3.10a). Suggested values of α under a variety of flow conditions commonly range between $\alpha = 0.5$ and $\alpha = 1.0$ (e.g., Sumer et al., 1996; Pugh and Wilson, 1999; Soulsby and Damgaard, 2005; Puleo et al., 2017; Kim et al., 2019). For instance, Sumer et al. (1996) obtained $\alpha = 0.75$ for sheet flow driven by steady current with the use of light and large grains ($s < 1.27$ and $d_{50} > 2.6$ mm). Puleo et al. (2017) found $\alpha = 0.62$ to be the best-fit compared to velocity profiles measured using an optical current meter in swash flows. Mieras et al. (2019) further demonstrated that q^s is sensitive to the choice of α and Kim et al. (2019) showed a 28.5% variation in net sediment transport rates using $\alpha = 0.5$ versus $\alpha = 1.0$.

The range of $0.3 \leq \alpha \leq 1$ is tested to determine the instantaneous best-fit (i.e, maximum IA) profile shape parameter under the modeled transient wave (Fig. 3.10c - f). Initially, as the sheet flow layer begins to develop, $\alpha = 1.0$ is obtained (Fig. 3.10c). At the maximum δ_s (red vertical dashed line in Fig. 3.10b), α decreases to 0.63 (Fig. 3.10d). The smallest α value of 0.38 is obtained at $t = 25.4$ s (Fig. 3.10e). As δ_s drops to less than 15% of its maximum thickness, α returns to 0.94 (Fig. 3.10f). The minimum IA (maximum NRMSE)

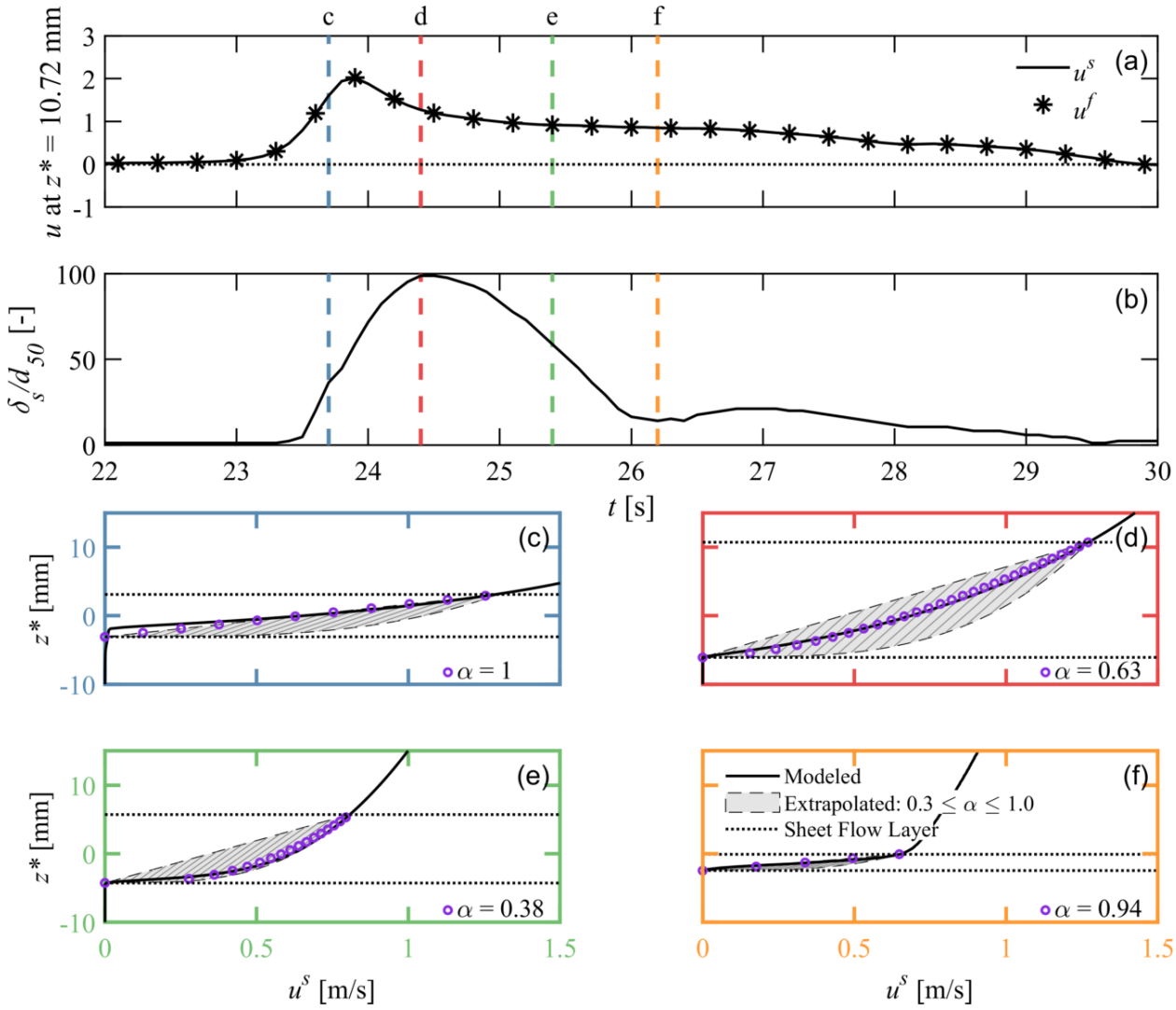

Figure 3.10: Time series of modeled (a) streamwise sediment velocity (u^s) (black solid curve) and streamwise fluid velocity (u^f) (black markers) at $z^* = 10.72$ mm and (b) normalized sheet flow layer thickness (δ_s/d_{50}). (c) - (f) are modeled profiles (black curves) of u^s at (c) $t = 23.7$ s (blue), (d) $t = 24.4$ s (red), (e) $t = 25.4$ s (green), and (f) $t = 26.2$ s (orange), as marked in (a) and (b) using the corresponding colored, vertical dashed lines. The purple symbols represent the extrapolated velocity using the instantaneous best-fit profile shape parameter (α) in Eq. (3.9). The grey hatched bands show the range of extrapolated velocities using time-invariant α values between 0.3 and 1.0.

with the optimal, time-varying α was 0.886 (23.43%) at $t = 23.5$ s, significantly better than those obtained with constant α values of 0.3 ($IA_{min} = 0.614$, $\text{NRMSE}_{max} = 42.97\%$) and 1.0 ($IA_{min} = 0.816$, $\text{NRMSE}_{max} = 27.38\%$) at $t = 23.6$ and 25.7 s, respectively. Values of $\alpha = 0.3$ ($\alpha = 1.0$) tend to overestimate (underestimate) the near-bed u^s, particularly when δ_s is large (small). The extrapolated u^s (i.e., Eq. (3.9)) using the time-varying optimal α value produces an IA of 0.990 and NRMSE of 5.05% (averaged over 23.4 s $< t <$ 29.4 s) when compared with the directly modeled u^s. The shape of the velocity profile within the sheet flow layer changes in time under the transient wave and a constant α value is not recommended.

The flow field in the turbulent boundary layer is characterized by the dimensionless distance from the bed, called the wall unit, z^+ (e.g., Von Kármán, 1931; Pope, 2000). Although the log-law was derived for a fixed solid boundary, it can be successfully applied to a mobile sediment bed (e.g., Pugh and Wilson, 1999) by referencing z^+ to the instantaneous elevation of the immobile bed. Typically, the wall unit is non-dimensionalized by ν^f; in two-phase flow however, ν^f does not account for the effect of particles on energy dissipation. Thus, a modified z^+ at the top of the sheet flow layer (with reference to the instantaneous elevation of the immobile bed) is defined as:

$$z^+ = \frac{\delta_s u_\tau}{\nu^m}, \tag{3.10}$$

where $u_\tau = \sqrt{\tau_b/\rho^f}$ is the friction velocity. The mixture viscosity, ν^m, is defined as (Krieger and Dougherty, 1959):

$$\nu^m = \nu^f \left(1 - \frac{\phi^s_{\text{avg}}}{\phi^s_{\text{max}}}\right)^{-2.5\phi^s_{\text{max}}}, \tag{3.11}$$

where the instantaneous, average sediment concentration, ϕ^s_{avg}, is calculated only within the sheet flow layer (i.e., $z^*_{bed} < z^* < z^*_s$). It should be noted that ν^m (i.e., Eq. (3.11)) is based on dense granular-flow rheology, in contrast the kinetic granular theory applied to SedFoam in this work, and is only applied as a non-dimensionalization method. In the viscous sublayer ($z^+ < 5$), viscous effects dominate and velocity linearly increases with the distance from the bed (i.e., $\alpha = 1.0$). Further away from the bed, the log-law layer ($30 < z^+ < 140$) exists

(Shih et al., 1999) where the velocity follows a logarithmic profile ($\alpha \sim 0.5$). In the outer layer ($z^+ > 140$), the direct effect of viscosity is negligible and the velocity profile slightly deviates from the log-law ($\alpha < 0.5$). In the buffer layer ($5 < z^+ < 30$) , $0.5 < \alpha < 1.0$ is expected. Notably, these layers are defined for clear-fluid, turbulent flow; analysis of the modified wall unit therefore is investigative in nature and occurs only after 23.7 s with the Reynolds number is on the order of 10^6.

The optimal profile shape parameter is initially 1.0 however quickly decreases as u_∞^f increases and z^+ transitions into the log-law and outer layers at $t \sim 23.7$ s (Fig. 3.11). The optimal α decreases until $t = 25.4$ s as the BBL develops (Fig. 3.11b) where the BBL thickness, δ_w, is defined as:

$$\delta_w = z_w^* - z_{bed}^*. \tag{3.12}$$

The optimal α exhibits a near-immediate increase when z^+ falls back into the buffer region at $t \sim 25.8$ s due to the continued decrease in δ_s while δ_w is still increasing. At $t \sim 26.3$ s, z^+ returns to the buffer layer and the optimal α decreases. Once z^+ enters the log-law layer, the optimal α stays more or less constant. As the sediments settle back (decreasing δ_s) at $t > 27$ s, z^+ drops and the optimal α slowly begins increasing at $t \sim 27.7$ s. These results highlight the relationship between the optimal α and z^+ (or δ_s), namely z_s^* is located in different log-law regimes in a transient turbulent boundary layer where the evolution of the sheet flow layer and BBL do not coincide. Secondary flow effects beyond the scope of this work may also contribute to the velocity evolution and optimal α value. The significance of using an appropriate profile shape parameter is further discussed in Section 3.4.3.

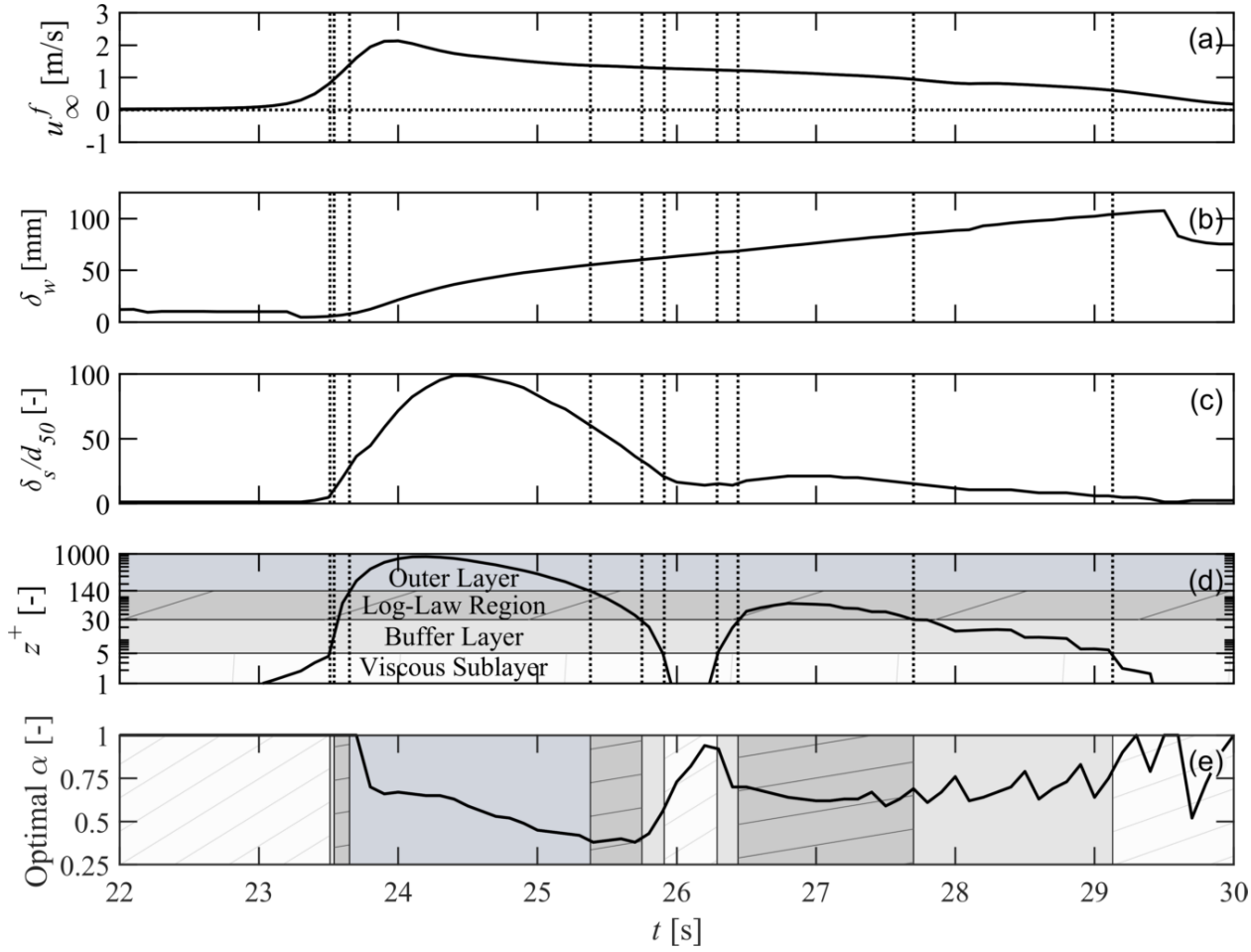

Figure 3.11: Time series of modeled (a) free stream velocity (u_∞^f), (b) BBL thickness (δ_w), (c) normalized sheet flow layer thickness (δ_s/d_{50}), (d) wall unit (z^+) at the top of the sheet flow layer (z_s^*) and (e) optimal profile shape parameter (α). The shading in (d) delineates the viscous sublayer ($z^+ < 5$; white hatched), buffer layer ($5 < z^+ < 30$; grey), log-law region ($30 < z^+ < 140$; dark-grey hatched), and the outer layer ($z^+ > 140$; slate-grey) region. The dotted vertical lines indicate when z^+ transitions into a different regime. The shading in (e) corresponds to regime that z^+ exists in at that time.

3.4.3 Sediment transport

The effect of the profile shape parameter and suspended sediment-induced density stratification on sediment transport are investigated here. The sediment transport rate is calculated by integrating the streamwise sediment flux over the water column as:

$$q^s(t) = \int_{z^*_{bed}(t)}^{z^*_t} \phi^s(t) u^s(t) dz^*, \tag{3.13}$$

where z^*_t represents the top of the model domain. Sediment transport consists of bedload (subscript "bl"), the movement of sediment within the sheet flow layer (i.e., below z^*_s), and suspended load (subscript "ss"), the movement of sediment above the sheet flow layer (i.e., above z^*_s). No subscript represents the total quantity:

$$q^s = q^s_{bl} + q^s_{ss}. \tag{3.14}$$

The sediment transport rate is considerably affected by the velocity of the carrier fluid. For example, a small modulation in wave-averaged velocity under periodic waves can significantly enhance the onshore directed net transport rate by 60 - 300% (Kim et al., 2018, 2019). Critically, estimations of the near-bed velocity in the absence of measurements can significantly change the prediction of q^s_{bl} (Fig. 3.12e). In this study, the q^s_{bl} is on average 1.36 times greater when using a quadratic versus linear profile shape parameter, less than the 1.64 factor reported in Mieras et al. (2019) for a range of periodic skewed-asymmetric waves. Using $\alpha = 0.5$ results in 1.50 times greater gross bedload sediment transport (i.e., time-integrated between 22 - 30 s, $q^s_{bl,g}$) than with $\alpha = 1.0$. When approximating q^s_{bl} by extrapolating the near-bed velocity using Eq. (3.9) with the optimal, time-dependent α (see Section 3.4.2), excellent agreement with the modeled q^s_{bl} is observed ($IA > 0.999$, NRMSE = 1.22%; Fig. 3.12e). When using time-invariant values of $\alpha = 0.5$ and 1.0 in Eq. (3.9) to approximate q^s_{bl}, NRMSE of 5.14% and 13.11% are obtained when compared to modeled q^s_{bl}, respectively. At the peak q^s_{bl} (i.e., $t = 24.1$ s), $\alpha = 0.5$ over-predicts the modeled q^s_{bl} by 17.03% and $\alpha = 1.0$ under-predicts the modeled q^s_{bl} by 21.88%.

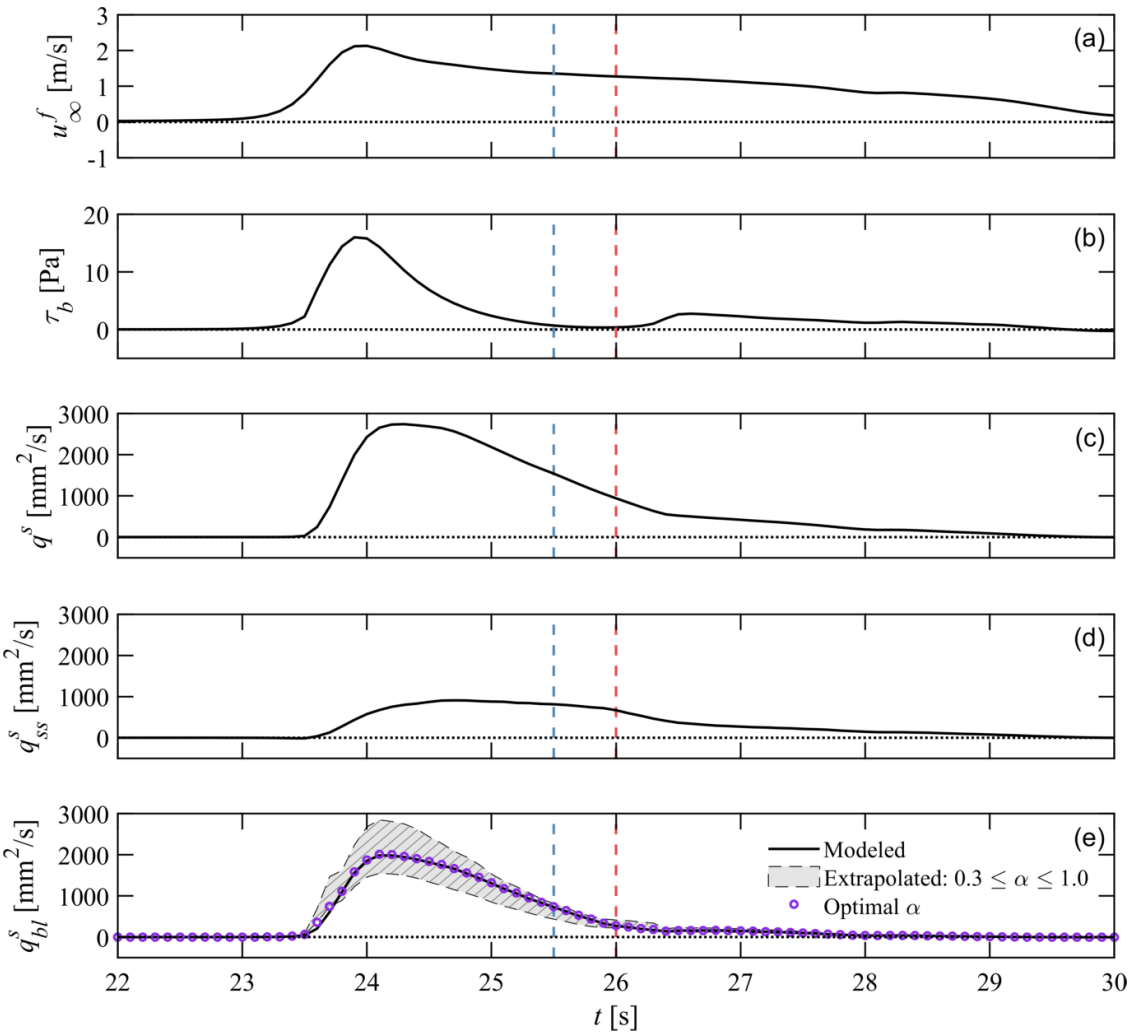

Figure 3.12: Time series of modeled (black curves) (a) free stream velocity (u^f_∞), (b) bed shear stress (τ_b), (c) sediment transport rate (q^s), (d) suspended load sediment transport rate (q^s_{ss}), and (e) bedload sediment transport rate (q^s_{bl}). The purple symbols in (e) are q^s_{bl} using the extrapolated streamwise sediment velocity (u^s) (i.e., Eq. (3.9)) with the instantaneous best-fit profile shape parameter (α) (Fig. 3.11e). The grey hatched band shows the range of parameterized q^s_{bl} using time-invariant α between 0.3 and 1.0. The blue vertical dashed line at $t = 25.5$ s indicates the transition from bedload to suspended load dominant sediment transport. The red vertical dashed line at $t = 26$ s indicates minimum τ_b.

In the model results, bedload dominates the total sediment transport rate until $t = 25.5$ s (Fig. 3.12). It is important to note that it is a drop in q^s_{bl} rather than an increase in q^s_{ss} that leads to the transition from bedload to suspended load-dominant sediment transport. In fact, q^s_{ss} shows minimal change in magnitude between $t \sim 24$ - 26 s, corresponding to the time span in which bed shear stress decreases (Fig. 3.12d). At $t = 26$ s (red vertical dashed line in Fig. 3.12), q^s_{bl} is close to zero at the same time that τ_b reaches its minimum. The maximum q^s_{bl} (at $t = 24.1$ s) slightly trails the maximum τ_b and u^f_∞ (at $t = 24$ s) and leads the maximum q^s (at $t = 24.3$ s) (Fig. 3.12). In contrast, the maximum q^s_{ss} (at $t = 24.7$ s) lags the maximum τ_b, u^f_∞, and q^s. The lag observed in q^s_{ss} may result from ongoing dilute sediment suspension where q^s_{ss} remains within 10% of its maximum until $t = 25.4$ s. The decrease in τ_b reduces q^s_{bl} and results in suspended load-dominant sediment transport. Overall, the suspended load contributes 43.54% of the gross sediment transport (i.e., bedload contributes 56.46%).

3.5 Conclusions

The two-phase Eulerian sediment transport model, SedFoam, was used to numerically investigate sheet flow under a transient wave. 1DV SedFoam was validated with measured fluid velocity and sediment concentration data obtained during the BARSED experiment (Anderson et al., 2017; Mieras et al., 2017, 2019) and yielded good agreement with measured data. Sheet flow layer thickness comparisons showed reasonable agreement.

Through numerical modeling, detailed near-bed sediment transport processes were examined. Investigation of the modeled bed shear stress revealed a limitation of the conventional quasi-steady bed shear stress parameterization. The model results demonstrated that intense sediment suspension may induce stable density stratification that dampens near-bed turbulent kinetic energy and reduces bed shear stress. This phenomenon is not captured by the quasi-steady approach as the effect of density stratification on the free stream velocity

obtained further away from the bed is insignificant.

The modeled near-bed velocity was used to determine the optimal profile shape parameter. It was found that the optimal profile shape parameter is dependent on the dimensionless distance (z^+) from the immobile bed and sheet flow layer thickness. Under the transient wave, the BBL and sheet flow layer evolve in time separately, thus the optimal profile shape parameter varies with time.

Evaluation of the sediment transport rate revealed that the profile shape parameter significantly impacts the estimated bedload, with $\alpha = 1.0$ under-predicting the modeled sediment transport rate by a maximum of 20.01%. Density stratification resulted in decreased bed shear stress and consequently, reduced bedload transport while substantial suspended load sediment transport persisted. This suggests that density stratification plays a key role in mediating the relative contributions of bedload and suspended load and may significantly impact total sediment transport rate estimates.

The analysis presented was based on a single sediment size of $d_{50} = 0.17$ mm and trial (Run 92, S1TR10). SedFoam characterizes buoyancy using calculated values rather than physically-resolving buoyancy; future work should address model shortcomings in resolving inner boundary layer dynamics. A comprehensive understanding of sheet flow under transient wave conditions requires further investigation with a variety of sediment sizes and wave shapes.

3.6 Acknowledgements

This study was partially supported by the California Department of Parks and Recreation Division of Boating and Waterways (C1670006). Numerical simulations presented in this study were carried out using the Hoffman2 cluster at the University of California, Los Angeles. Data used in this chapter were obtained through DesignSafe-CI (`https://doi.org/10.17603/DS2BW9W`) and the case setup to reproduce the results are publicly available on GitHub

(https://github.com/mpdelisle/BARSED-S1TR10). The authors would like to thank Dr. Tian-Jian Hsu and Ali Salimi-Tarazouj for their personal communications that significantly improved this chapter.

Chapter 3 was published as "Numerical investigation of sheet flow driven by a near-breaking transient wave using SedFoam" by the authors: Marie-Pierre C. Delisle, Yeulwoo Kim, Ryan S. Mieras, and Timu W. Gallien, in the European Journal of Fluid Mechanics – B/Fluids, Volume 96, Pages 51–64, Copyright Elsevier (2022).

CHAPTER 4

Dam-break driven swash and beach groundwater interactions

4.1 Background

Global sea levels are projected to increase by 0.46 to 1.89 m by 2100 (Fox-Kemper et al., 2021). SLR will substantially increase both the frequency and intensity of extreme coastal events (i.e., energetic waves, high spring tides, and storm surge) interacting with infrastructure (Cayan et al., 2008; Heberger et al., 2009; Mastrandrea and Luers, 2012). The compounding effects of SLR, dynamic water level components, and coastal change (e.g., beach erosion, cliff retreat) can disproportionately amplify coastal risk and flood extent (Prime et al., 2015; Vitousek et al., 2017). When projected population growth and coastal migration are accounted for, approximately 4.2 million people in the continental United States will be at risk of inundation with 0.9 m of SLR by 2100; the number increases to 13.1 million people if the sea level rises 1.8 m (Hauer et al., 2016). Improved understanding of beach and nearshore dynamics is essential for future risk assessment (Horn, 2002; Gallien, 2016).

The swash zone, the intermittently wet and dry region of the beach that migrates across the beach face with the tide, is fundamental to coastal flood vulnerability. The surface-subsurface dynamics occurring within the swash zone create a highly complex flow region characterized by multi-phase, transient, turbulent, and interdependent processes. Swash zone hydrodynamics consist of three primary components: surface flows (i.e., swash), surface-subsurface flow interactions, and beach groundwater. From the surface perspective, wave

runup and overtopping are more sensitive to SLR than tides (Arns et al., 2017) and overtopping is expected to increase exponentially with SLR (Almar et al., 2021). Typically, coastal flood assessment and planning focus only on surface flows and neglect beach groundwater contributions to coastal flood risk (Rotzoll and Fletcher, 2013). Including SLR-induced groundwater inundation dynamics in a model of Waikiki, Hawaii (USA) more than doubled the predicted flooding extent as compared to overland flooding alone (Rotzoll and Fletcher, 2013). Coastal groundwater levels will increase at approximately the same rate as the sea level (Horn, 2006; Bjerklie et al., 2012; Rotzoll and Fletcher, 2013; Hoover et al., 2017) and rising groundwater levels will inevitably breach submerged infrastructure (e.g., basements, water, sewage, and electricity lines) posing significant infrastructure complications. Beach groundwater tables can rise more than 1 m during large wave and surge events (Housego et al., 2021). In low-lying coastal communities, groundwater emergence and subsequent infrastructure damage is expected (Habel et al., 2017). Notably, the compounding impacts of surface and subsurface flows on swash zone behavior remains unresolved.

A key characteristic of the swash zone is the exchange of water between the surface and subsurface through infiltration/exfiltration. Swash infiltration and exfiltration depend on a variety of beach and hydrodynamic factors, not limited to beach porosity (e.g., Packwood, 1983), tidal stage (e.g., Heiss et al., 2014), and depth to the groundwater table (e.g., Bakhtyar et al., 2011). Conventional swash zone infiltration/exfiltration research has primarily focused on characterizing and quantifying sediment transport impacts (e.g., Bagnold, 1940; Duncan, 1964; Harrison, 1969; Waddell, 1976; Packwood, 1983; Turner, 1993; Turner and Nielsen, 1997; Turner and Masselink, 1998; Butt et al., 2001; Nielsen et al., 2001; Austin and Masselink, 2006a; Masselink and Turner, 2012; Jamal et al., 2014). Infiltration, exfiltration, and beach characteristics significantly impact boundary layer dynamics and runup, however the role and relative dominance of these processes is uncertain (Horn, 2006; McCall et al., 2012; Jamal et al., 2014; Briganti et al., 2016). When air becomes entrapped between the infiltrating wetting front and the beach groundwater table, infiltration is reduced (Horn, 2002,

2006; Steenhauer et al., 2011). Infiltration decreases runup extent and must be considered to accurately reproduce swash observations (Pintado-Patiño et al., 2015). Improved knowledge of the bi-directional relationship between surface and subsurface flows is fundamental to quantifying and characterizing swash zone response to evolving ocean levels and wave climatology.

A growing body of research suggests that the beach groundwater table plays a key role in seepage processes (e.g., Gillham, 1984; Turner, 1993; Masselink and Li, 2001; Bakhtyar et al., 2011; Masselink and Turner, 2012; Rotzoll and Fletcher, 2013; Sous et al., 2013). A shallow (deep) groundwater table typically leads to exfiltration (infiltration) and promotes erosion/offshore (accretion/onshore) sediment transport (e.g., Bagnold, 1940; Turner and Masselink, 1998; Baldock and Holmes, 1999; Masselink and Li, 2001; Bakhtyar et al., 2011). The capillary fringe, which forms immediately above the groundwater table when tension saturation pulls groundwater upwards, impacts groundwater table oscillations over a range of frequencies, including those of wave and tidal fluctuations (Waddell, 1976; Turner and Nielsen, 1997; Nielsen and Perrochet, 2000; Werner and Lockington, 2003; Horn, 2006). A capillary fringe limits beach groundwater storage capacity and can cause a disproportionate and near-instantaneous groundwater table response to infiltration in cases where the capillary fringe reaches the surface (i.e., reverse Wieringermeer effect; Gillham, 1984; Turner, 1993). Numerical models that do not characterize capillarity and groundwater flow over-estimate infiltration, which in turn may lead to the misrepresentation and under-prediction of swash runup Li et al. (1999); Pintado-Patiño et al. (2015).

Interactions between surface flows and the beach groundwater table must be resolved to accurately model the entirety of the swash zone (e.g., Elfrink and Baldock, 2002). The phase-resolving numerical model called BeachWin (Li et al., 1997, 2002) simulates wave motion effects on groundwater flow using the nonlinear shallow water (NLSW) equations for surface flow partially-coupled with the Laplace equation for groundwater flow. The model is able to reproduce high-frequency water table fluctuations but is limited in that only sat-

urated groundwater flow is considered using the Laplace equation. Similarly, Perera et al. (2019) weakly coupled the NLSW and Laplace equations for surface and subsurface flow, respectively; the model agreed reasonably well with experimental groundwater table elevations, however infiltration effects on the bottom boundary layer could not be resolved. Desombre et al. (2012) simulated flow through a beach using the Reynolds-averaged Navier-Stokes (RANS) equations for surface flow and the Darcy-Brinkman-Forchheimer formulation for groundwater flow, however, capillarity was neglected and only the main subsurface flow characteristics could be reasonably reproduced. Bakhtyar et al. (2011) loosely coupled the Navier-Stokes equations for surface flow with a groundwater flow model based on SEAWAT-2000 (Guo and Langevin, 2002); differences between the numerical model and experimental data were attributed to capillary fringe exclusion. The volume-averaged RANS model COBRAS was extended by Hsu et al. (2002) to include both surface and subsurface flow; porous flow is characterized with the semi-empirical Forchheimer equation. Pintado-Patiño et al. (2015) showed that modified COBRAS is capable of simulating the influence of beach permeability and porosity on swash infiltration/exfiltration, however it does not fully represent groundwater flow processes. In particular, neither air nor sediment phases are resolved in the model. Rather, the beach is characterized by an effective porosity and phenomena such as air bubble entrapment in the subsurface are not accounted for. Several OpenFOAM solvers can simulate free surface water waves over porous media using the volume of fluid approach (e.g., olaFlow (Higuera et al., 2014), waves2Foam (Jensen et al., 2014)); both olaFlow and waves2Foam have been validated for porous coastal structure applications. However, these models simplify the beach subsurface by using porosity to represent sediment. Two-phase models that can explicitly model high-frequency free-surface fluctuations, directly account for sediment, and include bi-directional surface-subsurface feedback are necessary to accurately replicate swash-groundwater interactions in the swash zone.

In this study, a free surface resolving Eulerian two-phase numerical model is developed in the OpenFOAM framework by modifying the existing solver olaFlow (Higuera et al.,

2014) and combining it with elements (primarily the drag term) of SedWaveFoam (Kim et al., 2018). SedWaveFoam resolves the free surface wave field and full vertical profiles of fluid and sediment transport processes using the Reynolds-averaged Eulerian two-phase flow equations. It has been validated for monochromatic non-breaking waves (Kim et al., 2018), asymmetric near-breaking waves (Kim et al., 2019), and shoaling waves (Kim et al., 2021). However, SedWaveFoam is currently only capable of modeling flows over saturated sediment beds. The widely-used, comprehensive solver, olaFlow, enables wave generation and absorption and the ability to simulate porous media; olaFlow does not explicitly model the sediment phase and approximates sediment properties through porosity.

The purpose of this study is to present a novel numerical modeling strategy capable of simultaneously resolving the free surface and porous media flow. The model is validated with bore-drive swash measurements collected in a laboratory flume reported by Kikkert et al. (2013). Section 4.2 outlines the numerical model, experimental setup, and model setup. Section 4.3 presents model validation and main flow results. Discussion of the groundwater response to swash, groundwater circulation, and swash response to groundwater conditions are included in Section 4.4. Section 4.5 summarizes the main conclusions of this study.

4.2 Methods

4.2.1 Numerical model

In this study, the two-phase model, SedOlaFlow (Delisle et al., in revision), is developed and used to simulate swash–groundwater flows driven by monochromatic and irregular waves. A description of the numerical model can be found in Section 2.2 with more detailed description in (Delisle et al., in revision).

4.2.2 Experimental Setup

A series of wave flume experiments conducted at the Fluid Mechanics Laboratory (University of Aberdeen, Scotland) are used for model validation (Kikkert et al., 2013). Bore-driven swash events were generated in a 20 m × 0.45 m × 0.9 m (length × width × depth) wave flume. A 1 m × 0.45 m (length × width) water reservoir enclosed by a movable gate was filled to a depth of $h_d = 0.6$ m. A 4.2 m long flat, horizontal section was immediately adjacent to the gate and a 1:10 fixed beach profile was constructed 4.2 m to 10.8 m away from the gate. The initial water depth on the flat, horizontal section and within the beach was $h_0 = 0.062$ m. The gate was lifted at high speed (∼4 m/s) and generated a plunging breaker that evolved into a ∼0.25 m bore with a speed of ∼2.0 m/s before reaching the beach slope and initiating swash motion. Permeable beach experiments were conducted using either gravel ($d_{50} = 8.41$ mm) or coarse sand ($d_{50} = 1.32$ mm); the top 30 mm of the beach was cemented using a dilute water-cement mixture (Steenhauer et al., 2011; Kikkert et al., 2013) to create an immobile beach surface and permeable layer. The initial beach groundwater level was maintained by a weir extending 0.5 m beyond the end of the beach.

Simultaneous flow depth and velocity profile measurements were recorded at six cross-shore locations (x = -1.802 m, 0.072 m, 0.772 m, 1.567 m, 2.377 m and 3.177 m) at 13.5 Hz with laser induced fluorescence (LIF) and cross-correlation particle image velocimetry (PIV), respectively. The experimental x'-z' coordinate system is defined by the x' (z') axis parallel (perpendicular) to the beach slope (see Section 4.2.3 for details). The combined PIV-LIF system had a spatial resolution (random error) of 0.1–0.3 mm (0.1–0.3 mm) and 1–2.5 mm (5–15 mm/s) for flow depth and velocity, respectively. Ensemble-averaged and turbulence measurements were calculated from 50 (15) identical swash events for the gravel (sand) beach. Swash did not reach the most landward sensor during the gravel beach trials (i.e., no measurements recorded at $x = 3.177$ m). Readers are directed to Kikkert et al. (2012, 2013) for additional experimental details.

4.2.3 Model Setup

A two-dimensional (2DV) model domain is created to replicate the experimental setup described in Section 4.2.2 (Fig. 4.1). The modeled bed-parallel (x') and bed-normal (z') axes are defined as positive onshore and upward, respectively, as are the gravity-normal (x) and gravity-parallel (z) axes used for analysis. The origin of both coordinate systems is at the intersection of the initial water surface and beach face. The gate motion is not modeled; instead, the dam-break is produced by gravity at $t = 0$ s.

The mesh is first constructed with a 11.6817 m (width) $\times$ 2.1571 m (height) grid. Regions outside of the experimental flume (light grey regions in Fig. 4.1) are then removed using the OpenFOAM tool snappyHexMesh (Jackson, 2012). Various mesh setups with uniform and irregular grid spacing between $dx = 0.5$–10 mm and $dz = 0.5$–10 mm were generated to test sensitivity to the grid resolution. The instantaneous water depth and depth-averaged velocity converged to similar results using grid resolutions of $dx \leq 4$ mm and $dz \leq 2$ mm (not shown here). Gravity-normal (x-z) and bed-parallel (x'-z') model grid orientations were also tested. The x-z grid orientation case over-predicted the water depth and under-predicted backwash velocity magnitudes compared to the x'-z' grid orientation, indicating that the bed-parallel grid orientation better captures swash processes such as infiltration and drag. Thus, the bed-parallel, uniform $dx = 4$ mm $\times$ $dz = 2$ mm computational grid (1.46 million grid cells) is selected for model validation and further analysis.

A wall boundary is imposed along the bottom of the computational domain; no-flux boundary conditions are applied for scalar and bottom-normal velocity components and a no-slip condition is applied for bottom-parallel velocities. It should be noted that the no-slip boundary condition in the beach region is of minor importance as it exists below an immobile sediment bed. The top boundary is specified with an atmospheric boundary condition, the inlet/outlet (y-z) planes are specified as no-flux boundaries for scalar and velocity components, and the lateral (x-z) planes are specified as empty boundaries in OpenFOAM.

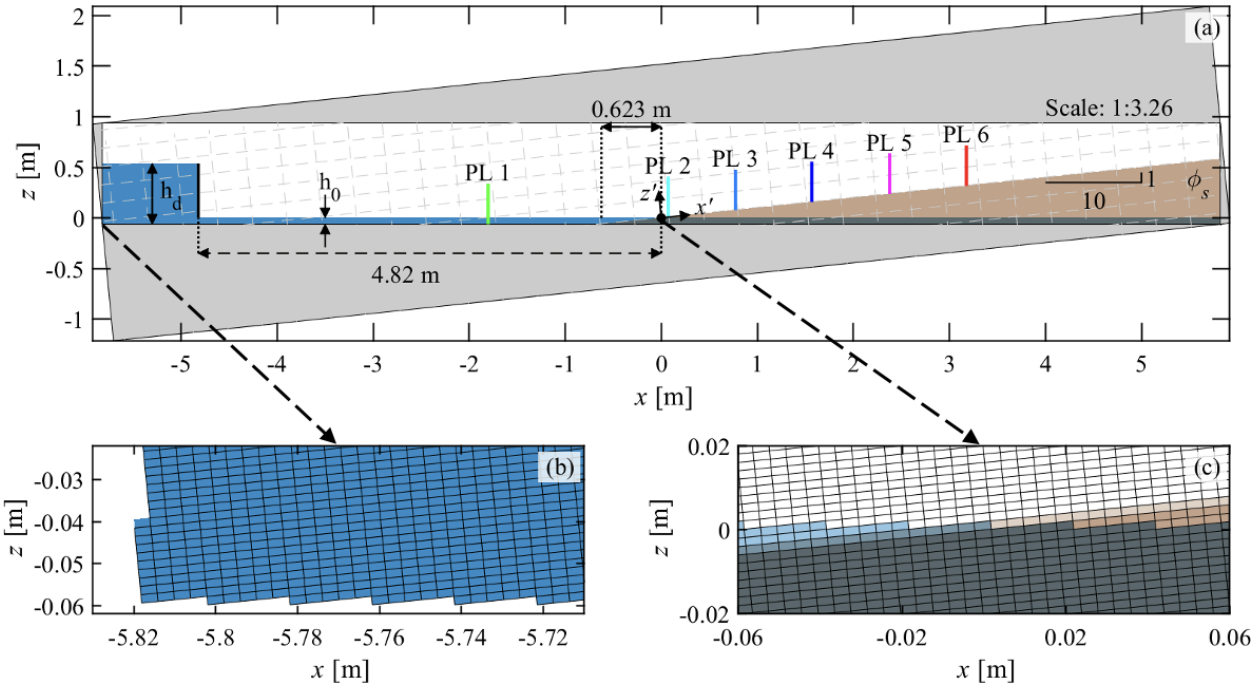

Figure 4.1: (a) Numerical setup and initial conditions replicating the Kikkert et al. (2013) permeable beach experiments. Air, surface water, groundwater, and sediment phases are white, blue, dark grey, and tan, respectively. The origin of both coordinate systems is at the intersection of the initial water surface and beach face (black circle), 0.621 m and 4.82 m from the beach toe and gate, respectively. h_d = 0.6 m is the initial water depth in the reservoir and h_0 = 0.062 m is the initial water depth in front of and within the beach. The beach volumetric sediment concentration is ϕ_s. The colored vertical lines indicate the cross-shore deployment locations of the PIV-LIF (PL) systems at x = -1.802 m (PL 1), 0.072 m (PL 2), 0.772 m (PL 3), 1.567 m (PL 4), 2.377 m (PL 5), and 3.177 m (PL 6). The surrounding light grey regions are not included in the numerical domain as shown by the enlarged views of the (b) lower left corner and (c) origin of the domain.

An initial model timestep of 10^{-6} s is used and then dynamically adjusted by the Courant-Friedrichs-Lewy condition with a courant number of 0.2. The numerical model required a wall-clock time of ∼17 hours using 14 processors (2.3 GHz Intel Xeon Gold 6140) for the 10 s run.

The reported experimental d_{50} values, 8.4 mm (gravel) and 1.3 mm (sand), and specific gravity of 2.65 are specified in the model. The vertical profile of volumetric sediment concentration, ϕ_s, is prescribed as:

$$\phi^s = \frac{\phi_0^s}{2}\{1 + \tanh[2400(z_b - z)]\} \tag{4.1}$$

where ϕ_0^s is the maximum sediment concentration and z_b is the beach interface. Steenhauer et al. (2011) reported an effective porosity of $\eta = 0.3$ for the gravel and sand sediments used by Kikkert et al. (2013). However, Pintado-Patiño et al. (2015) found $\eta = 0.2$ to be ideal for numerical modeling of the gravel sediment. Values between $0.6 \leq \phi_0^s \leq 0.8$ were tested as the model is highly sensitive to ϕ^s, which encompasses beach characteristics such as η, packing density (D), and sediment shape. For both the gravel and sand cases, $\phi_0^s = 0.7$ best matched the experimental data (see calibration below) which follows the relationship between packing density and porosity ($D = 1 - \eta$), and is chosen for further analysis. Notably, $\phi_0^s = 0.7$ is slightly larger than the 0.6–0.64 values typically used in SedFoam and SedWaveFoam numerical modeling (e.g., Chauchat et al., 2017; Kim et al., 2018, 2019, 2021; Delisle et al., 2022). These previous studies assumed uniform packing of perfectly spherical particles; heterogeneity (e.g., in shape or size) reduces pore space, reflecting as in increase in ϕ^s. It is also possible that the experimental cementing technique to immobilize the top 30 mm of the beach (see Section 4.2.2) reduced beach porosity (i.e., increased ϕ^s). Although both the gravel and sand cases are defined by the same ϕ_0^s, larger sediment size will result in an increased gravel beach permeability as compared to the sand beach.

The model is calibrated to optimize the normalized root mean square error, NRMSE, and model skill (i.e., index of agreement, IA) for the instantaneous water depth (h) and depth-averaged bed-parallel velocity ($u_{x'}$). NRMSE represents the mean of squared errors

with reference to the absolute maximum of the measured data. The IA represents the ratio of the mean squared error and the potential error (Willmott, 1981):

$$IA = 1 - \frac{\sum_{i=1}^{T} (P_i - O_i)^2}{\sum_{i=1}^{T} \left[\left(\left| P_i - \overline{O} \right| \right) + \left(\left| O_i - \overline{O} \right| \right) \right]^2}, \tag{4.2}$$

where T is the total number of timesteps. P and O are the predicted (i.e., modeled) and observed (i.e., measured) values, respectively. Model results were interpolated to match experimental timesteps, resulting in $T = 102$ (for h and $u_{x'}$) and $T = 135$ (for shoreline position). Values of zero and unity for IA correspond to no agreement and complete agreement, respectively.

The model is calibrated using the Darcy-Forchheimer drag coefficients α and β in Equation (2.30). Calibrated values of α and β exist in the literature (e.g., Liu et al., 1999; Hsu et al., 2002; Lara et al., 2008); however, most were optimized for porous elements with d_{50} significantly larger than 8.4 mm and for waves interacting with porous structures. Various combinations of ϕ_0^s, α, and β were systematically tested to determine model sensitivity (Fig. 4.2). The numerical model is most sensitive to ϕ_0^s, however α, β, and ϕ_0^s are interdependent thus all possible combinations must be tested to rigorously determine the optimal values. The experimental porosity of 0.3 provided a basis to test $0.6 \leq \phi_0^s \leq 0.8$ for both the gravel and sand cases. Based on previous numerical calibration for the gravel case (Pintado-Patiño et al., 2015), $0.1 \leq \alpha \leq 150$ and $0.001 \leq \beta \leq 10$ were tested for the 8.4 mm gravel beach. Ranges of $10 \leq \alpha \leq 500$ and $1 \leq \beta \leq 35$ were tested for the 1.3 mm sand beach, falling on both ends of reported values for larger sediment sizes (e.g., Liu et al., 1999; Hsu et al., 2002; Lara et al., 2008). The model skill was used to inform calibration efforts and reduce computational cost.

The combined h and $u_{x'}$ average NRMSE values demonstrate that the model is sensitive to all three parameters α, β, and ϕ_0^s (Fig. 4.2). The dark blue cells indicate the best agreement with experimental data while dark red cells indicate the worst agreement of tested

combinations for the gravel and sand cases separately. SedOlaFlow is more sensitive to the nonlinear drag component, β, as compared to the linear drag component, α, likely because flow is mostly turbulent within the beach. For both cases, $\phi_0^s = 0.7$ agrees best with experimental data and is chosen as the model packing density, corresponding to the experimental porosity of 0.3. The optimal α and β values are smaller for the gravel case ($\alpha = 1$, $\beta = 0.05$) as compared to the sand case ($\alpha = 400$, $\beta = 20$), corresponding to increased drag observed for smaller sediment. Notably, the optimal values for the gravel case are similar to the calibrated values used by Pintado-Patiño et al. (2015) ($\alpha = 10$, $\beta = 0.1$) for the same case. Table 4.1 summarizes the number of tests, range of α and β values tested, and the resulting NRMSE and IA values for h and $u_{x'}$ for the $\phi_0^s = 0.7$ cases. IA and NRMSE values are calculated by averaging the individual skill values at each swash zone PIV-LIF sensor location (i.e., PIV-LIF's 2–6) for t = 0–10 s. The optimal parameters chosen for model validation are indicated by the * in Table 4.1.

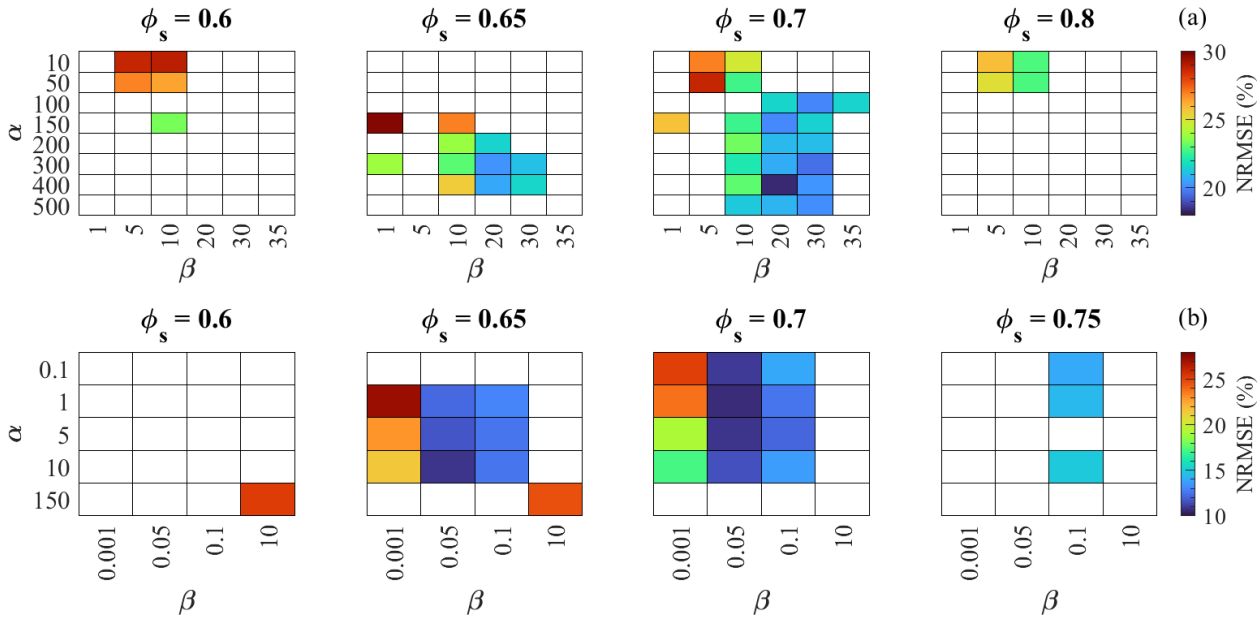

Figure 4.2: Mean of averaged h and $u_{x'}$ NRMSE values for (a) sand and (b) gravel cases for tested combinations of ϕ_0^s, α, and β. Dark blue (red) corresponds to the lowest (highest) NRMSE values, or best (worst) agreement with experimental results.

Table 4.1: Summary of simulated tests, α and β values, and averaged h and $u_{x'}$ model skill values using $\phi_0^s = 0.7$. IA and NRMSE values are calculated by averaging the individual skill values at each swash zone PIV-LIF sensor location (i.e., PIV-LIF's 2–6) for $t = 0$–10 s. The * indicates the optimal parameters for the specified grain size.

d_{50} (mm)	Tests	α	β	h_{IA}	h_{NRMSE} (%)	$u_{x',IA}$	$u_{x',\mathrm{NRMSE}}$ (%)
1.3	23	10–500	1–35	0.82–0.96	12.0–23.5	0.67–0.86	26.0–34.0
1.3*	1	400	20	0.96	12.1	0.88	24.7
8.4	12	0.1–10	0.001–0.1	0.80–0.97	12.1–24.4	0.90–0.98	9.8–25.8
8.4*	1	1	0.05	0.98	11.6	0.98	9.80

4.3 Results

Flows are separated into surface (i.e., uprush/backwash) and subsurface (i.e., infiltration/exfiltration) components. Experimental data from Kikkert et al. (2013) provides only swash surface flow measurements; the numerical model performance is evaluated by comparing the model results to measured water depth and bed-parallel depth-averaged flow velocity at each swash zone sensor location, in addition to the evolving shoreline position. Subsurface processes are qualitatively compared to the data reported by Steenhauer et al. (2011) for the same experiment, providing numerical model confidence.

Model results are evaluated based on NRMSE and IA. Table 4.2 presents the results for the water depth and bed-parallel depth-averaged flow velocity for the calibrated gravel and sand cases at each swash zone sensor location. Videos of the numerical simulations for both cases are provided as Supporting Information. The instantaneous h is further compared at each swash zone PIV-LIF location (Fig. 4.3). In general, the numerical model reproduces the rapid rise in h followed by an elongated and asymmetric decrease, with reduced h asymmetry observed in the landward direction. Differences in h between the gravel and sand cases increase landwards. Most notably, the larger grain size in the gravel case leads to increased

infiltration (reduced h) and swash does not reach the most landward sensor (PIV-LIF 6). Excellent agreement between the modeled and measured h is observed for $t \lesssim 7$ s for both the gravel and sand cases. Slight over-prediction of h is observed during swash backwash at the most seaward swash sensor for the gravel case (Fig. 4.3b1), with more significant over-prediction of h observed at the most seaward swash sensor locations for the sand case (Fig. 4.3a1-a2). This suggests an under-prediction in infiltration and could be corrected by modifying the drag coefficients α and β. However, these drag coefficients were optimized to improve the overall model performance, rather than solely h. Overall, the model reproduces h well with $IA \geq$ of 0.97 (0.92) and average NRMSE $\leq$ 14.1% (17.0%) for the gravel (sand) case.

Table 4.2: Model IA and NRMSE for the water depth and depth-averaged flow velocity for the calibrated sand (d_{50} = 1.3 mm, α = 400, β = 20) and gravel (d_{50} = 8.4 mm, α = 1, β = 0.05) cases.

d_{50} (mm)	x [m]	h_{IA}	h_{NRMSE} (%)	$u_{x',IA}$	$u_{x',\mathrm{NRMSE}}$ (%)
1.3	0.072	0.92	16.95	0.85	31.84
	0.772	0.93	16.08	0.93	19.36
	1.567	0.98	9.81	0.91	21.23
	2.377	0.99	7.28	0.89	22.37
	3.177	0.97	10.57	0.79	28.67
8.4	0.072	0.97	11.46	0.98	9.92
	0.772	0.99	7.60	0.99	8.31
	1.567	0.98	13.07	0.97	11.39
	2.377	0.97	14.08	0.98	9.57
	3.177				

The modeled, instantaneous $u_{x'}$ is compared to measured data at the swash zone sensor locations (Fig. 4.4). The model reproduces the asymmetry between the larger uprush and

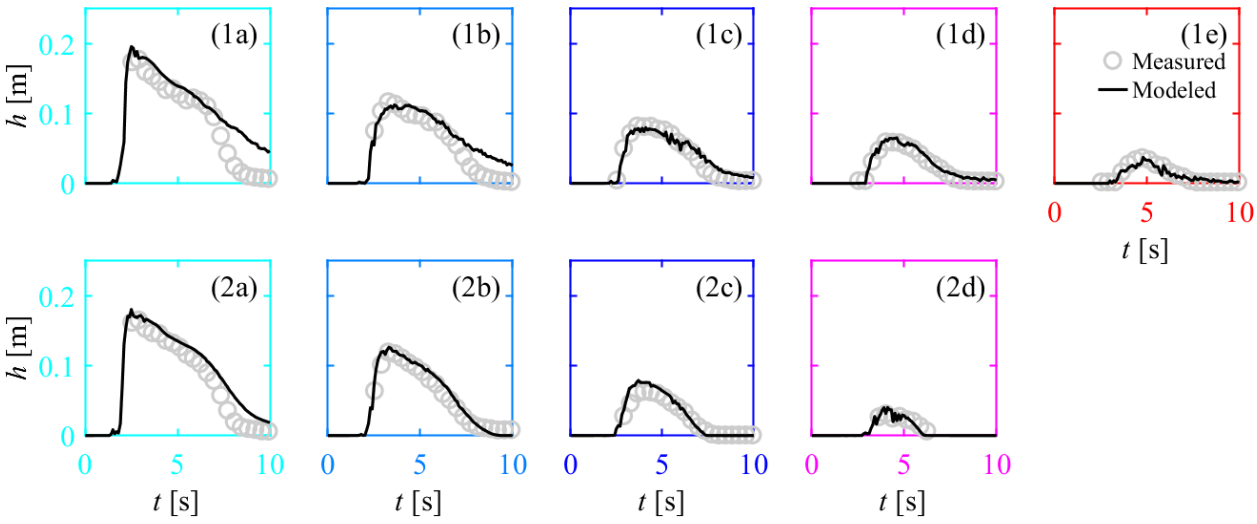

Figure 4.3: Time series of measured (open grey markers) and modeled (black solid curve) water depth (h) for the (a) sand and (b) gravel cases at (1) PL 2 (cyan), (2) PL 3 (light blue), (3) PL 4 (dark blue), (4) PL 5 (pink), and (5) PL 6 (red) corresponding to the swash zone sensor locations shown in Fig 4.1.

smaller backwash bed-parallel flow velocities. Sharp drops in the modeled velocity (e.g., Fig. 4.4b2 at $t = 2.3$ s) are associated with air bubbles within the bore tip (e.g., Fig. 4.4b5). The time of flow reversal (i.e., when $u_{x'} = 0$) is well-captured by the model. In the gravel (sand) case, the modeled time of flow reversal occurs within 0–0.3 s (0.1–0.3 s) of the experimental flow reversal time. Maximum backwash velocity magnitudes are slightly under-predicted for the gravel case at the most seaward locations (Fig. 4.4b1-b3). This may be partially related to the fixed α and β drag coefficients used in the model (Torres-Freyermuth et al., 2013). Agreement with measured data remains high with $IA \geq 0.97$ and NRMSE $\leq$ 11.4% for all gravel beach swash sensors. Maximum backwash velocity magnitudes for the sand beach are significantly under-predicted (Fig. 4.4a1-a5). Over-prediction of the water depth at the most seaward sensors (Fig. 4.3a1-a2) may contribute to the under-estimation of velocity magnitudes. The results suggest that the numerical model cannot fully resolve the boundary layer, especially for shallow backwash flow depths, at the 4 mm $\times$ 2 mm grid

resolution. The under-prediction of $u_{x'}$ during backwash leads to less satisfactory agreement with an average $IA = 0.88$ and NRMSE = 24.7% for the sand case. Notably, previous depth-resolving numerical modeling approaches were not capable of accurately simulating permeable, sand beaches (Briganti et al., 2016).

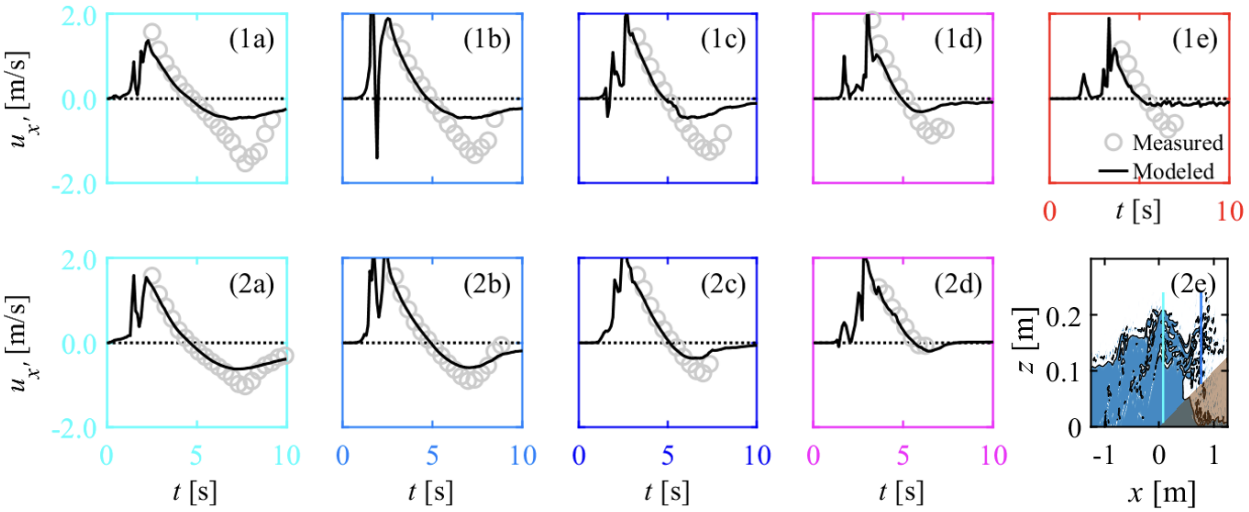

Figure 4.4: Time series of measured (open grey markers) and modeled (black solid curve) depth-averaged flow velocity ($u_{x'}$) for the (a) sand and (b) gravel cases at (1) PL 2 (cyan), (2) PL 3 (light blue), (3) PL 4 (dark blue), (4) PL 5 (pink), and (5) PL 6 (red) corresponding to the swash zone sensor locations shown in Fig 4.1. (b5) is a snapshot of the gravel case at t = 2.3 s with the $\phi^f = 0.5$ contour (black).

Modeled and measured shoreline position show good agreement (Fig. 4.5). The experimental shoreline position is defined at the location where the bed-normal flow depth is equal to 5 mm (Kikkert et al., 2013). However, the shoreline position is sensitive to the cutoff depth; a 1 mm difference in the cutoff value resulted in up to a ± 0.24 m (± 1.35 m) difference in the modeled shoreline position for the gravel (sand) case. Similarly, Kim et al. (2017) observed a ± 1 m difference in the shoreline position for dam-break driven swash on an impermeable, rough beach when changing the shoreline position cutoff by 1 mm. Using a threshold value of 5 mm to define the shoreline position (e.g., Kikkert et al.,

2013; Briganti et al., 2016), the maximum modeled shoreline position is over-predicted by 3.8% and under-predicted by 6.8% for the gravel and sand cases, respectively. In both cases, the maximum modeled shoreline position (i.e., runup) occurs 0.5 s later than the observed maximum runup and the shoreline position is over-predicted during the backwash phase; these differences may be related to the experimental gate motion that was not numerically modeled. Otherwise, the model reproduces the shoreline position well with $IA = 0.99$ (0.95) and NRMSE = 8.8% (15.8%) for the gravel (sand) case.

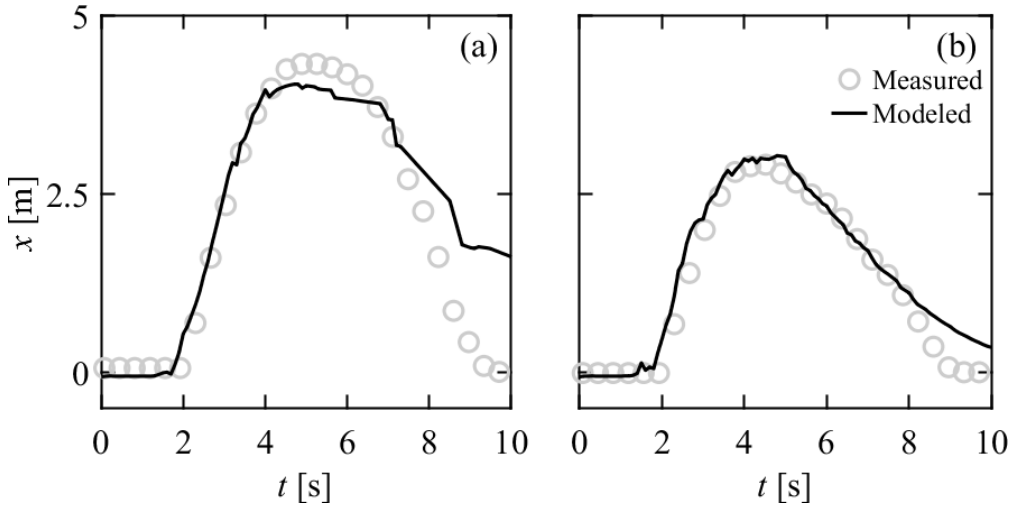

Figure 4.5: Time series of measured (open grey markers) and modeled (black solid curve) shoreline position for the (a) sand and (b) gravel cases.

Wetting fronts (Fig. 4.6) are compared to Figure 11 in Steenhauer et al. (2011) and demonstrate that the model behaves similarly to experimental observations. At t = 3.8 s, the gravel wetting front has significantly infiltrated and joined the groundwater for over half the distance traveled by the swash lens (Fig. 4.6b2). The groundwater table rapidly rises in response to the addition of water volume and has completely merged with the groundwater table by t = 6.4 s (Fig. 4.6d2). Conversely, the sand wetting front is very close to the beach surface for the majority of the swash lens at t = 3.8 s (Fig. 4.6b1). The ambient groundwater table is both forced away from and drawn towards the sand beach face. Near the end of the swash event, the wetting profile is still separated from the groundwater table in

the sand beach (Fig. 4.6d1). These results are in agreement with experimental observations (see Fig. 11 in Steenhauer et al., 2011). The most notable differences between the model and experiment are the the presence of seepage face in the backwash phase of the gravel experiment that is not observed in the numerical model and enhanced landward movement in the modeled groundwater.

Experimental and modeled wetting front differences may be partly attributed the wall effect; experimental measurements were recorded through a glass sidewall that may have altered wetting front measurements (Steenhauer et al., 2011). In the experiment, a weir located 0.5 m beyond the end of the beach (not modeled) controlled the groundwater level and may contribute to minor groundwater table differences near the landward edge of the domain. Additionally, the experimental wetting front between 0–50 mm could not be tracked for the sand case. Details such as encapsulated air bubbles and separation of infiltrating water observed in the numerical model are not captured by the experimental measurements.

The modeled cumulative infiltrated water volume (V_g; Fig. 4.7) is compared with Figure 13 in Steenhauer et al. (2011) and demonstrates good agreement with experimental measurements. In the experiment, V_g was calculated using two methods - one based on the change in water volume present on the beach surface and the other based on subsurface profiles and porosity. The modeled V_g was extracted directly as the amount of water present within the beach that exceeded the initial groundwater volume (i.e., at t = 0). Comparisons between the measured and modeled V_g demonstrate similar infiltration patterns. Gravel infiltration occurs more rapidly than in the sand beach and the infiltrated water volume is $\sim$3.2 times greater for the gravel case. The cumulative infiltrated water volume at t = 6 s is under-predicted by $\sim$5.9% and $\sim$19.0% as compared to the experimental results for the gravel and sand cases, respectively.

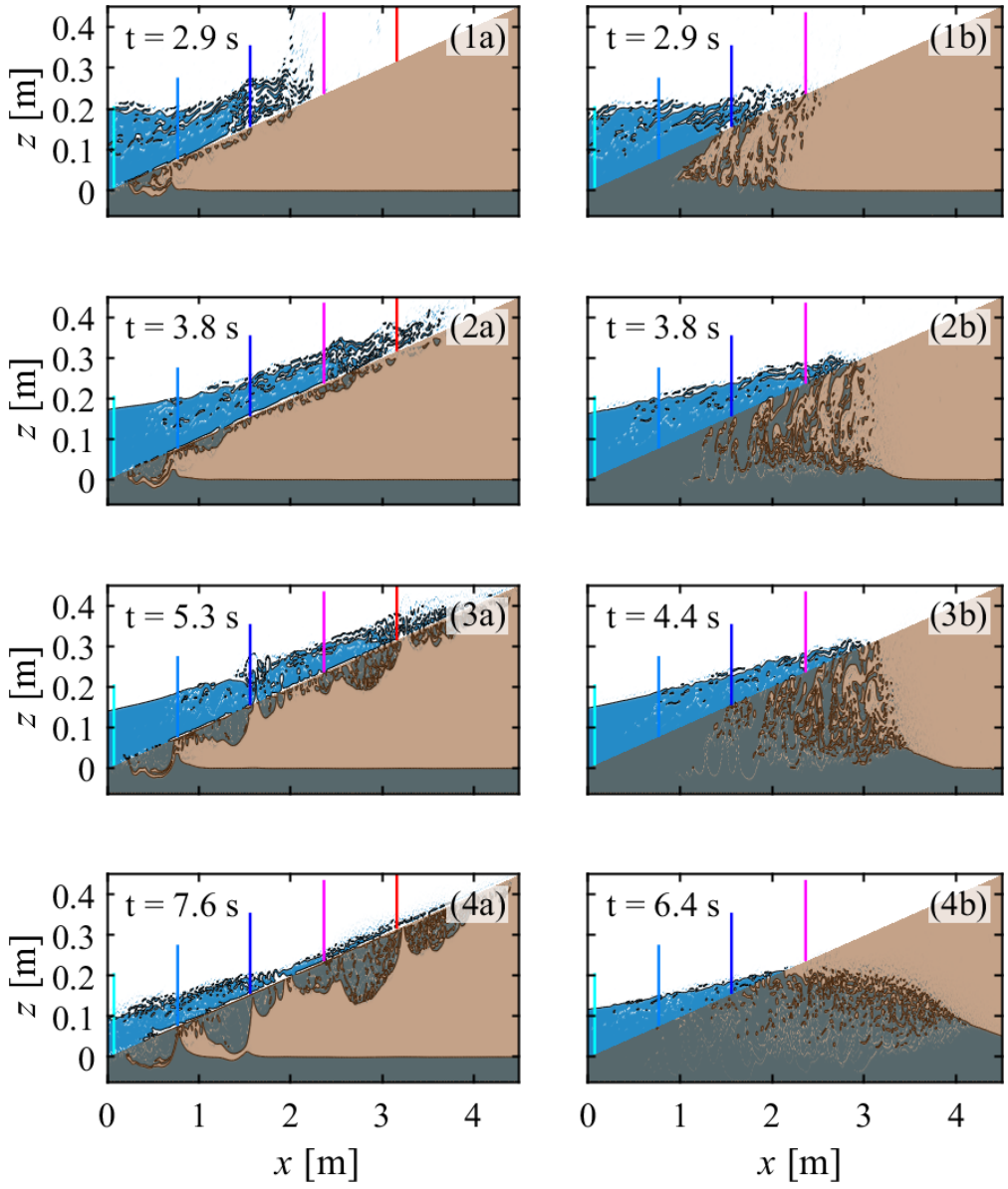

Figure 4.6: Snapshots of modeled water profiles with the $\phi^f = 0.5$ contour (black) at selected times (approximately equal to those shown in Fig. 11 in Steenhauer et al., 2011) for the (1) sand and (2) gravel cases. The colored vertical lines indicate correspond to the cross-shore deployment locations of PL 2 (cyan), PL 3 (light blue), PL 4 (dark blue), PL 5 (pink), and PL 6 (red).

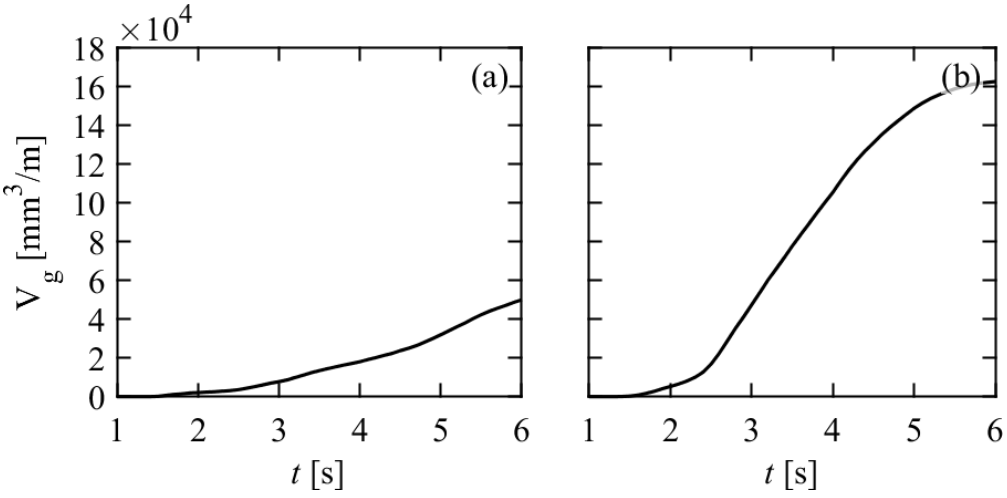

Figure 4.7: Time series of modeled cumulative infiltrated water volume (V_g) for the (a) sand and (b) gravel cases.

4.4 Discussion

4.4.1 Groundwater response to swash

The influence of swash zone surface flows on the beach groundwater table is highly dependent upon sediment characteristics (i.e., grain size, packing density, permeability, etc.). SedOlaFlow enables detailed investigation of swash surface and subsurface processes that can only be captured at a coarse scale (or not at all) by conventional experimental measurement techniques. Subsurface pressures, seepage processes, and the impact of grain size are explored by comparing two near-identical simulations; the only changes between the simulations are the grain size and calibrated drag coefficients (Table 4.1). As previously noted, both the gravel and sand cases are defined by the same ϕ_0^s (i.e., porosity). However, the gravel beach has a higher permeability as compared to the sand beach because of its larger sediment size.

In the gravel beach, the pressure head, ψ, at two selected vertical elevations (equal to (z = 0 m) and slightly below (z = -0.05 m) the initial groundwater level) increases

rapidly and then declines more slowly, with respect to the trend observed in h (Fig. 4.8a-b). Excluding PIV-LIF 5, the local infiltration rate (i.e., vertical velocity at the beach face) at a specific cross-shore location, q_x, is highest near-immediately after the uprush reaches the sensor location and rapidly decreases (Fig. 4.8c). The largest infiltration rate occurs at PIV-LIF 4. Exfiltration (i.e., $q_x < 0$) begins at approximately $t = 5$ s at all locations. The local volumetric water content, V_x, is the amount of water present within the vertical beach profile at $x \pm 0.002$ m that exceeds the initial groundwater volume; it includes the effects of infiltration/exfiltration and vertical/horizontal subsurface flow. Saturation is reached when the groundwater table extends to the beach face and is represented by a straight, horizontal V_x. For the two most seaward sensors, the groundwater table reaches the beach face near-instantaneously after bore arrival and the beach remains saturated (Fig. 4.6a2-d2, 4.8d1-d2). For the two most landward sensors, air bubbles are encapsulated as infiltrating swash meets the groundwater table, preventing complete saturation of the beach (Fig. 4.6c2-d2, 4.8d3-d4). A 3.1 s and 1.2 s lag between maximum h and maximum V_x is observed at PIV-LIF 4 (Fig. 4.8a3, d3) and PIV-LIF 5 (Fig. 4.8a4, d4), respectively. At $t = 10$ s, the groundwater level at the beach face exceeds the surface water level by $\sim$0.05 m (i.e., a seepage face exists) and the groundwater table is relatively flat at $z = 0.08$ m (not shown).

When compared to the gravel beach, the sand beach groundwater table response to swash infiltration is more localized; infiltrating swash only reaches the groundwater table for $x < \sim$0.9 m (Fig. 4.6d1). The maximum ψ at z = -0.05 m and q_x are larger for the sand beach as compared to the gravel beach at all PIV-LIF locations with the exception of PIV-LIF 4. The decreased permeability, increased drag, and larger water depth in the sand beach likely account for these differences. Large pressure fluctuations within the beach are observed that do not follow the trend of h (Fig. 4.9a-b). The maximum ψ at z = -0.05 m (i.e., slightly below the initial groundwater level) reaches 12.38 m and 44.49 m at PIV-LIF's 2 and 3, respectively (Fig. 4.9b1-b2). This large jump in ψ at $t = 1.9$ s at/between PIV-LIF's 2 and 3 displaces and creates sharp overheights in the groundwater

table (Fig. 4.6a1-d1), a phenomena also observed near PIV-LIF 4 after an increase in ψ at $t = 6.1$ s (Fig. 4.9b1-b3). Waddell (1973) similarly found that swash transmits pressure forces through the lower beach that induce high-frequency instantaneous groundwater-level response. This conclusion however, relied on pressure measurements characterizing the beach groundwater table, which may not be indicative of the actual groundwater table elevation. The present study confirms the importance of subsurface pressures on beach groundwater through direct examination of the groundwater table and subsurface pressures. This rapid change in pressure also coincides with a thin film of air becoming trapped between swash infiltration and the groundwater table. For the most seaward and landward sensors (i.e., PIV-LIF's 2 and 6), only infiltration occurs throughout the swash duration (Fig. 4.9c1, c5), whereas both infiltration and exfiltration occur in between these locations (Fig. 4.9c2-c4). Rapid changes in q_x, especially for PIV-LIF's 4 and 5 (Fig. 4.9c3-c4) indicate that infiltration (exfiltration) is not limited to occurring only at the rear (front) of the bore, contrasting with the findings of Packwood and Peregrine (1979). Rapid changes in q_x from positive to negative (and vice versa) are observed at PIV-LIF 5; these correspond to instances when $\psi < 0$ (Fig. 4.9b4-c4). The groundwater table reaches near-saturation for the two most landward sensors only (Fig. 4.9d1-d2) and the increase in V_x while exfiltration occurs for PIV-LIF's 4 and 5 suggests significant horizontal subsurface flow (Fig. 4.9d3-d4). The effects of swash on the groundwater table for $x > \sim$2 m are not realized in the short (10 s) simulation of the sand beach. Groundwater oscillations in the upper beach will significantly lag the swash event. This is in agreement with delayed water table responses observed by Hegge and Masselink (1991) and the dual-infiltration pathway proposed by Austin and Masselink (2006b) in which the groundwater response to swash is composed of both near-instantaneous and delayed components in the lower and upper beach, respectively. The delayed component is negligible in the gravel beach due to increased permeability and reduced drag when compared to the sand beach.

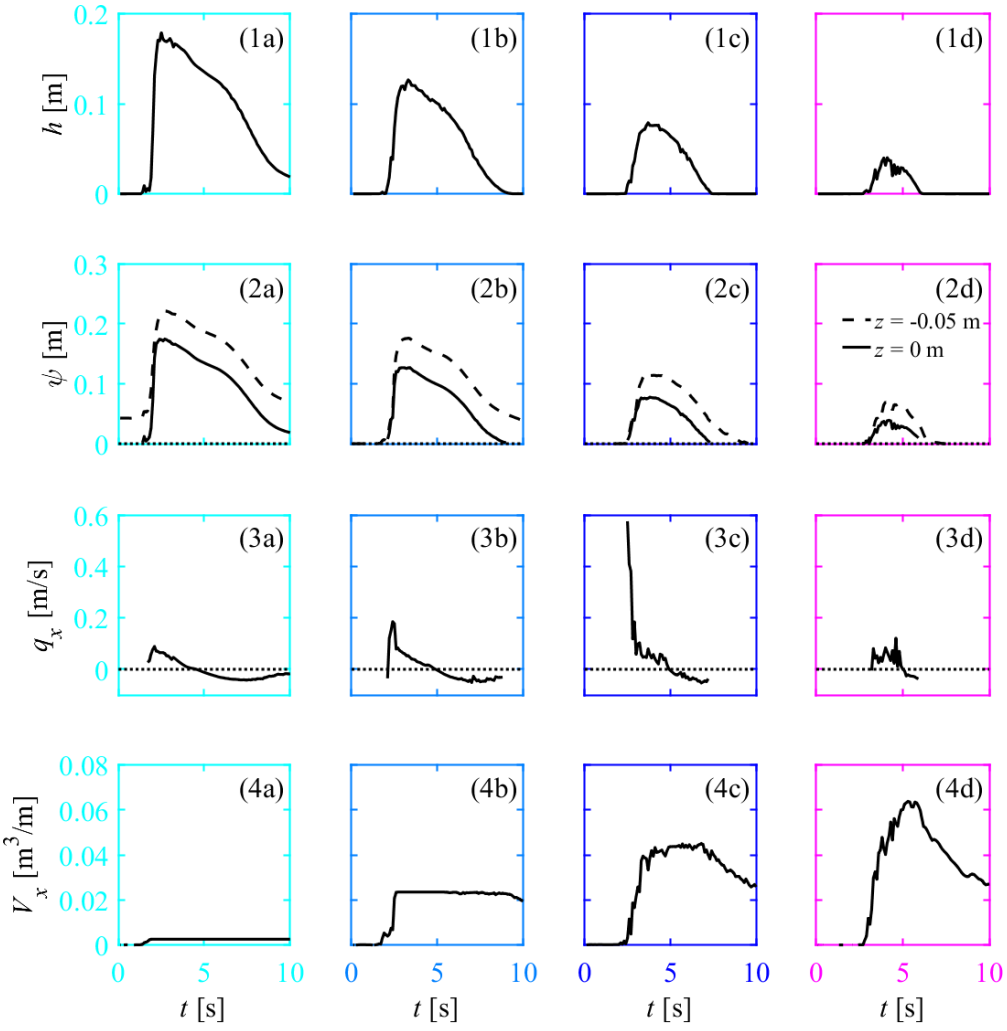

Figure 4.8: Time series of modeled (a) water depth (h), (b) pressure head (ψ) at z = -0.05 m (solid line) and $z = 0$ m (dashed line), (c) local infiltration rate (q_x), and (d) local volumetric groundwater (V_x) for the gravel case at (1) PL 2 (cyan), (2) PL 3 (light blue), (3) PL 4 (dark blue), and (4) PL 5 (pink) corresponding to the swash zone sensor locations shown in Fig 4.1. The vertical dash-dotted and dotted lines in (3) and (4) indicated the times of maximum h and V_x, respectively.

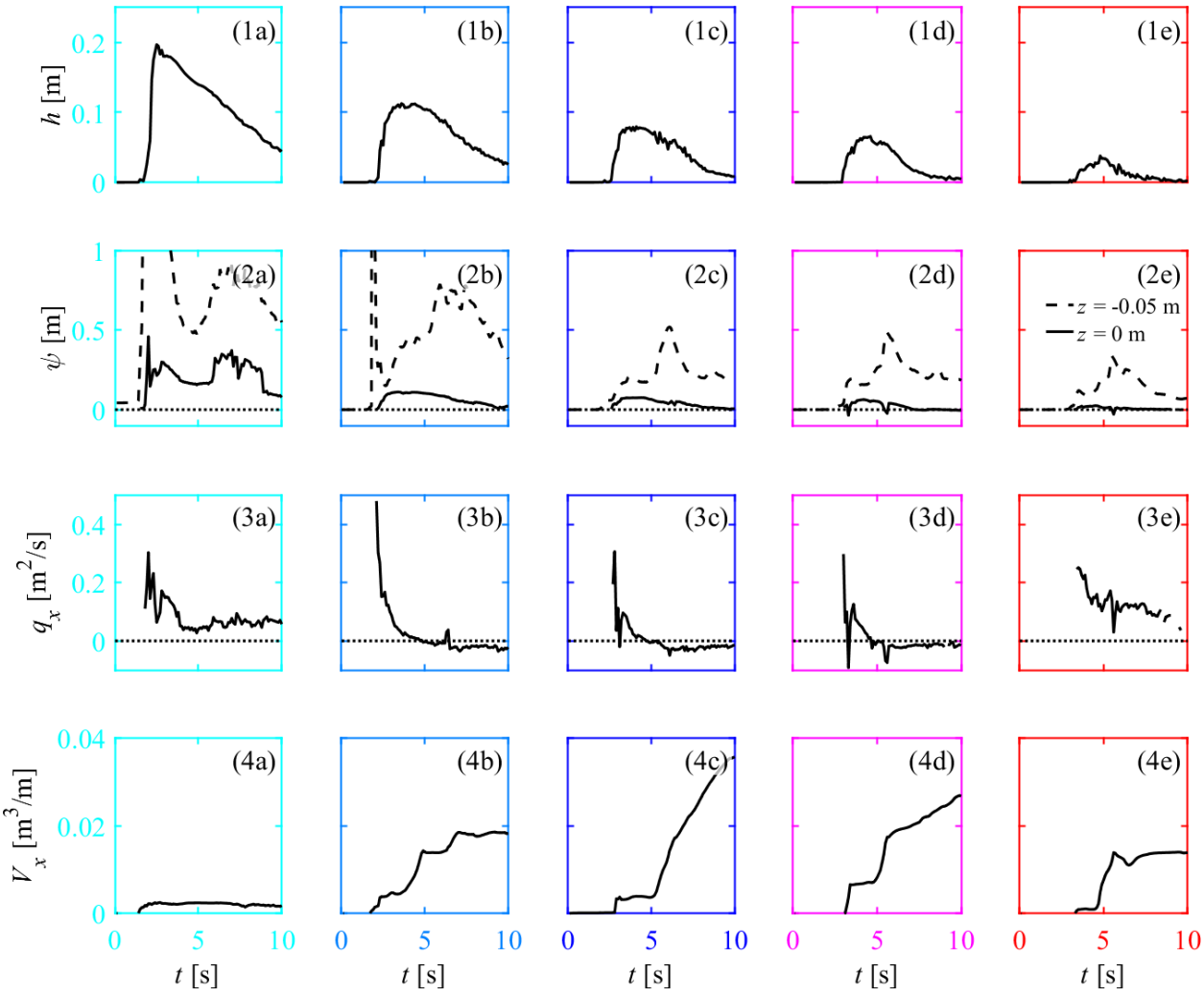

Figure 4.9: Time series of modeled (a) water depth (h), (b) pressure head (ψ) at z = -0.05 m (solid line) and $z = 0$ m (dashed line), (c) local infiltration rate (q_x), and (d) local volumetric groundwater (V_x) for the sand case at (1) PL 2 (cyan), (2) PL 3 (light blue), (3) PL 4 (dark blue), (4) PL 5 (pink), and (5) PL 6 (red) corresponding to the swash zone sensor locations shown in Fig 4.1.

4.4.2 Groundwater circulation

Swash-induced beach groundwater circulation is observed in the numerical model for the gravel and sand beaches. Longuet-Higgins (1983) developed an analytical solution for theoretical groundwater flow; however, it applies only to wave setup within a semi-infinite, fully-saturated domain and neglects water table, free surface, and land boundary effects. The solution describes infiltration in the swash zone following a curved offshore-directed path until exfiltrating at the lower beach face. Li and Barry (2000) found the analytical solution for groundwater circulation largely agreed with numerical modeling, however only phase-averaged, saturated groundwater flow was considered. The groundwater circulation observed in this study exhibits differences with the analytical groundwater circulation solution of Longuet-Higgins (1983), most significantly for the sand beach case.

In the gravel beach, infiltration quickly occupies the unsaturated zone, especially near the beach toe where horizontal infiltration exists and generates horizontal, onshore-directed groundwater movement (Fig. 4.10a). However, this horizontal infiltration is quickly reversed and an offshore-directed groundwater circulation cell exists by the late uprush phase on the lower edge of the beach (Fig. 4.10b). Onshore of this cell, subsurface flow is less organized, though largely directed onshore. The offshore-directed groundwater circulation cell grows through the remainder of the simulation and flow shifts from vertical infiltration to horizontal exfiltration during backwash in this cell (Fig. 4.10c-d). Flow in the upper beach becomes more organized and evolves into an onshore-directed circulation cell (Fig. 4.10d). By the end of the simulation, the circulation cell separates from the beach face and upper bed velocities become slope parallel, offshore-directed (Fig. 4.10e). The offshore-directed flow contributes to a net groundwater flux as a significant volume of groundwater has infiltrated into the beach.

Near-immediately after bore arrival, two non-uniform circulation cells are observed in the sand beach that are separated near the leading edge of the bore, coinciding with the

location of the largest subsurface velocities (Fig. 4.11a). Both cells show onshore-directed infiltration into the beach until the exfiltration point. The horizontal flow in the lower beach corresponds to a near-instantaneous groundwater flow pathway (i.e., P1 in Austin and Masselink (2006b)) described in Section 4.4.1. Immediately prior to maximum runup and flow reversal, two small circulation cells are visible within the upper beach circulation cell (Fig. 4.11b). The separation between the larger (i.e., lower and upper beach) circulation cells increases and moves onshore to a location approximately halfway between the initial shoreline position and maximum runup location. After flow reversal, the two smaller circulation cells begin to merge back together and the separation between the large circulation cells decreases (Fig. 4.11c). Between $t = 5.9$ s and 6.8 s, two offshore-directed circulation cells are formed at approximately 0.9 m $\leq x \leq$ 1.2 m and 2 m $\leq x \leq$ 2.6 m; both cells are located between onshore-directed circulation cells (Fig. 4.11d). However, these offshore-directed circulation cells are overtaken by onshore flow and by the end of the simulation nearly all flow below the infiltrating swash is directed onshore (Fig. 4.11e). In the upper beach (i.e., $x >\sim 2$ m), infiltrating swash flow within $\sim$0.1 m of the beach face is still vertical, corresponding to the unsaturated flow phenomenon described in Austin and Masselink (2006b). The rapid horizontal infiltration and delayed vertical infiltration into the vadose (i.e, variably saturated) zone occur simultaneously, thus increasing the complexity of groundwater circulation in the sand beach. The horizontal velocities between the infiltrating swash and groundwater table in the upper beach will contribute to the lag between the swash event and groundwater table response. The numerical model enables direct investigation of merging water masses in the upper beach that cannot be measured experimentally with pressure transducers. Unlike for the gravel case, there is negligible net groundwater flux in the sand beach due to limited infiltrated water volume.

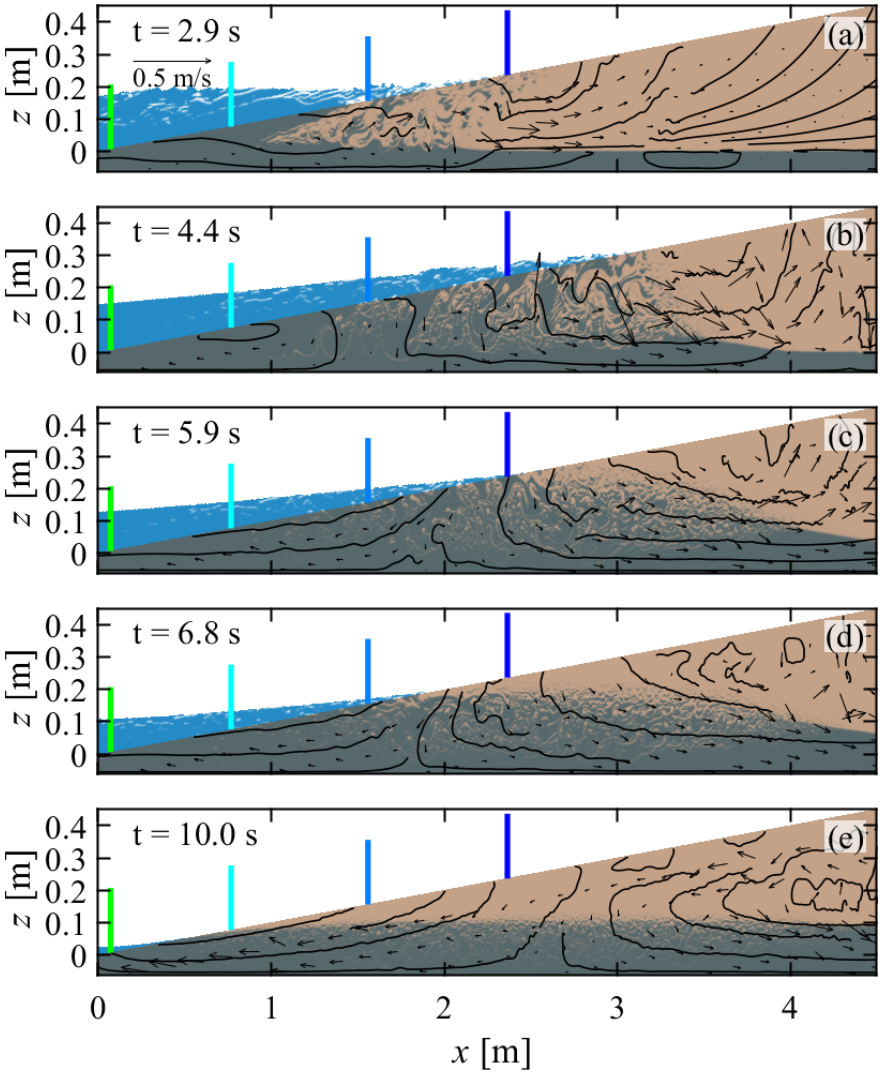

Figure 4.10: Snapshots of modeled water profiles at selected times for the gravel beach with fluid velocity vectors and streamlines shown as black arrows and curves, respectively. The colored vertical lines indicate correspond to the cross-shore deployment locations of PL 2 (cyan), PL 3 (light blue), and PL 4 (dark blue).

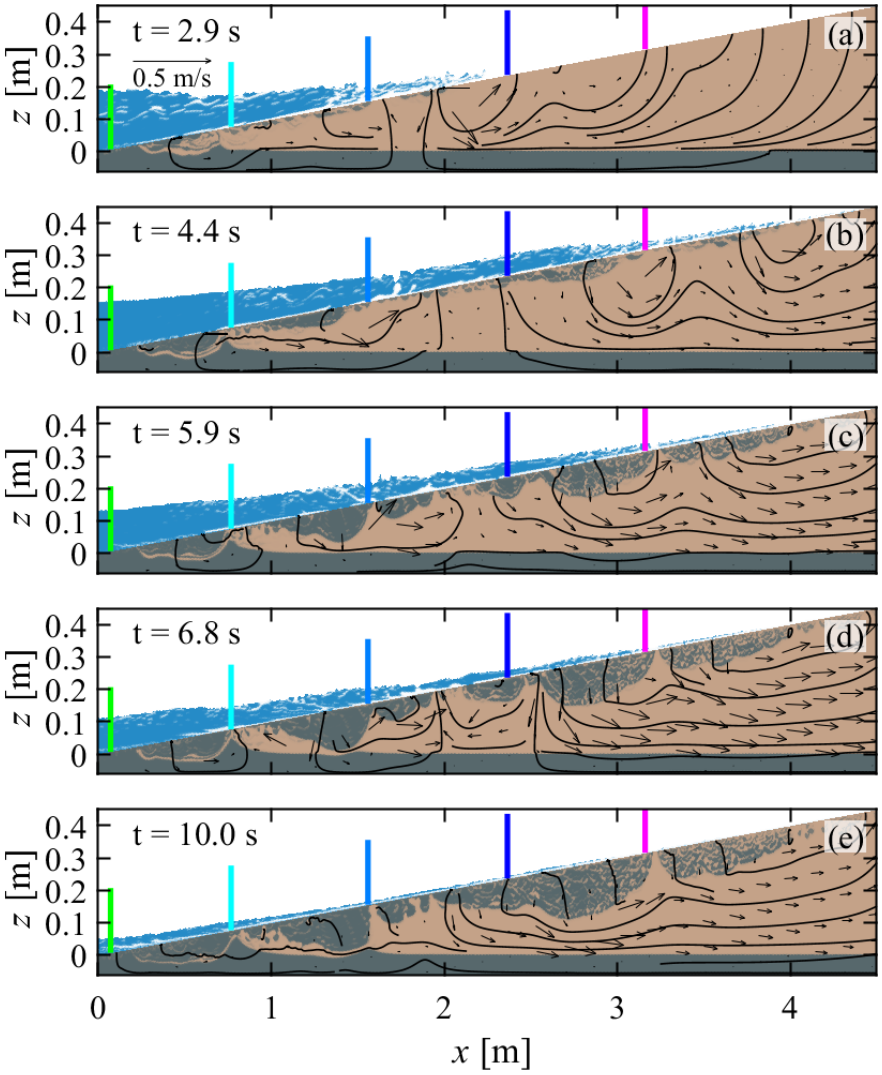

Figure 4.11: Snapshots of modeled water profiles at selected times for the sand beach with fluid velocity vectors and streamlines shown as black arrows and curves, respectively. The colored vertical lines indicate correspond to the cross-shore deployment locations of PL 2 (cyan), PL 3 (light blue), PL 4 (dark blue), and PL 5 (pink).

4.4.3 Swash response to groundwater

Surface swash flows impact the beach groundwater table, as demonstrated by previous studies (e.g., Austin and Masselink, 2006b; Bakhtyar et al., 2011) and expanded upon in this work. Pintado-Patiño et al. (2015) demonstrated that runup extent on an impermeable beach is significantly larger than on a permeable beach suggesting that beach subsurface infiltration capacity may play a role in surface swash flows. In a study of overtopping on gravel beaches, McCall et al. (2012) found that the inclusion of groundwater was critical to accurate numerical modeling of extreme wave runup. However, the impact of the beach groundwater table on swash flows has yet to be explicitly considered. Determining the influence and control of beach groundwater on surface swash flows is essential for accurate coastal vulnerability assessment and hazard planning.

Additional numerical simulations were performed to investigate the impacts of groundwater on swash. Ambient groundwater levels (i.e., initial water elevation within the beach) between $h_g = 0$ m and $h_g = 0.3$ m were modeled at 0.1 m increments. For each groundwater level, three beach slopes were tested corresponding to a steep (2:15), intermediate (1:10), and mild(er) (1:15) beach. Setup conditions, including the initial reservoir water depth (h_d = 0.6 m), water depth in front of the beach (h_0 = 0.062 m), and the distance between the water reservoir and intersection of the beach face with h_0, remained identical for all simulations. It should be noted that the domain was sufficiently extended for gravel beach cases (maximum $x = 11.32$ m) to eliminate groundwater reflection effects from the onshore, no-flux boundary. All simulations were performed with a bed-parallel numerical grid (Fig. 4.12). As with model validation, a threshold depth of 5 mm is used to define the shoreline position for each simulation. To compare results among sediment sizes and beach slopes, the vertical runup position, r_z (i.e., the vertical elevation of the shoreline position), is compared. The maximum r_z for the baseline (i.e., $h_g = h_0$) case for each sediment size and slope is used to normalize the data as $\Delta r_{z,i} = \max(r_{z,i}) - \max(r_{z,0})$, where i is initial groundwater level. Δr_z is effectively the change in vertical runup extent resulting from a change in the initial

groundwater level.

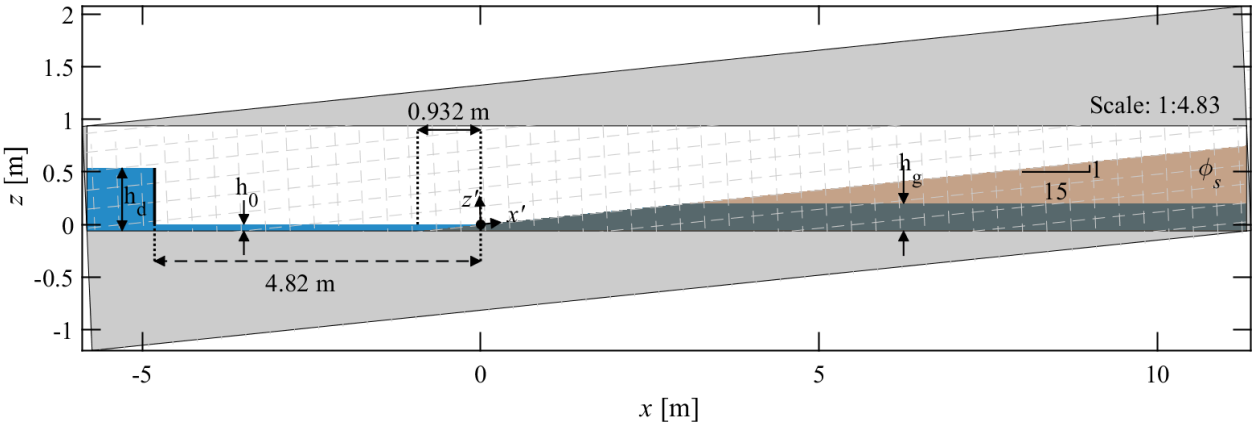

Figure 4.12: Example numerical setup for the mild (1:15) gravel beach with an initial groundwater level of $h_g = 0.2$ m. The origin of both coordinate systems is at the intersection of the initial water surface and beach face (black circle), 0.932 m and 4.82 m from the beach toe and gate, respectively. $h_d = 0.6$ m is initial water depth in the reservoir and $h_0 = 0.062$ m is the initial water depth in front of the beach. The beach volumetric sediment concentration is ϕ_s. The light grey regions are not included in the numerical domain.

Model results show that antecedent groundwater levels significantly change the vertical swash extent (up to 25%) for both the gravel and sand beaches (Fig. 4.13). The dashed colored lines in Figure 4.13 indicate the best fit of the data for the corresponding beach slope, calculated using the least-squares method constrained by $\Delta r_z = 0$ m for $h_g = 0$ m. Generally, a linearly increasing relationship between h_g and Δr_z is observed. Minor discrepancies may be due to the finite model domain size and initially flat groundwater table. In natural beaches, a groundwater overheight (i.e., when the elevation of the groundwater table is higher than the free (ocean) surface) is typically convex and the hydraulic gradient leads to divergent onshore/offshore groundwater flow Heiss et al. (2014). In the numerical domain, the groundwater table is initialized as a horizontal line for direct comparison and no onshore-directed groundwater flow can occur across the onshore boundary, likely leading to increased exfiltration at the beach face. This model-induced exfiltration hinders onshore-directed flow

near the beach face and increases in magnitude with rising groundwater levels. This may also explain why Δr_z is negative for $h_g = 0.3$ m for the mild, sand beach case.

Raising the groundwater levels in the gravel beach results in approximately a 25%, 20%, and 23% increase in the vertical swash extent for the mild, intermediate, and steep beach, respectively (Fig. 4.13a). For the sand beach, the vertical swash extent is increased by approximately 0%, 4%, and 6% for the mild, intermediate, and steep beach, respectively (Fig. 4.13b).

The magnitude of Δr_z is significantly larger for the gravel beach as compared to the sand beach, highlighting that the relationship between swash and groundwater is highly sensitive to sediment properties (e.g., permeability). Results from the gravel and sand beaches suggest that elevated groundwater levels reduce infiltration into the beach, limiting momentum and mass loss due to vertical swash infiltration and driving swash further onshore. The change in infiltration capacity due to higher groundwater levels is larger for the gravel beach and thus the impacts are more significant as compared to the sand beach. It is also possible that the seepage face caused by a groundwater overheight serves to reduce drag along the beach face and propel swash onshore.

In addition to swash extent, a key factor in coastal flooding is the duration (t_e) for which the water level exceeds a certain threshold (Fig. 4.14). Coastal flood duration is critical for infrastructure risk (Pezza and White, 2021), emergency response services (Yin et al., 2017), and habitat survival (Hoggart et al., 2014). Here, t_e is defined as the duration for which $r_{z,i} > \max(r_{z,0})$. The dashed colored lines in Figure 4.14 indicate the best fit of the data for the corresponding beach slope, calculated using the least-squares method constrained by $t_e = 0$ s for $h_g = 0$ m. Generally, t_e linearly increases with h_g, with small discrepancies likely related to the finite model domain size and initially flat groundwater table. A 0.1 m increase in h_g results in approximately a 2 s, 0.9 s, and 0.8 s increase in t_e for the mild, intermediate, and steep gravel beaches, respectively. For the sand case, t_e increases by approximately 0.04 s, 0.6 s, and 0.1 s per 0.1 m increase in h_g for the mild, intermediate, and steep beaches,

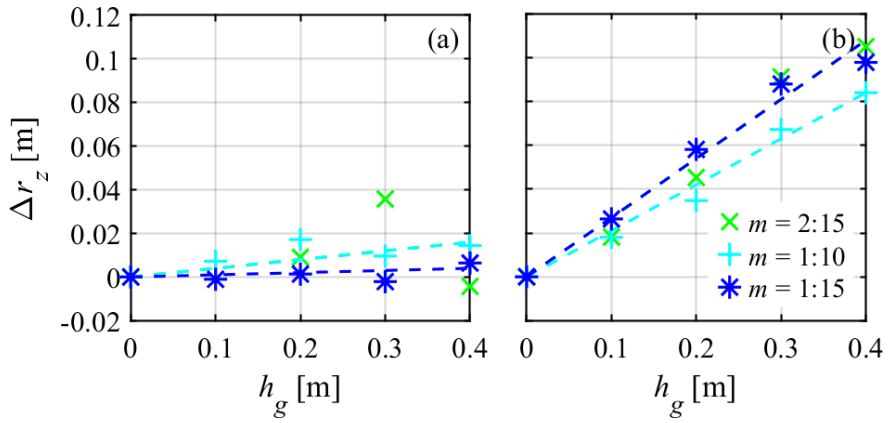

Figure 4.13: Change in maximum runup elevation (Δr_z) as a function of the initial groundwater level (h_g) for the (a) sand and (b) gravel cases. The steep (2:15), intermediate (1:10), and mild(er) (1:15) beaches are differentiated as the green $\times$, cyan $+$, and blue * markers, respectively, where the corresponding dashed colored lines are the line of best fit.

respectively. Both Δr_z and t_e are inversely proportional to the gravel beach slope; this behavior is not observed in the sand beaches. The beach slope appears to have minimal impact on t_e for the sand beach; however, swash backwash flows are reduced for the $h_g > 0$ cases (i.e., swash remains elevated for a longer amount of time, not shown). The impact of ambient groundwater on swash magnitudes is most significant for the mild (steep) beach, however the mild (intermediate) beach experiences the longest duration of swash exceeding the baseline r_z for the gravel (sand) case.

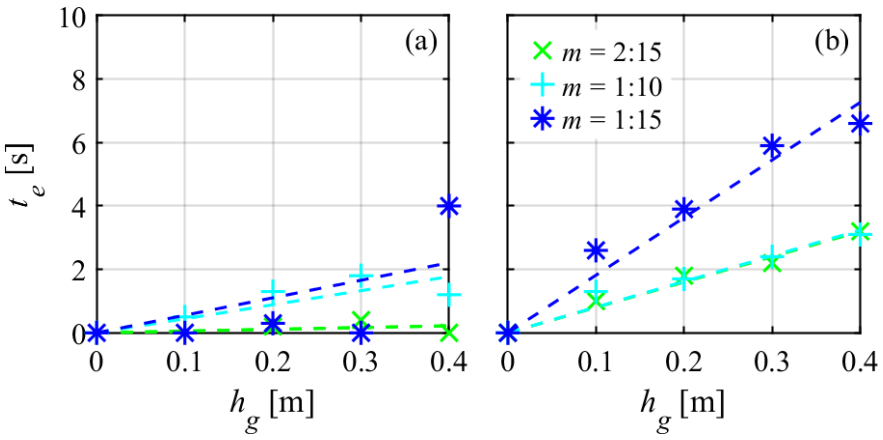

Figure 4.14: Total time for which the vertical runup position ($r_{z,i}$) exceeds the baseline (i.e., $h_g = h_0$) maximum runup position $r_{z,0}$ as a function of the initial groundwater level (h_g) for the (a) sand and (b) gravel cases. The steep (2:15), intermediate (1:10), and mild(er) (1:15) beaches are differentiated as the green $\times$, cyan $+$, and blue * markers, respectively, where the corresponding dashed colored lines are the line of best fit.

4.5 Conclusions

A new two-phase Eulerian model, SedOlaFlow, was developed and utilized to numerically investigate swash–groundwater dynamics. SedOlaFlow was validated with flow depth, flow velocity, and shoreline position measurements, and qualitatively compared to subsurface measurements and yielded good agreement with measured data (Steenhauer et al., 2011; Kikkert et al., 2013).

In addition to model validation, detailed swash zone seepage processes were examined through numerical modeling. Investigation of the groundwater response to swash highlights that the groundwater table is highly dynamic and reactive to bore-driven swash zone flows. Large differences in the infiltration behavior between the gravel and sand beaches impact the extent and timing of groundwater oscillations. Unsteady, non-uniformly distributed infiltration is the dominant process in both the gravel and sand beaches. In contrast with previous observations (e.g., Li and Barry, 2000), exfiltration can occur even when the swash

depth is non-zero. The reduced permeability of the sand beach leads to increased impacts of subsurface pressure fluxes on the groundwater table. Numerical modeling enables direct examination of the delayed component of swash-induced groundwater flow (i.e., vertical infiltration through the unsaturated subsurface).

Flow through the variably-saturated vadose zone differs significantly from analytical solutions of saturated groundwater flow. Complex flow patterns create multiple groundwater circulation cells that rapidly evolve in time. Groundwater circulation patterns in the gravel and sand beach are dissimilar, suggesting that the vadose zone and beach permeability play a key role in subsurface flow behavior.

Ambient groundwater levels impact swash extent and duration; higher antecedent groundwater levels propagate swash flows further onshore and increase the runup period. Swash extent is increased by 20-25% (0-6%) for the gravel (sand) beach under elevated groundwater conditions. This suggests that impact of the beach groundwater table on swash increases with beach permeability. These findings confirm a bi-directional relationship between surface and subsurface flows in the swash zone and have direct impacts on coastal flooding and vulnerability assessment, especially for coarse sediment beaches.

The analysis presented in this work was based on two sediment sizes and a single dam-break driven swash event. The investigation of groundwater effects on swash flows was limited to three slopes with idealized horizontal groundwater levels. A comprehensive understanding of the bi-directional relationship between surface and subsurface flows in a real beach requires further investigation, not limited to the effects of grain size and heterogeneity, groundwater table shape, wave events, and beach mobility.

4.6 Acknowledgements

This study was partially supported by the Streisand Foundation, California Department of Parks and Recreation Division of Boating and Waterways (C1670006), and the Basic Science

Research Program through the National Research Foundation of Korea (NRF) funded by the Ministry of Education (NRF-2021R1F1A1062223). Numerical simulations presented in this study were carried out using the Hoffman2 cluster at the University of California, Los Angeles. The SedOlaFlow source code and case setup to reproduce the same results are publicly available on Zenodo: `https://doi.org/10.5281/zenodo.7946411` (source code) and `https://doi.org/10.5281/zenodo.7946415` (case setup). The authors gratefully acknowledge Tom O'Donoghue for providing the experimental data used for model validation.

Chapter 4 is currently in revision as "A numerical study of dam-break driven swash and beach groundwater interactions" by the authors: Marie-Pierre C. Delisle, Yeulwoo Kim, and Timu W. Gallien, in the Journal of Geophysical Research: Oceans, Copyright American Geophysical Union.

CHAPTER 5

Beach groundwater impacts on wave runup: mechanisms and implications

5.1 Background

Sea level rise will substantially amplify coastal risk and flood extent (e.g., Church et al., 2013; Rotzoll and Fletcher, 2013; Prime et al., 2015; Vitousek et al., 2017; Befus et al., 2020; Taherkhani et al., 2020). By the end of the 21st century, extreme once-in-a-century sea levels of the recent past are projected to occur 160 – 530 times more frequently (i.e., 1.6 – 5.3 times a year; Fox-Kemper et al., 2021). Coastal migration is increasing (e.g., Nicholls, 2004; McGranahan et al., 2007; Hugo, 2011) and over one billion people are projected to live in coastal communities by 2050 (Merkens et al., 2016). Improved understanding of processes contributing to coastal flood risk is urgently needed to protect vulnerable coastal communities (Horn, 2002; Elko et al., 2015; Gallien, 2016; Elko et al., 2019; Housego et al., 2021).

The swash zone is defined as the cross-shore region of the beach that is intermittently covered and exposed by wave runup and rundown. This is a highly dynamic region characterized by extreme sensitivity to SLR (Arns et al., 2017; Almar et al., 2021). Flow exchange between swash and subsurface flows through infiltration/exfiltration processes is an important swash zone feature that depends on a variety of factors, including beach porosity (e.g., Packwood, 1983), tidal stage (e.g., Heiss et al., 2014), and depth to the groundwater table (e.g., Bakhtyar et al., 2011). The beach groundwater table responds to both low-frequency (e.g., tide, storm

surge) and high-frequency (e.g., individual swash events) fluctuations and may be higher than the tidal elevation (e.g., Turner et al., 1997b; Steenhauer et al., 2011; Sous et al., 2013; Heiss et al., 2015). Groundwater levels will rise at approximately the same rate as SLR, increasing groundwater-driven coastal flooding (Horn, 2006; Bjerklie et al., 2012; Rotzoll and Fletcher, 2013; Hoover et al., 2017; Housego et al., 2021). Although swash impacts on beach groundwater have received sustained attention in the literature (e.g., Longuet-Higgins, 1983; Hegge and Masselink, 1991; Li and Barry, 2000; Horn and Li, 2006; Bakhtyar et al., 2011), beach groundwater impacts on swash and coastal vulnerability have received little attention (e.g., Morris et al., 2007; Rotzoll and Fletcher, 2013; Abboud et al., 2018; Delisle et al., in revision). Notably, the inclusion of groundwater processes substantially increases SLR-induced coastal flooding predictions (Rotzoll and Fletcher, 2013; Befus et al., 2020).

Quantifying the underlying physical processes occurring within the dynamic swash zone is extremely difficult (Chardón-Maldonado et al., 2016). An inverse relationship between beach permeability and wave runup has been observed (e.g., Villarroel-Lamb et al., 2014; Poate et al., 2016) and incorporating sediment size into empirical parameterizations improves runup (setup) predictions (Dalinghaus et al., 2022). Recently, Delisle et al. (in revision) demonstrated a bi-directional feedback between a solitary wave and beach groundwater flows where elevated antecedent groundwater levels increase runup extent and duration. However, runup interactions between successive waves are not well understood (Wu et al., 2021). Raubenheimer et al. (2004) suggested that wave runup is influenced by near-bed turbulence and friction, however the role of boundary layer processes on runup evolution remains unclear (Delisle et al., in revision).

Swash zone flows are multi-phase, transient, and interdependent, posing significant challenges to observational measurements and modeling strategies (Chardón-Maldonado et al., 2016). A significant body of research suggests that near-bed dynamics such as infiltration and turbulence impact runup (Horn, 2006; Briganti et al., 2016). Infiltration (exfiltration) in the swash zone causes vertical fluid drag that alters the effective weight of surface sediment

and stabilizes (destabilizes) the bed (e.g., Martin and Aral, 1971; Nielsen, 1992; Baldock and Holmes, 1999; Nielsen et al., 2001). Moreover, swash infiltration increases turbulence (e.g., Kikkert et al., 2013; Pintado-Patiño et al., 2015). Bore-generated turbulent motions reach the beach face in the swash zone and turbulent dissipation rates increase as water depth decreases (Puleo et al., 2000; Raubenheimer et al., 2004). Turbulence generated at bore-collapse dominates during swash uprush whereas bottom-generated turbulence is dominant during rundown (Puleo et al., 2000; Petti and Longo, 2001; Cowen et al., 2003). Turbulence is critical to accurately characterize surface water depths (Briganti et al., 2016) and bed shear stress (Turner and Masselink, 1998; Butt et al., 2001; Horn and Li, 2006; Kikkert et al., 2013). Collectively, these findings suggest that seepage processes and boundary layer mechanisms are interconnected, however, their impact on swash extent remains unresolved (Chardón-Maldonado et al., 2016). Understanding the physical processes controlling swash zone surface and subsurface flow interactions is fundamental to accurate wave runup predictions and assessment of coastal flooding risk.

Few numerical models exist that can resolve both surface and subsurface flows within the swash zone. Models that weakly or partially-couple surface and subsurface flows (e.g., Li et al., 1997, 2002; Bakhtyar et al., 2011; Desombre et al., 2012; Perera et al., 2019) cannot capture the bi-directional relationship between swash and beach groundwater and often exclude important processes (e.g., variably-saturated subsurface flow). COBRAS (Cornell Breaking Waves and Structures; Lin and Liu, 1998a,b), a RANS model with k-ε turbulence closure, has been validated for a variety of swash zone applications (e.g., Lin et al., 1999; Liu et al., 1999; Hsu et al., 2002; Amoudry et al., 2008; Zhang and Liu, 2008; Pintado-Patiño et al., 2015). Hsu et al. (2002) extended COBRAS to include both surface and subsurface flows, however, groundwater flow processes are simplified and neither air nor sediment phases are explicitly modeled. SedOlaFlow, a two-phase model that simultaneously resolves high-frequency surface fluctuations, accounts for porous media flow, and includes bi-directional surface-subsurface processes was recently developed by Delisle et al. (in revision). The model

was validated with surface flow and velocity measurements and yielded good agreement with qualitative subsurface data comparisons.

Motivated by the need to understand swash–groundwater feedback mechanisms on runup and subsequent coastal vulnerability, wave runup is investigated using the OpenFOAM based numerical model SedOlaFlow (Delisle et al., in revision). The model is used to investigate physical processes controlling swash behavior, particularly in relation to beach groundwater and seepage face impacts. SedOlaFlow was previously validated for dam-break driven swash on a sloping permeable beaches composed of sand or gravel (Delisle et al., in revision) and is applied to periodic waves in this study. The numerical model and model setup are described in Section 5.2. Section 5.3 presents the swash response to various wave conditions and antecedent groundwater levels. Discussion of the near-bed mechanisms responsible for the swash–groundwater relationship, application of results to natural beaches, and the implications of swash–groundwater dynamics on coastal vulnerability are included in Section 5.4. Section 5.5 summarizes the main conclusions of this study.

5.2 Methods

5.2.1 Numerical model

In this study, the Reynolds-averaged Eulerian two-phase numerical model, SedOlaFlow (Delisle et al., in revision), is used to investigate the relationship between swash and beach groundwater. SedOlaFlow was validated for extreme swash flow conditions (i.e., dam-break driven swash; Delisle et al., in revision) and further validation is not conducted in this work. A description of the numerical model can be found in Section 2.2 with more detailed description in (Delisle et al., in revision).

5.2.2 Model setup

A two-dimensional (2DV) model domain is created that is an elongated version of the model setup described in Delisle et al. (in revision). The domain is extended to provide sufficient space for wave generation and eliminate groundwater reflection effects from the onshore, no-flux boundary (Fig. 5.1). Based on sensitivity testing performed in Delisle et al. (in revision), a bed-parallel, uniform $dx = 8$ mm $\times$ $dz = 4$ mm computational grid is selected. The modeled bed-parallel (x') and bed-normal (z') axes are defined as positive onshore and upward, respectively, as are the gravity-normal (x) and gravity-parallel (z) axes used for analysis. The origin of both coordinate systems is at the beach toe. The mesh is initially constructed with a 18.1 m (width) $\times$ 3.8 m (height) grid and regions outside of the numerical flume (light grey regions in Fig. 5.1a) are then removed using the OpenFOAM tool snappyHexMesh (Jackson, 2012) to create the final mesh with flume dimensions of 18 m (width) $\times$ 2 m (height) (1.1 million grid cells).

The numerical flume is composed of a 6 m flat, horizontal section adjacent to a fixed 1:10 beach profile. The initial water depth in front of the beach is $h_0 = 0.6$ m. The initially flat water depth within the beach (i.e., groundwater level) varies between 0.6–0.8 m depending on the trial where h_g indicates the elevation of the groundwater level above h_0. The grain size $d = 8.4$ mm (gravel) or $d = 1.3$ mm (sand) and specific gravity $s = 2.65$ are specified in the model. The vertical profile of volumetric sediment concentration, ϕ_s, is prescribed as:

$$\phi^s = \frac{\phi_0^s}{2}\{1 + \tanh[2400(z_b - z)]\} \tag{5.1}$$

where $\phi_0^s = 0.7$ (i.e., effective porosity of $\eta \approx 0.3$) is the maximum sediment concentration and z_b is the beach interface. The Darcy-Forchheimer drag coefficients are specified as $\alpha =$ 1 (400) and $\beta = 0.05$ (20) for the gravel (sand) beach (Delisle et al., in revision).

Application of model results to nature requires careful consideration of how physical processes are represented. The scale parameter, n, represents the ratio of nature (prototype) to model values and is defined as: $n = p_p/p_m$, where p_p and p_m are the prototype and model

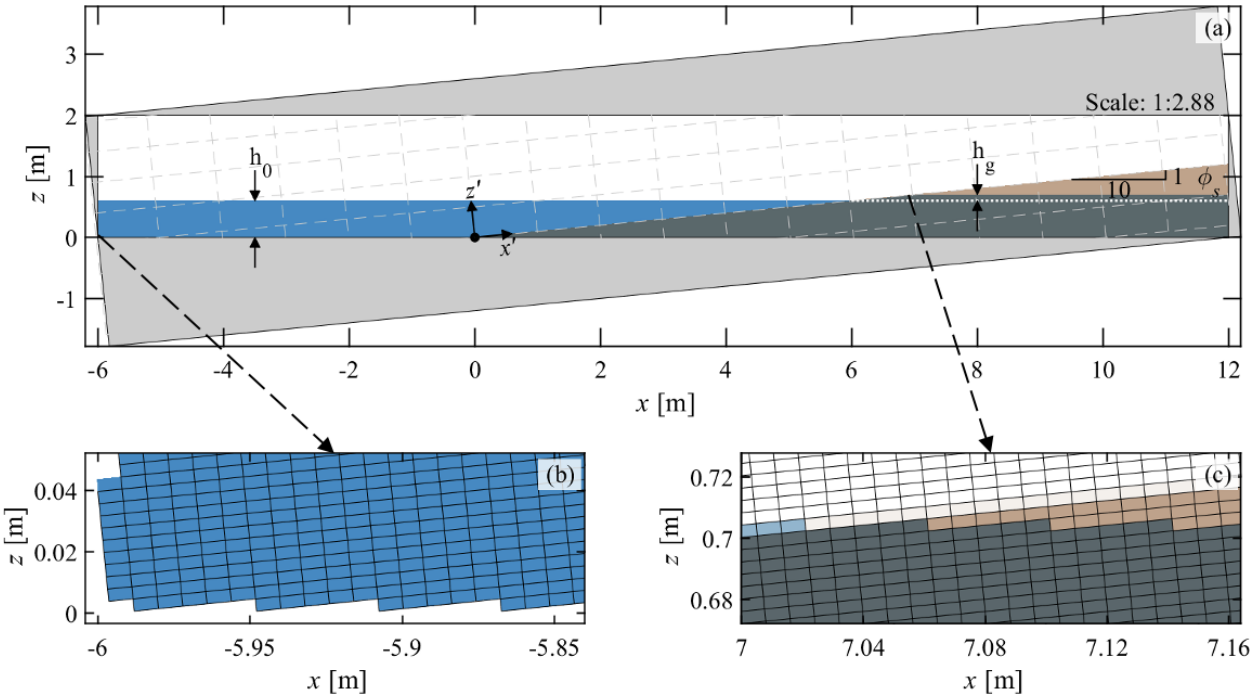

Figure 5.1: (a) Numerical setup and initial conditions (for $h_g = 0.1$ m trial). Air, surface water, groundwater, and sediment (ϕ_s) phases are white, blue, dark grey, and tan colors, respectively. The surrounding light grey regions are not included in the numerical domain as shown by (b) the enlarged view of the lower left corner of the domain. The modeled x'-z' coordinate system is bed-parallel as shown by (c) the enlarged view of the intersection of the groundwater level and beach face.

parameter values, respectively. To accurately represent nature, dimensionless parameters (e.g., Froude, Reynolds, Weber, Irribaren, Shields numbers, etc.) that describe physical processes should match (or fall within a certain range). In this work, Froude scaling is applied and representative in-situ conditions are adjusted for the flume dimensions as (e.g., Kamphuis, 1972; Noda, 1972):

$$n_T = \sqrt{n_L} = \sqrt{n_H} = \sqrt{n_D} \tag{5.2}$$

where T = wave period, L = wave length, H = wave height, and D = water depth. The chosen depth scale ($n_D = 5$) was used to define the model parameter values (Table 5.1).

Equation (5.2) ensures the accurate depiction of wave dynamics (e.g., Noda, 1972) and also satisfies the conditions for wave runup similitude (Van Rijn et al., 2011). Given that model simulations are performed for immobile beaches, sediment mobility scaling is not required.

Table 5.1: Summary of modeled cases with scaled wave conditions using Froude scaling (Eq. 5.2). T is the wave period, H is the wave height, d is the modeled grain size, and the subscript "p" represents the prototype (nature) value. Each case is simulated with a water depth of $D = 0.6$ m ($D_p = 3$ m) and $h_g = 0$, 0.1, and 0.2 m (36 total simulations).

Wave Type	H (m)	H_p (m)	T (s)	T_p (s)	d (mm)	Case ID
Monochromatic	0.1	0.5	3.1305	7	8.4	MT3G
					1.3	MT3S
			7.1554	16	8.4	MT7G
					1.3	MT7S
Irregular	0.25	1.25	3.1305	7	8.4	IT3G
					1.3	IT3S
			7.1554	16	8.4	IT7G
					1.3	IT7S

A wall boundary is imposed along the bottom of the computational domain; no-flux boundary conditions are applied for scalar and bottom-normal velocity components and a no-slip condition is applied for bottom-parallel velocities. In the beach region, the no-slip boundary condition is of minor importance as it exists below an immobile sediment bed. The top boundary is specified with an atmospheric boundary condition, the inlet/outlet (y-z) planes are specified as no-flux boundaries for scalar and velocity components, and the lateral (x-z) planes are specified as empty boundaries in OpenFOAM. An initial model timestep of 10^{-6} s is used and then dynamically adjusted by the Courant-Friedrichs-Lewy condition with a Courant number of 0.2. The numerical model required a wall-clock time of $\sim$90 hours using 12 processors (2.3 GHz Intel Xeon Gold 6140) for 80 s of simulation.

5.3 Results

5.3.1 Incident wave conditions

This study investigates the relationship between antecedent groundwater levels and runup extent for monochromatic and irregular wave series with various wave periods, wave heights, and grain sizes (Table 5.1). Simulations with the same wave type, wave height, wave period, and grain size are referred to as a *case* hereafter. For each modeled case, initial groundwater levels of h_g = 0, 0.1, and 0.2 m (hereafter referred to as *groundwater* (or h_g) *trials*) are simulated separately for a total of 36 simulations. Regular, monochromatic waves were generated at the offshore boundary based on cnoidal wave theory for intermediate (T = 3.1305 s) and shallow water wave conditions (T = 7.1554 s). Irregular waves were generated by implementing a JONSWAP spectrum with a peak enhancement factor of 3.3. Significant wave heights of H_s = 0.1325 and 0.0922 m were chosen for peak wave periods of T_p = 3.1305 s and 7.1544 s, respectively. Following Rayleigh probability distribution, these selected conditions correspond to H = 0.25 m at the initial water depth of h_0 = 0.6 m. Comparison of the idealized and modeled energy densities (E) at the beach toe (x = 0 m) demonstrate modeled spectra with substantial noise (Fig. 5.2). This is likely the result of a relatively short model duration (t = 120 s) that was feasible with available computational resources, especially as the deviation from the idealized spectrum is larger for the I7G and I7S cases (∼20 waves; Fig. 5.2b) as compared to I3G and I3S case (∼40 waves; Fig. 5.2a). However, the spectra demonstrate that a reasonable range of wave conditions are captured to assess the influence of wave irregularity on swash–groundwater dynamics while remaining computationally feasible.

The temporal evolution of free surface elevation at the beach toe (x = 0 m) demonstrates that near-identical wave conditions are simulated for both gravel and sand beach cases (Fig. 5.3). Monochromatic (irregular) wave cases were simulated for t = 80 s (120 s). Small discrepancies in the surface elevation exist at the start of the simulation for gravel trials

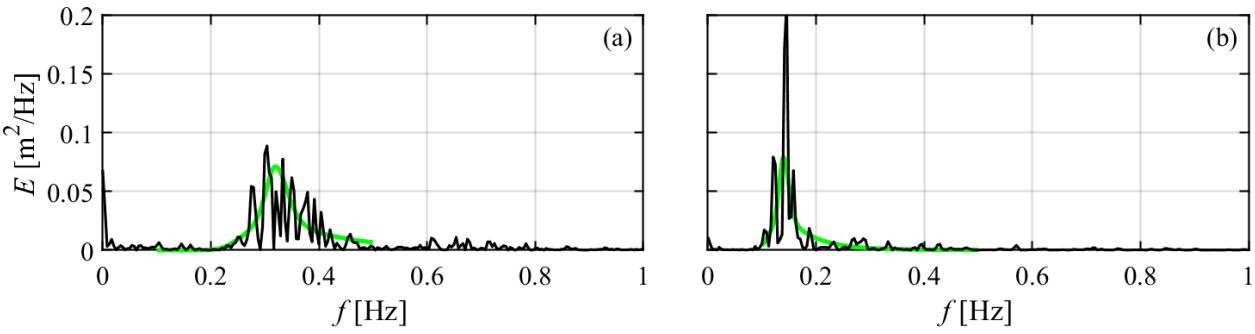

Figure 5.2: Comparison of idealized (green) and modeled (black) energy density (E) spectra for the irregular wave simulations at the beach toe ($x = 0$ m) with peak wave periods of (a) $T_p = 3.1305$ s and (b) $T_p = 7.1554$ s.

with $h_g > 0$ m (i.e., 5 s $< t <$ 12 s, solid red and black lines). In the ∼7 s (∼10.5 s) between the start of the simulation and the arrival of the first wave at the beach face for the $T =$ 3.1305 s ($T = 7.1554$ s) cases, groundwater rapidly exfiltrates from the gravel beach trials with $h_g > 0$ m, resulting in slightly higher free surface elevations at the beach toe. This discrepancy is trivial within a few waves when the exit point (i.e., where the groundwater level meets the beach face) converges for $h_g = 0$, 0.1, and 0.2 m trials.

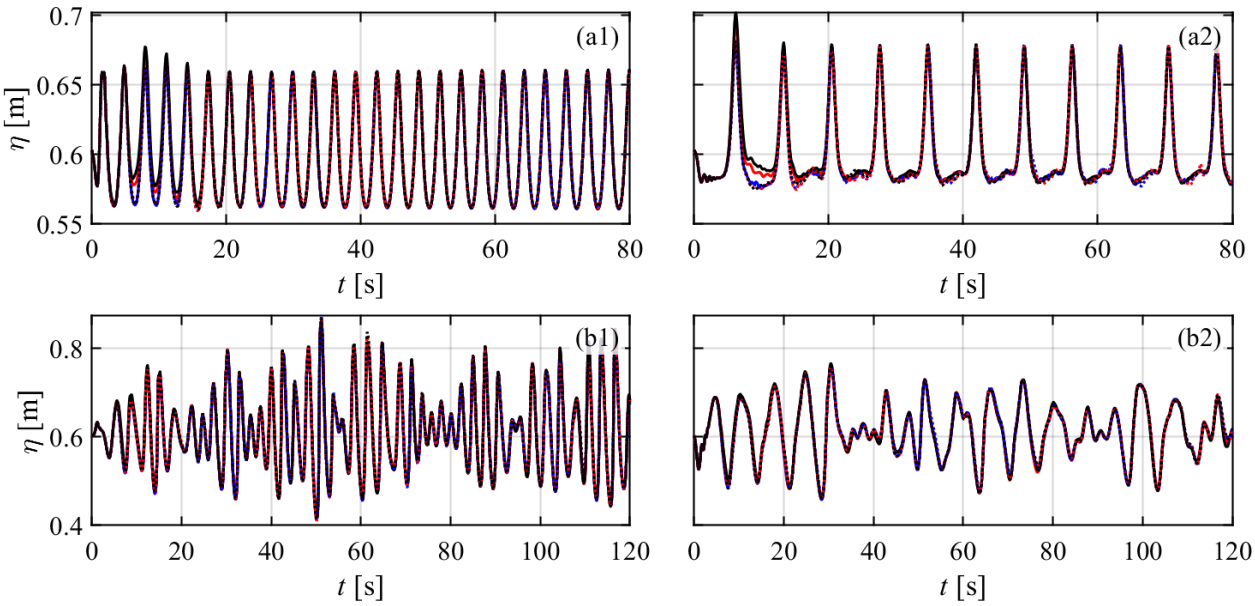

Figure 5.3: Time series of free surface elevation at the beach toe ($x = 0$ m) for (a) monochromatic wave cases with wave height $H = 0.1$ m and (b) irregular wave cases with $H = 0.25$ m. Simulations with wave periods of (1) $T = 3.1305$ s and (2) $T = 7.1554$ s are shown. Gravel (solid line) and sand (dotted line) beach results for $h_g = 0$ (blue), 0.1 (red), and 0.2 m (black) trials are shown.

5.3.2 Swash runup

5.3.2.1 Monochromatic wave conditions

The shoreline position is defined as the location where the bed-normal flow depth is equal to 5 mm (Kikkert et al., 2013; Briganti et al., 2016; Kim et al., 2017; Delisle et al., in revision). The vertical elevation of the instantaneous shoreline position, referred to as the runup position (r_z), demonstrates that wave runup is highly dependent on beach sediment characteristics (Fig. 5.4). Although both the gravel and sand beaches are defined by the same ϕ_0^s (i.e., effective porosity), the gravel beach has a higher permeability due to its larger sediment size. Prior to first wave arrival at the beach face, groundwater exfiltrates in gravel beach trials with $h_g > 0$ m, a behavior not observed in the sand beach trials (Fig. 5.4a1-

b1). In the gravel beach trials, runup evolution is nearly symmetric with sharp transitions between backwash (i.e., swash moving in the offshore direction) of one wave and uprush (i.e., swash moving in the onshore direction) of the next wave. Minimal interaction between consecutive waves is observed, evidenced by r_z returning to approximately the same elevation after each wave. The runup position converges (i.e., less than 5 mm difference in r_z between all h_g trials) for case MT3G (MT7G) at $t = 17$ s (18.6 s). The maximum r_z is 0.5% (0.9%) larger for the $h_g = 0.2$ m trial as compared to the $h_g = 0$ m for case MT3G (MT7G). This is significantly smaller than the 20% increase reported for a single dam-break driven swash event with elevated groundwater levels on a 1:10 sloping gravel beach in Delisle et al. (in revision). Significant differences in the initial groundwater depth (0.6 m versus 0.062 m) and wave height (0.1 m versus 0.25 m) likely contribute to the smaller increase in r_z observed in this study. The asymptotic peak r_z (based on the $h_g = 0$ m trial) is 97.2% (97.9%) of the maximum r_z for case MT3G (MT7G).

In the sand beach simulations, a rapid change in r_z during uprush is followed by an elongated and asymmetric decrease during backwash (Fig. 5.4a2-b2). Significant interaction between the backwash and uprush phases of consecutive waves is observed, highlighted by minimal changes in r_z between successive waves. The initial groundwater level has a longer lasting impact on r_z as compared to the gravel beach trials, with convergence of r_z occurring at $t = 34.2$ (68.7) s for case MT3S (MT7S; Fig. 5.4a2-b2). With over 10 s of maintained r_z convergence for all monochromatic cases, a simulation duration of $t = 80$ s is deemed sufficient. As compared to the $h_g = 0$ m trial for case MT3S (MT7S), the maximum r_z is 3.0% (2.8%) larger for the $h_g = 0.2$ m trial. Notably, this is similar to the 4% increase reported for a single dam-break driven swash event with elevated groundwater levels on a 1:10 sloping sand beach in Delisle et al. (in revision). The asymptotic peak r_z is 95.0% (95.8%) of the maximum r_z for case MT3S (MT7S).

Maximum wave runup increases with wave period for both the monochromatic gravel and sand beach trials. The maximum runup position and asymptotic peak r_z are ∼5% (∼4–

5%) larger for the MT7G (MT7S) case as compared to the MT3G (MT3S) case for all h_g trials. However, runup evolution is not significantly impacted. The increased time between waves in case MT7S as compared to case MT3S reduces the interaction between successive waves and a more discernible uprush-backwash pattern is observed (Fig. 5.4a2-b2). Prior to $\sim$40 s, differences in r_z between the h_g trials for case MT7S are smallest during uprush and increase during the backwash phase. The largest wave runup occurs after the first wave in all simulations except for the $h_g = 0.2$ m trial in case MT3S (maximum r_z occurs after the fourth wave).

Despite having the same porosity, swash behavior on the gravel and sand beaches varies significantly. The runup evolution in gravel beach trials is symmetric, while in sand beach trials, it is elongated and asymmetric. Swash interaction between successive waves is minimal (significant) for gravel (sand) beach trials. The maximum runup increases with wave period for both the gravel and sand beach cases. Swash evolution in the sand beach cases demonstrate greater sensitivity to the initial groundwater elevation (i.e., higher initial groundwater levels lead to increased runup magnitudes), however runup converges for all monochromatic cases.

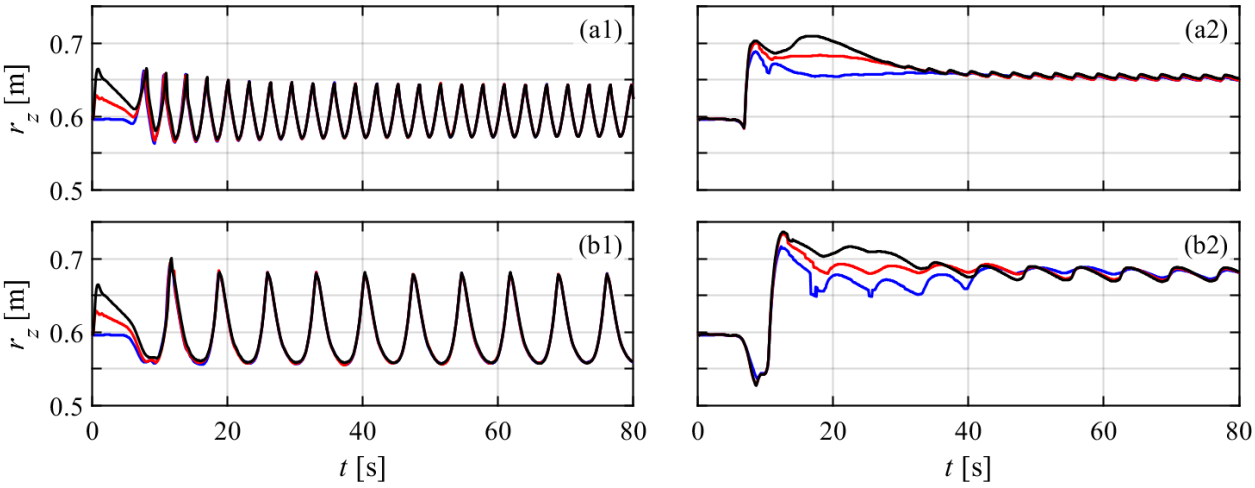

Figure 5.4: Swash runup response to monochromatic waves. Time series of runup position (r_z) with $H = 0.1$ m and (a) $T = 3.1305$ s (corresponding to Fig. 5.3a1) and (b) $T = 7.1554$ s (corresponding to Fig. 5.3a2). (1) Gravel and (2) sand simulation results for $h_g = 0$ (blue), 0.1 (red), and 0.2 m (black) trials are shown.

5.3.2.2 Irregular wave conditions

Similar to the monochromatic gravel beach cases, groundwater exfiltrates prior to the arrival of the first wave in the irregular gravel beach trials with $h_g > 0$ m (Fig. 5.5a1-b1). Distinct uprush and backwash phases are visible in r_z, although not as precisely as in the monochromatic gravel beach cases, indicating that more uprush-backwash interaction is occurring. Convergence of r_z occurs significantly later than in the monochromatic gravel beach cases at $t = 77.2$ s (79.5 s) for case IT3G (IT7G) (Fig. 5.5a1-b1). With over 40 s of maintained r_z convergence for the irregular gravel beach cases, a simulation duration of $t = 120$ s is deemed sufficient. As expected, peak r_z values vary irregularly with the waves. For all h_g trials, the maximum r_z occurs between $t = 57.2$–57.5 s (30.9–31 s) for the IT3G (IT7G) case. The average r_z, computed between $t = 10$-120 s, is 0% (0.2%) larger for the $h_g = 0.2$ m trials as compared to the $h_g = 0$ m for case IT3G (IT7G), again significantly smaller than the 20% reported in Delisle et al. (in revision).

The runup position evolution for the irregular sand beach trials does not display clear uprush and backwash features for each wave (Fig. 5.5a2-b2). The same general trend in r_z is observed for all of the h_g trials, however the magnitude of changes due to the wave climate varies. Although there are periods where r_z nearly converges (e.g., t ∼22–25, 35–40 s for case IT3S, t ∼19–21, 104–106 s for case IT7S), the h_g = 0.2 m (0 m) trial persistently exhibits the highest (lowest) r_z for both IT3S and IT7S cases. Differences in r_z between the h_g trials range from ∼0–9 cm (∼0–11 cm) for case IT3S (IT7S). For the IT3S case, the maximum r_z occurs slightly later than in the IT3G case between t = 58.2–58.5 s for all h_g trials. The time of maximum r_z in case IT7S occurs later than case IT7G and is dependent on the initial h_g, occurring at t = 38.2, 113.5, and 40.4 s for h_g = 0, 0.1, and 0.2 m, respectively. With the exception of a few seconds during decreasing r_z at t ∼25 s for case IT3S and near immediately when the first wave reaches the beach face for case IT7S, the instantaneous r_z is largest (smallest) for the h_g = 0.2 m (0 m) trial. The average r_z, computed between t = 10-120 s, is 4.4% (6.2%) larger for the h_g = 0.2 m trials as compared to the h_g = 0 m for case IT3S (IT7S), similar to the 4% reported in Delisle et al. (in revision).

In contrast to the monochromatic cases, maximum r_z decreases with wave period for both the irregular gravel (by ∼8–9%) and sand beach (by ∼6–11%) trials. Wave ordering may play a non-negligible role in this behavior as case IT3S is exposed to approximately double the amount of waves as compared to case IT3G. Due to the nature of irregular waves, it is difficult to directly compare the impact of wave period on runup behavior, however the duration of r_z peaks in case IT7G are noticeably increased as compared to case IT3G (i.e., r_z peaks appear flatter; Fig. 5.5a1-b1). The runup position in case IT7S also increases more rapidly at the start of the simulation as compared to case IT3S (Fig. 5.5a2-b2).

Swash uprush and backwash behavior in the irregular gravel and sand beach cases closely resemble that of the monochromatic cases. In contrast to the monochromatic cases, the maximum runup decreases with wave period for both the irregular gravel and sand beach cases. For the gravel beach cases, runup converges regardless of the initial groundwater level.

Conversely, the runup position for the sand beach trials consistently remains highest (lowest) for the highest (lowest) initial groundwater level, even after periods of near-convergence. Moreover, the timing of maximum runup in sand beach trials (particularly for the longer wave period) is influenced by the initial groundwater level.

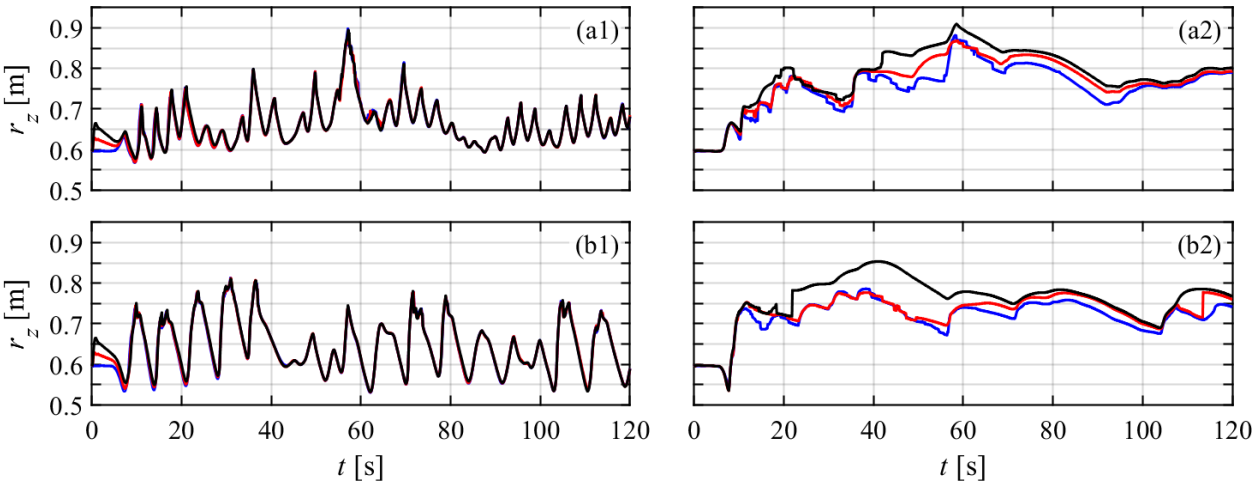

Figure 5.5: Swash runup response to irregular waves. Time series of runup position (r_z) with $H = 0.25$ m and (a) $T = 3.1305$ s (corresponding to Fig. 5.3c1) and (b) $T = 7.1554$ s (corresponding to Fig. 5.3c2). (1) Gravel and (2) sand beach simulation results for $h_g = 0$ (blue), 0.1 (red), and 0.2 m (black) trials are shown.

5.3.3 Infiltration capacity and near-bed turbulence

SedOlaFlow enables detailed investigation of swash surface and subsurface near-bed processes. Infiltration capacity and turbulence are explored by comparing trials with initial groundwater levels of $h_g = 0$, 0.1, and 0.2 m for each case described in Table 5.1. The beach face infiltration capacity (or volume available for infiltration), V_g, is calculated as the amount of pore space available within 5 cm below the beach face between the beach toe and

instantaneous runup position:

$$V_g(t) = dx * dz * \sum_{z=z_b-0.05}^{z_b} \sum_{x=0}^{x(r_z(t))} (\phi^f(t) - 1)(1 - \phi^s). \tag{5.3}$$

V_g is a function of sediment porosity and fluid volume and is affected by swash infiltration, subsurface flow, and groundwater exfiltration. The black outlined regions (extending offshore to the beach toe) in Figure 5.6b1-b2 indicate the V_g calculation region. Note that only fluid within the calculation region is shown in panels (b1) and (b2); the complete profiles are shown in (a1) and (a2). Tan areas represent dry conditions (i.e., absence of fluid) and dark grey regions represent fully saturated conditions (i.e., presence of fluid). The beach face infiltration capacity for the instances shown are $V_g = 0$ m^2 (Fig. 5.6b1) and $V_g = 3.1\times10^{-3}$ m^2 (Fig. 5.6b2).

The beach face turbulent kinetic energy, TKE, is calculated as the average k^f (see Eq. (2.35)) value within 5 cm above the beach face between $x = 2$ m offshore of the instantaneous runup position and the maximum swash extent. Due to the rapid decrease in fluid velocity beneath the beach face, subsurface TKE is not taken into account. The black outlined regions in Figure 5.6c1-c2 indicate the TKE calculation region; the onshore border of the calculation region follows the onshore runup/rundown edge and varies with the swash evolution. The beach face turbulence for the snapshots shown are TKE $= 6.6\times10^{-3}$ m^2/s^2 (Fig. 5.6c1) and TKE $= 9.3\times10^{-2}$ m^2/s^2 (Fig. 5.6c2).

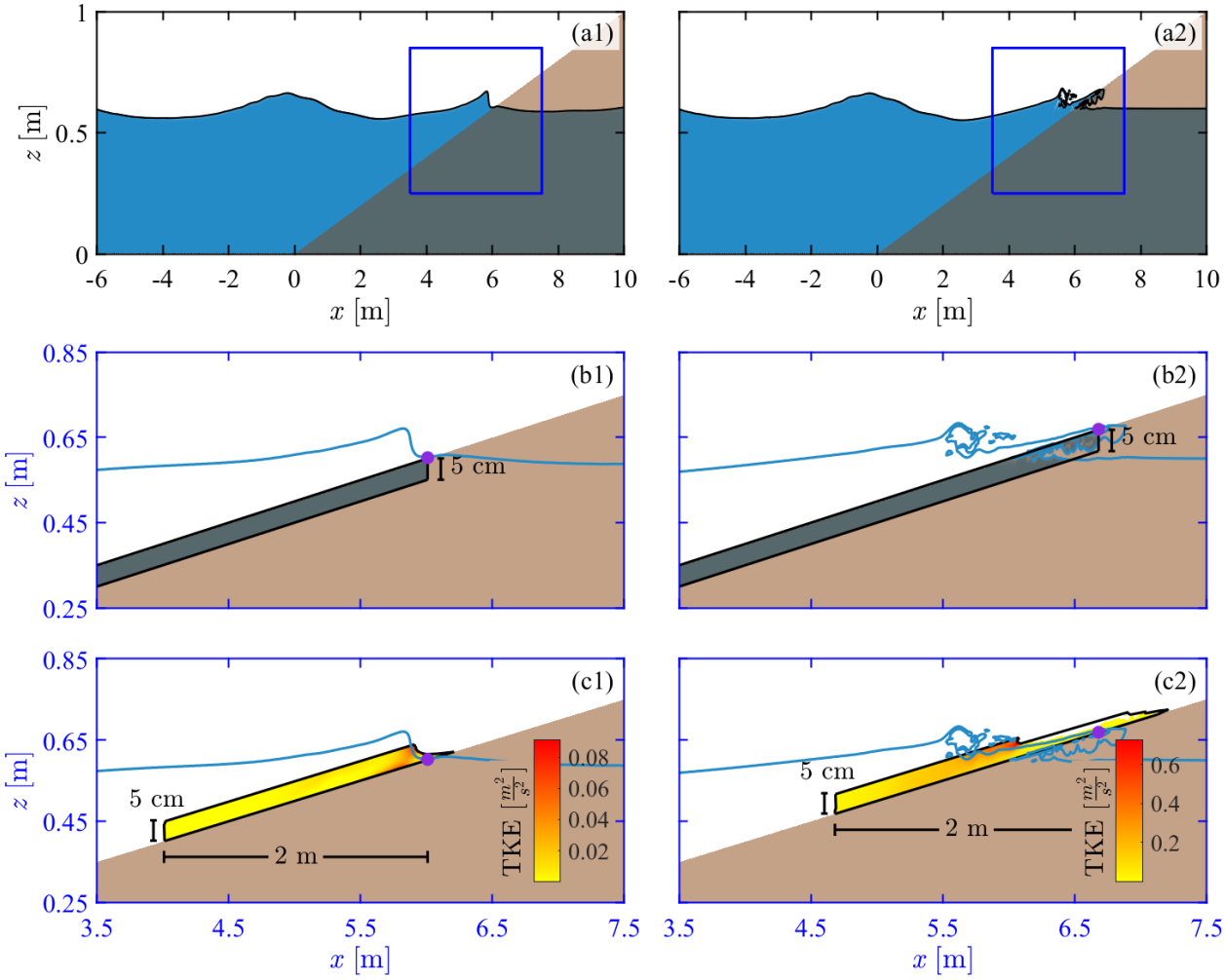

Figure 5.6: Snapshots of (a) the fluid profile, (b) infiltration capacity (V_g) calculation region (black outline), and (c) beach face turbulence (TKE) calculation region (black outline) at t = 10 s for (1) MT3G and (2) MT3S trials with h_g = 0 m. The ϕ^f = 0.5 contour is shown as the black line in (a) and blue lines in (b) and (c). The purple circles in (b) and (c) mark the location of the instantaneous r_z.

5.3.3.1 Monochromatic wave conditions

Initially, V_g in the monochromatic gravel beach cases is largest (smallest) for the $h_g = 0$ m (0.2 m) trial (Fig. 5.7c1-2). As expected, higher antecedent groundwater levels reduce the initial beach face infiltration capacity. The arrival of the first wave at the beach causes r_z and V_g to increase until peak r_z is reached. Subsequently, V_g experiences a rapid decline, followed by a slower decrease for a few seconds, and then another rapid decline until a minimum V_g is reached during the beginning of the next wave's uprush phase. This cyclic behavior continues for each wave, with the peak V_g remaining near-constant and the minimum V_g decreasing with each wave, eventually reaching $V_g = 0$ m^2 between waves. The infiltration capacity increases rapidly with the runup position and declines more slowly during rundown; eventually, the beach face becomes completely saturated at between waves when runup is at its minimum. Noticeably, the maximum V_g is an order of magnitude larger in case MT7G as compared to case MT3G, likely because the swash travels further across the beach face in case MT7G.

TKE follows a similar pattern of reaching a peak value in phase with r_z, followed by a rapid decline during backwash (Fig. 5.7d1-2). However, TKE rebounds during the final seconds of backwash and then declines again until a minimum TKE is reached during the beginning of the next wave's uprush. As with V_g, this behavior persists for the entire wave series, with the peak TKE growing slightly until a peak asymptote is reached around $t \sim$40 s for both MT3G and MT7G cases. TKE is initially largest during backwash in the $h_g = 0.2$ m trial which is likely due to the interaction of surface flows and groundwater exfiltrating at the beach face; less groundwater exfiltration occurs in the $h_g < 0.2$ m trials leading to smaller TKE values as compared to the $h_g = 0.2$ m trial. Peak TKE values, however, are consistently smallest (largest) for the $h_g = 0.2$ m (0 m) trials. The infiltration capacity converges (i.e., less than 10^{-5} m^2 difference in V_g between all h_g trials) at $t = 17$ s (18.6 s), slightly before the beach face turbulence converges (i.e., less than 0.005 m^2/s^2 difference in TKE between all h_g trials) at $t = 18.8$ s (21.6 s) for case MT3G (MT7G).

Investigation of the monochromatic sand beach cases reveals differences in the V_g and TKE evolution as compared to the monochromatic gravel beach cases (Fig. 5.8c1-d2). Large differences between V_g for the $h_g = 0$ m and $h_g > 0$ m trials are initially observed; this can be attributed to r_z exceeding the exit point of the $h_g = 0$ m trial (MT3S and MT7S) and only slightly exceeding the exit point of the $h_g = 0.1$ m trial (MT7S only; not shown). The passage of waves across the beach face is evident in the TKE evolution, however TKE does not rebound during backwash as was observed in the monochromatic gravel beach cases. This suggests that TKE is increased by groundwater exfiltration and swash backwash interactions, a behavior not observed in the sand beach cases where limited exfiltration occurs. TKE increases with the first few waves until reaching a maximum, at which point it decreases to a peak asymptote as observed in the monochromatic gravel beach cases. With the exception of the MT3S $h_g = 0.2$ m trial, the maximum r_z and V_g occur in phase with each other and slightly before the maximum TKE. For case MT3S, maximum r_z lags behind both maximum V_g and TKE.

To account for the order of magnitude larger V_g in the monochromatic sand beach cases as compared to the monochromatic gravel beach cases, V_g convergence is defined for the monochromatic sand beach cases as a difference of less than 10^{-4} m^2 in V_g between all h_g trials. In case MT3S, V_g converges at $t = 19.5$ s, significantly before r_z converges at $t = 34.2$ s, and TKE does not converge. The difference in TKE between $h_g = 0.2$ m and $h_g = 0.1$ m (0 m) does however stabilize at a difference of $\sim$0.01 m^2/s^2 ($\sim$0.02 m^2/s^2). In case MT7S, V_g for the $h_g = 0$ m and $h_g = 0.1$ m trials converge at $t = 47.4$ s ($h_g = 0.2$ m does not), prior to r_z convergence at $t = 68.7$ s, and TKE does not converge.

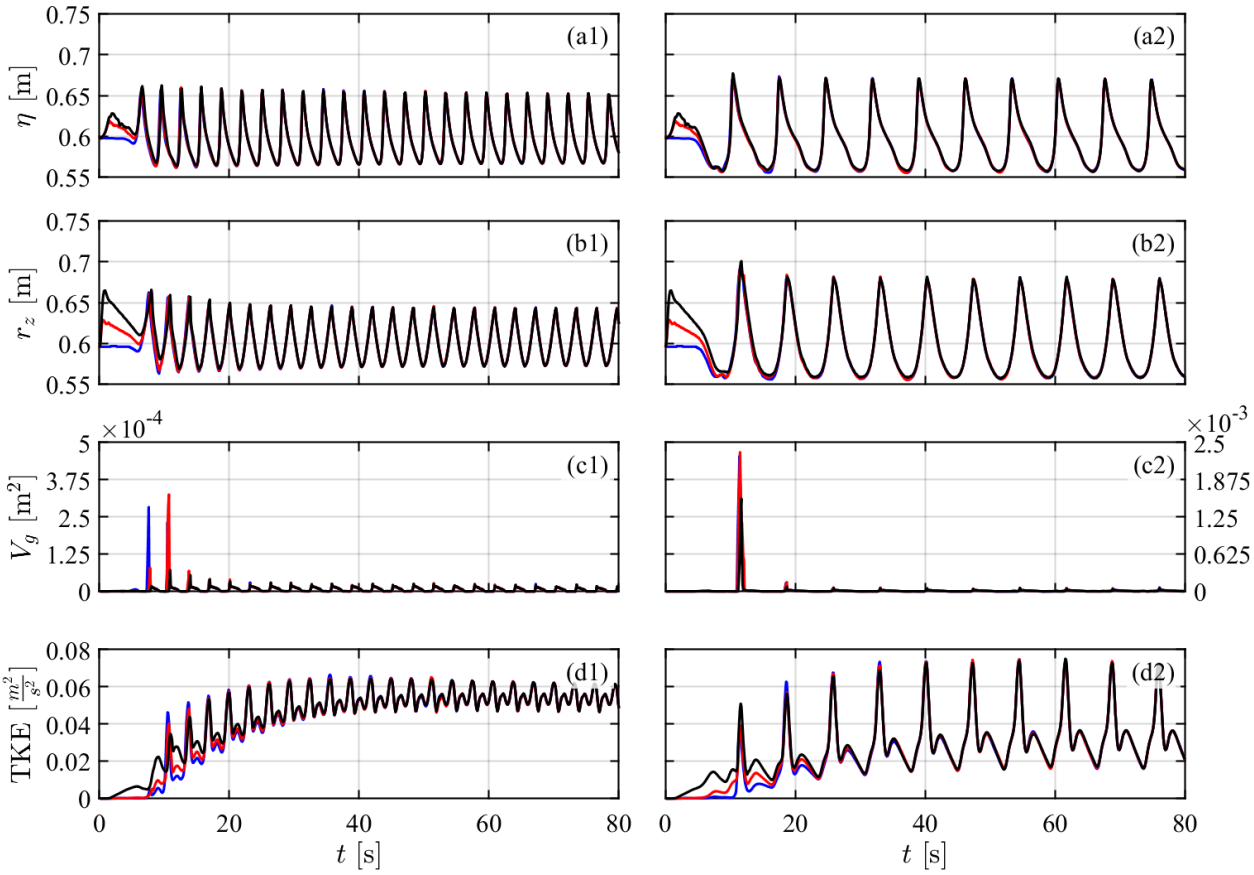

Figure 5.7: Monochromatic, gravel beach results. Time series of (a) free surface elevation at $x = 5$ m, (b) runup position (r_z), (c) infiltration capacity (V_g), and (d) turbulent kinetic energy (TKE) with (1) $T = 3.1305$ s (MT3G) and (2) $T = 7.1554$ s (MT7G). Simulation results for $h_g = 0$ (blue), 0.1 (red), and 0.2 m (black) trials are shown. Note that (c1) and (c2) have different vertical axes limits.

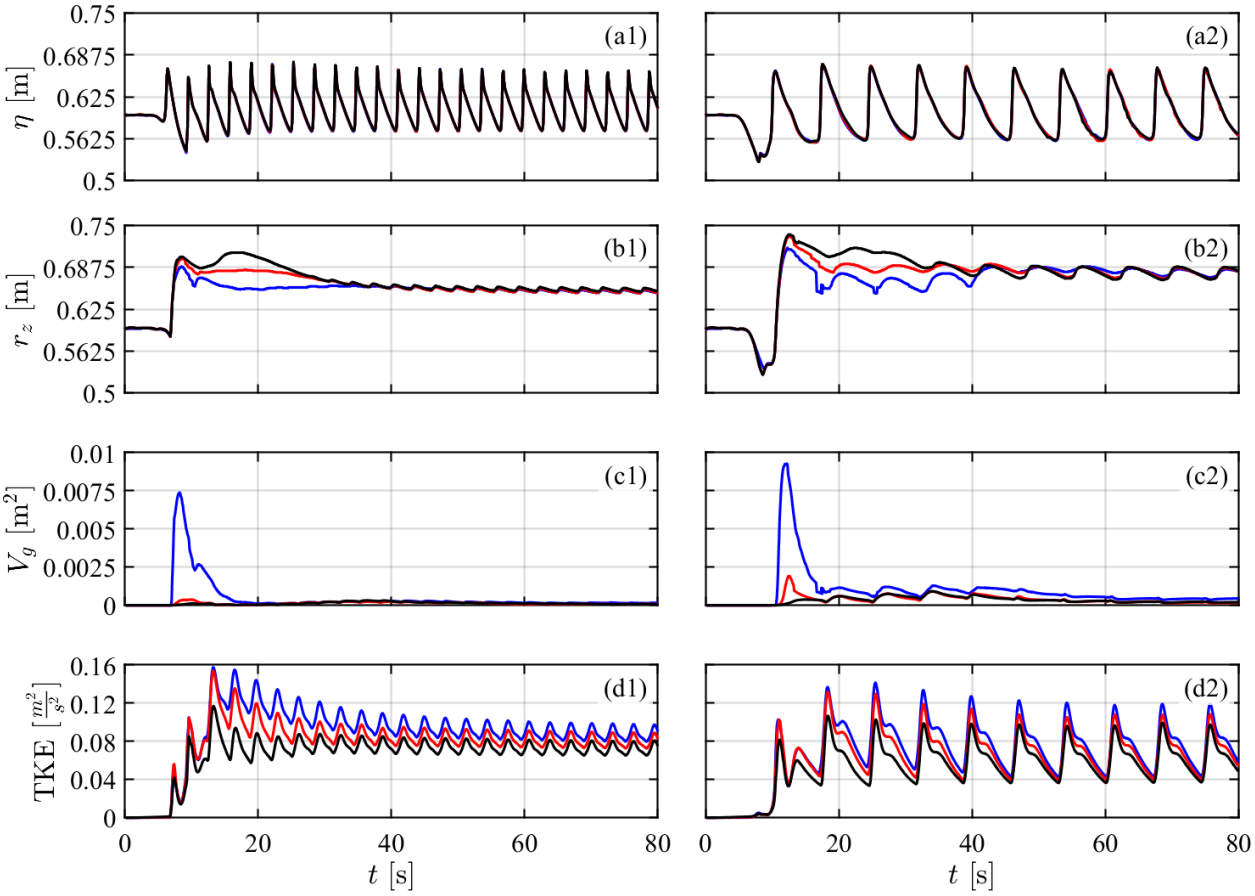

Figure 5.8: Monochromatic, sand beach results. Time series of (a) free surface elevation at $x = 5$ m, (b) runup position (r_z), (c) infiltration capacity (V_g), and (d) turbulent kinetic energy (TKE) with (1) $T = 3.1305$ s (MT3S) and (2) $T = 7.1554$ s (MT7S). Simulation results for $h_g = 0$ (blue), 0.1 (red), and 0.2 m (black) trials are shown.

5.3.3.2 Irregular wave conditions

Nonuniform wave conditions in the irregular wave cases increase the complexity of near-bed process. However, as observed in the monochromatic gravel beach cases, the impact of h_g on r_z is negligible in the irregular gravel beach cases due to rapid groundwater exfiltration prior to waves arriving at the beach face. Near-identical r_z, V_g, and TKE evolution across all h_g trials simplifies the investigation of near-bed processes' role in r_z behavior under irregular wave forcing (Fig. 5.9). In case IT3G, the first four waves to reach the beach face are increasing in magnitude, however r_z does not monotonically increase (Fig. 5.9a1-c1). V_g peaks with each of these first few waves and then remains at near-zero until the largest runup event at $t \sim$57 s before returning to near-zero. V_g does not mirror the increases in r_z at $t \sim$36 s and $\sim$50 s as horizontal subsurface flow pushes the groundwater exit point onshore beyond r_z (not shown). In contrast, V_g in case IT7G is more variable and responsive to wave events, likely due to increased time and exfiltration between successive waves as compared to case IT3G (Fig. 5.9a2-c2).

The irregular sand beach cases show persistent differences in r_z between h_g trials, even after periods of r_z convergence (Fig. 5.10). The behavior of V_g and TKE largely follow the same trends observed in the irregular gravel beach cases. For both cases IT3S and IT7S, i.e., both short and long waves, the variability in V_g decreases with h_g and after maximum r_z is reached there is significantly less V_g fluctuation for all h_g trials (Fig. 5.10b1-c2). The higher initial groundwater level in $h_g > 0$ m trials limits infiltration until r_z exceeds the groundwater exit point at $t = 17$ s (9.5 s) for the $h_g = 0.1$ m trial in case IT3S (IT7S) (not shown). The differences in TKE between h_g trials fluctuates significantly; generally, the difference is largest during TKE peaks and smallest at TKE minimums.

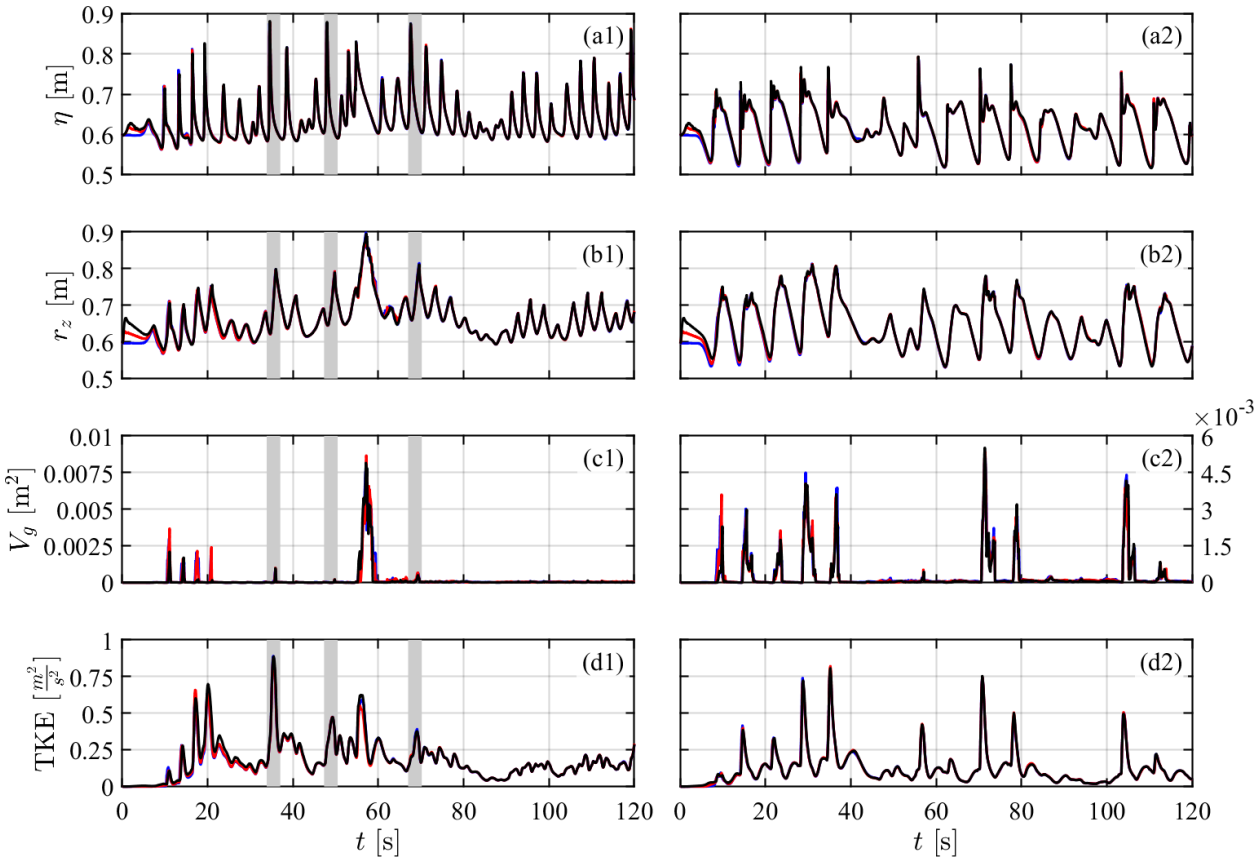

Figure 5.9: Irregular, gravel beach results. Time series of (a) free surface elevation at x = 5 m, (b) runup position (r_z), (c) infiltration capacity (V_g), and (d) turbulent kinetic energy (TKE) with (1) T = 3.1305 s (IT3G) and (2) T = 7.1554 s (IT7G). Simulation results for h_g = 0 (blue), 0.1 (red), and 0.2 m (black) trials are shown. The gray vertical lines in (a1)-(d1) correspond to t = 35.5 s, 48.9, and 68.6 s (left to right). Note that (c1) and (c2) have different vertical axes limits.

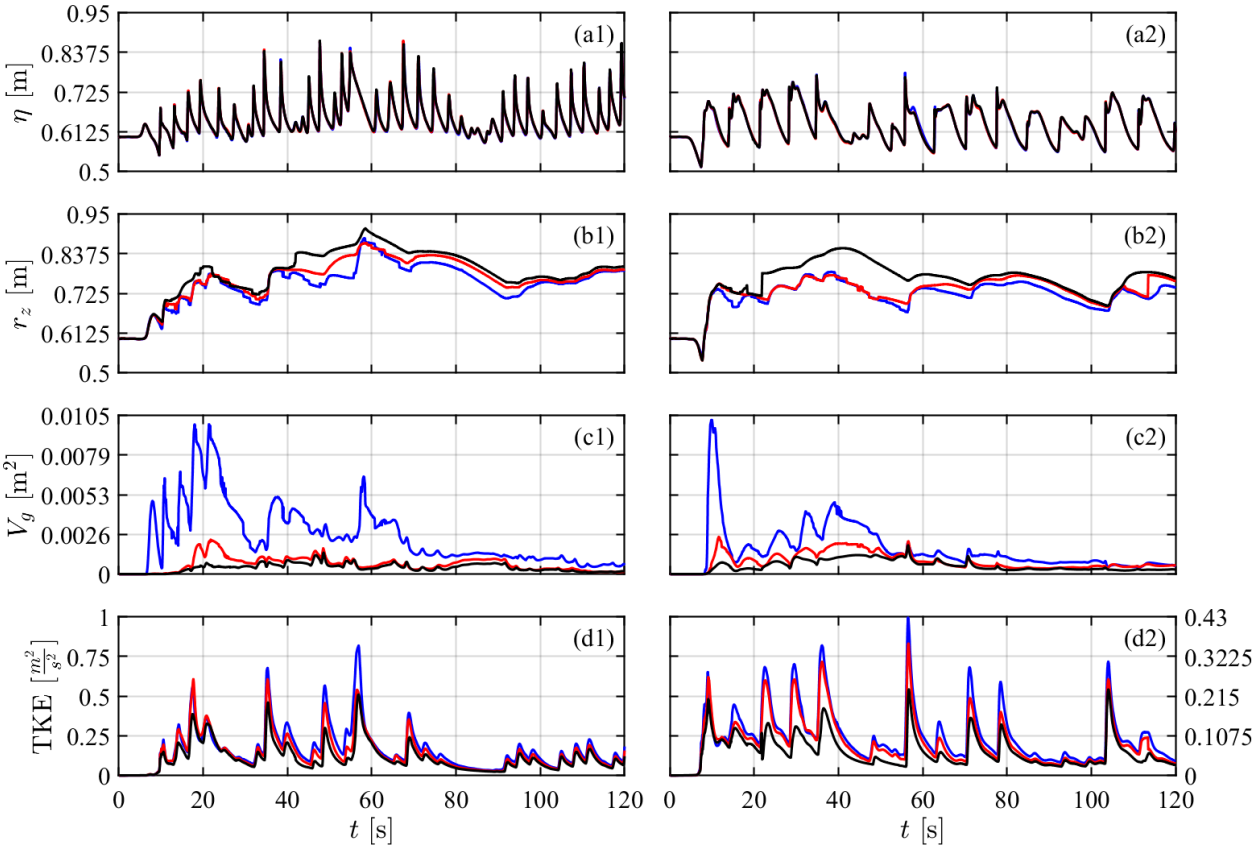

Figure 5.10: Irregular, sand beach results. Time series of (a) free surface elevation at $x =$ 5 m, (b) runup position (r_z), (c) infiltration capacity (V_g), and (d) turbulent kinetic energy (TKE) with (1) $T = 3.1305$ s (IT3S) and (2) $T = 7.1554$ s (IT7S). Simulation results for $h_g = 0$ (blue), 0.1 (red), and 0.2 m (black) trials are shown. Note that (d1) and (d2) have different vertical axes limits.

5.4 Discussion

The numerical simulations presented in this study were designed to provide insight into the swash and beach groundwater behavior of realistic beaches (see Table 5.1). During a rising tide, the shoreline (i.e., where the mean water level meets the beach face) and groundwater exit point are typically at the same elevation (i.e., $h_g = 0$ m trials). As the tide falls however, the ocean water level may decline faster than the beach exfiltration rate leading to a groundwater overheight (i.e., $h_g = 0.1$ and 0.2 m trials; e.g., Nielsen, 1990; Steenhauer et al., 2011; Heiss et al., 2015). The simulations presented in this work implement an idealized beach with homogeneous, immobile sediment and constant slope, conditions that are unlikely in reality. Nevertheless, these simplifications are essential to enable the study of complex near-bed processes and improve our fundamental understanding of the swash–groundwater relationship.

5.4.1 Saturation and near-bed turbulence

Infiltration capacity is intrinsically tied to runup extent as the further swash travels, the more potential space for infiltration above the groundwater table. In the monochromatic gravel case, the differences in V_g and TKE between h_g trials are most significant at the start of the simulation (Fig. 5.7c1-d2). Large differences in V_g can be attributed to h_g as r_z exceeds the exit point of only the $h_g = 0$ m trial before the exit points of all h_g trials converge after a few waves (not shown). A similar behavior in TKE, i.e., that lower initial groundwater levels exhibit increased TKE, suggests that beach face saturation plays a role in turbulence. Convergence of V_g and TKE at nearly the same time as r_z for the monochromatic gravel beach cases hints that these near-bed processes are closely linked with swash evolution.

As opposed to the monochromatic gravel beach cases however, r_z, V_g, and TKE evolution do not coincide in the monochromatic sand beach simulations (Fig. 5.8c1-d2). Both differences in V_g and TKE likely contribute to the initial discrepancy in r_z, however even after

V_g converges, the runup position is largest (smallest) for the $h_g = 0.2$ m (0 m) trial in both MT3S and MT7S cases (Fig. 5.8b1-d2). V_g alone cannot explain the observed differences in r_z for the h_g trials. During the time period after V_g convergence, both the magnitude and difference in TKE between h_g trials declines with r_z. As r_z converges, TKE reaches a steady-state in which the $h_g = 0.2$ m (0 m) trial has the lowest (highest) TKE. This behavior suggests that TKE plays a non-negligible role in modulating swash evolution. The sustained difference in TKE between h_g trials even after r_z convergence may be partially attributed to a more onshore (offshore) exit point for the $h_g = 0.2$ m (0 m) case (not shown). Results from the monochromatic gravel and sand beach cases demonstrate that the impact of antecedent groundwater levels on swash evolution is negligible once a steady-state or equilibrium has been reached. As such, the monochromatic wave cases provide an important baseline for V_g and TKE behavior but do not clearly reveal the role of near-bed processes on swash evolution.

Under irregular wave forcing, antecedent beach conditions significantly impact V_g and TKE. The largest TKE in case IT3G is observed at $t \sim 36.1$ s, corresponding to the largest wave and a sharp increase in r_z (Fig. 5.9a1-d1, leftmost gray vertical line). However, waves of similar magnitudes at $t \sim 49.8$ s (middle gray vertical line) and $t \sim 69.6$ s (rightmost gray vertical line) have significantly smaller TKE values. Of these three waves, the largest r_z is observed when TKE is smallest (i.e., $t \sim 70$ s). Notably, this occurs after the maximum r_z has been reached at $t = 57.2$ s; maximum r_z does not occur after the largest wave but after several mid-sized runup event. These results suggest that preceding waves saturate the beach face, which in turn, diminishes TKE, leading to runup traveling further onshore. Under more saturated beach conditions, runup is enhanced though momentum retention associated with lower TKE and minimal infiltration mass losses. Past swash impacts are less evident under longer wave period conditions when increased groundwater exfiltration occurs between waves reducing beach face saturation (i.e., case IT7G; Fig. 5.9a2-d2).

Only the irregular, sand beach cases demonstrate sustained differences in r_z between h_g

trials. Divergence of r_z is associated with increased differences between V_g and TKE. At t ~40 s for example (for both cases IT3S and IT7S), the increasing difference in r_z between $h_g = 0$ m and $h_g = 0.2$ m trials corresponds to increased separation in V_g and TKE (Fig. 5.10b1-d2). While the $h_g = 0$ m and $h_g = 0.1$ m trials exhibit the most similar r_z and TKE magnitudes and behaviors, V_g for the $h_g = 0.1$ m and $h_g = 0.2$ m trials are more closely matched. This may suggest a groundwater level threshold exists at which runup impacts are realized, likely dependent on the wave conditions and beach sediment characteristics. The role of beach saturation in reducing TKE is highlighted in case IT3S at $t = 57$ s (Fig. 5.10c1-d1). At this time, only the $h_g = 0$ m trial shows a rapid rise in V_g and the associated peak in TKE is significantly larger compared to the $h_g > 0$ m trials. Notably, r_z and V_g are largest (smallest) and TKE is smallest (largest) for trial $h_g = 0.2$ m (0 m).

The authors propose that elevated antecedent groundwater levels can increase runup levels by (1) creating a saturated beach face that (2) reduces infiltration and beach face turbulence which (3) enables swash runup to propagate further onshore (hereby referred to as the *swash–groundwater relationship*). This phenomena can also occur temporarily after individual waves saturate the beach face (as observed in case IT3G). However, as opposed to individual swash excursions, beach face saturation due to a groundwater overheight (i.e., groundwater table above the offshore water level) has a persistent impact on runup evolution. In evaluating the runup evolution for various beach and wave conditions presented in this work, it is evident that the bi-directional relationship between swash and beach groundwater flows is highly complex.

5.4.2 Application to natural beaches

5.4.2.1 Beach characteristics

Beach and sediment properties play an important role in the swash–groundwater relationship. For both the monochromatic and irregular wave cases, the influence of antecedent

groundwater level on runup amplitude is most significant for the sand (lower permeability) beach. In contrast, larger changes in swash extent were observed on higher permeability beaches for a single swash event (Delisle et al., in revision). Beaches with higher permeability will experience the reduced infiltration capacity associated with elevated groundwater levels more quickly. On lower permeability beaches, it takes more time for water to infiltrate and reach the groundwater table, so an elevated groundwater table will cause only a minimal reduction in the infiltration capacity beyond the exit point for a single swash event. However, after the beach becomes saturated, the infiltration capacity will remain near-zero whereas on a higher permeability beach, rapid exfiltration would allow the infiltration capacity to rebound between successive waves. This likely explains why for a single, relatively large swash event, the influence of beach groundwater on runup extent was more pronounced on the higher permeability beach and the reverse was true under periodic wave conditions. Lower permeability beaches may be more prone to regular impacts (i.e., increased runup and coastal flooding) from elevated groundwater levels, while higher permeability beaches may be more susceptible under extreme, isolated events (e.g., hurricanes, tsunamis).

This study is limited to beaches with homogeneous, uniformly distributed sediment. Studies exploring the impact of heterogeneous and composite (e.g., gravel and sand) beaches would provide valuable insights as heterogeneity in sediment composition can result in varying (i.e., increased or decreased) permeability and porosity. It is expected, however, that the fundamental role of permeability in the swash–groundwater relationship will not change due to sediment heterogeneity. The influence of beach slope on the swash–groundwater relationship was also not explored in this study and should be further investigated, particularly considering the inconclusive findings reported in Delisle et al. (in revision). It is anticipated that beach slope will play a complicated role in the swash–groundwater relationship; for the same increase in groundwater level, a steep beach would both create a larger change in infiltration capacity and smaller change in beach face saturation as compared to a mildly sloping beach. Notably, groundwater overheights increase as permeability, sediment size, and beach

slope decrease (Gourlay, 1992; Kang and Nielsen, 1996; Turner et al., 1997b). Permeability will likely play a key role in modulating whether beach slope changes to infiltration capacity or beach face saturation will have a more significant impact on the swash–groundwater relationship.

5.4.2.2 Incident wave conditions

Incident wave conditions have a significant impact on the swash–groundwater relationship. Under monochromatic wave conditions, the antecedent groundwater level is observed to have a minimal impact on runup magnitude that decreases until the runup is identical regardless of initial groundwater condition. It is worth noting that the wave height in the monochromatic cases was relatively small with a non-linearity parameter (wave height to wave depth ratio) of 0.167. Notably, when comparing runup between a higher and lower antecedent groundwater levels, the results suggest that runup will not change unless the runup amplitude exceeds the exit point of the lower antecedent groundwater level. As wave height increases, it is expected that the impact of the initial groundwater level on monochromatic wave runup will increase in duration due to larger differences in the infiltration capacity and beach face turbulence. When swash infiltration is balanced by beach exfiltration, both the runup amplitude and groundwater level are expected to stabilize (Hegge and Masselink, 1991).

Examining the role of groundwater levels on swash runup for monochromatic waves yields valuable insight into the swash–groundwater relationship, however, irregular wave conditions are far more common in natural beach environments. Focusing on the sand beach cases, sustained differences in the runup position for varying antecedent groundwater levels are observed for incident wave heights between ∼0.06–0.45 m. Larger variations in runup occurred during periods of increasing wave variability and magnitude (e.g., between t = 40–60 s, Fig. 5.10a1-b2), suggesting that the impact of antecedent groundwater levels on runup magnitudes increases with wave height. It is important to recognize that swash infiltration also contributes to the groundwater table elevation (e.g., Hegge and Masselink, 1991). This

could potentially cause a reinforcing cycle in which higher antecedent groundwater levels increase the runup amplitude, which in turn, increase swash infiltration and the groundwater table elevation. This may partially explain why the order in which waves arrive at the beach face impacts runup evolution. Waves that exceed the exit point of the beach saturate the beach face (and by extension reduce TKE), reduce the beach face infiltration capacity, and increase the groundwater level, all processes that are shown to increase runup magnitudes. It is expected then that if comparing scenarios of (a) small waves followed by large waves and (b) large waves followed by small waves, the runup magnitude of the small waves will be larger for scenario (b) than (a). This cycle is likely escaped in nature when wave height decreases or runup no longer exceeds the exit point. The impacts of this cycle would be less noticeable in higher permeability beaches for the reasons described in Section 5.4.2.1.

Extreme wave events like hurricanes and tsunamis were not studied in this work though previous work suggests that antecedent groundwater levels play a non-negligible role in their runup evolution (Delisle et al., in revision). In comparing extreme to typical wave conditions, the significance of the groundwater table elevation in relation to the overall runup magnitude may be diminished. This is because the increase in runup distance resulting from higher groundwater levels will constitute a smaller proportion of the total runup extent. Longer wave periods generally tend to result in larger runup magnitudes, suggesting that increasing wave period would increase the influence of antecedent beach groundwater conditions on runup. However, wave merging is more likely to occur for shorter wave periods and there is less time for exfiltration between waves (i.e., the beach face stays saturated). It is therefore difficult to extrapolate the impact of wave period on the swash–groundwater relationship. It may be useful for future work to consider the impact of frequency (i.e., $1/T$) spread rather than simply wave period to gain a better understanding of natural conditions.

Infragravity waves cannot be captured in the model domain, which have an impact on both runup and groundwater evolution (e.g., Sous et al., 2013; Anarde et al., 2020). The influence of wave direction, wave focusing, and alongshore flows are also not modeled. Further

investigation of various wave conditions should be conducted to determine which conditions are most sensitive to the swash–groundwater relationship. While no antecedent groundwater level impacts were observed in the irregular gravel beach cases, this is likely attributable to beach characteristics rather than incident wave conditions and underscores the intricate relationship between wave conditions, beach characteristics, and swash–groundwater dynamics. This complex relationship implies that not all beaches are susceptible to increased runup from higher groundwater conditions. Temporal variations in beach and wave conditions will cause the impact of antecedent groundwater levels on runup amplitude to vary for the same beach, and some beaches may only experience the effects intermittently or not at all.

5.4.3 Implications on coastal vulnerability

While the swash–groundwater relationship is not a novel phenomenon in nature, it has been largely overlooked in coastal hazard planning and assessments. Including the effects of antecedent groundwater levels on runup behavior has the potential to significantly increase coastal flooding magnitude predictions. In this section, the impact of the swash–groundwater relationship in relation to various (non-exhaustive) aspects of coastal hazards is examined to advance our understanding of coastal vulnerability. It is expected that these impacts will vary depending on beach and wave characteristics. Therefore, the analysis focuses on the general scenario of a beach that exhibits increased runup in response to elevated groundwater conditions.

5.4.3.1 Temporal dynamics

Timing plays a crucial role in coastal vulnerability. Coastal hazard planning and modeling are conventionally assessed at high tide to represent the "worst-case scenario" flooding events (e.g., NOAA National Storm Surge Risk Maps; Gallien et al., 2014; Griggs and Reguero, 2021). However, the results in this work and experimental data (e.g., Turner and Masselink,

1998) suggest that maximum wave runup may coincide with maximum groundwater levels rather than high tide. This implies that beach groundwater can temporarily have a larger influence on coastal flooding extent than offshore water levels. The specific threshold at which the impact of groundwater on runup no longer supersedes the reduction in offshore water level will vary depending on local environmental conditions. These findings carry considerable implications for coastal management, particularly for nuisance (high tide or sunny-day) flooding. Contrary to intuition, maximum flooding extent may occur after high tide due to the swash–groundwater relationship, with important ramifications for emergency response mobilization.

Given identical wave conditions and offshore water level, runup will travel further on a falling (rather than rising) tide due to higher groundwater levels. Large waves and storm events occurring during a falling tide will consequently pose a more significant threat compared to those transpiring during a rising tide. Notably, storm surge magnitudes escalate when coinciding with a receding or low tide, while the converse holds true for a rising or high tide (Rego and Li, 2010; Lin et al., 2012; Thomas et al., 2019). Increased runup caused by the swash–groundwater relationship will exacerbate the non-linear surge amplification during falling tides. Furthermore, elevated groundwater levels will prolong the duration required for coastal flood recovery (e.g., Housego et al., 2021). Coastal vulnerability is increased during falling tides when elevated groundwater levels intensify runup extent and exacerbate storm surge amplification.

5.4.3.2 Environmental factors

Improved understanding of compound hazards (i.e., storm surge, waves, and precipitation) is essential to improve hazard projections and mitigate risk (e.g., Wahl et al., 2015; Zscheischler et al., 2018). Precipitation can intensify coastal flooding by contributing to overland flow and by increasing the potential for groundwater emergence through infiltration. However, the results of this study suggest another pathway for rainfall to worsen coastal flooding; beach

face saturation. This work demonstrates that beach face saturation (whether the result of individual swash excursions or elevated groundwater levels) diminishes turbulence and in turn increases runup magnitudes. The amplifying effect on runup extent appears indiscriminate of the saturation method, suggesting that precipitation may also increase swash excursions, further contributing to coastal flooding. The impacts of precipitation-driven beach face saturation on runup are expected to be more pronounced on lower permeability beaches due to decreased infiltration rates.

The vulnerability of a coastal region is largely tied to the physical nature and shape of the landform. Narrow beaches that are adjacent to another body of water (e.g., bay or estuary backed beaches, sand spits, barrier islands) are exposed to increased flooding risks from dual-pathway water level forcings. Additionally, these beaches may face heightened coastal flooding risks arising from the swash–groundwater relationship. Beach groundwater elevations generally decrease with distance from the shoreline and groundwater bulges can travel significant distances inland (Rotzoll and El-Kadi, 2008; Housego et al., 2021). In regions where the backshore is a body of water, however, the groundwater table is constrained to connect with the backshore surface water elevation. Consequently, beaches in these areas are subjected to higher groundwater levels than would otherwise be experienced. This implies that water-backed beaches are particularly vulnerable to groundwater-induced increases in runup extent.

5.4.3.3 Sea level rise

SLR will both exacerbate a wide range of existing coastal hazards (e.g., energetic waves, storm surge, erosion; Cayan et al., 2008; FitzGerald et al., 2008; Heberger et al., 2009; Mastrandrea and Luers, 2012) and pose new challenges. Coastal groundwater levels will increase at approximately the same rate as the sea level (e.g., Bjerklie et al., 2012; Rotzoll and Fletcher, 2013; Hoover et al., 2017) which is expected to worsen coastal management issues as the frequency of infrastructure breaches and groundwater emergence grows (Habel

et al., 2017; Housego et al., 2021). The results in this study and previous work (e.g., Bakhtyar et al., 2011) demonstrate that swash infiltration decreases as groundwater levels increase. Swash magnitudes on beaches with deep (or low) groundwater tables are not expected to be influenced by the groundwater level. As groundwater levels rise with the sea level, however, these beaches may reach a "tipping point" in which infiltration is sufficiently limited that the groundwater level begins to exert influence on the runup extent. For beaches with deep groundwater tables, sea level-driven increases in beach groundwater elevations will increase overland flooding potential and magnitudes through the swash–groundwater relationship.

Structural measures, such as dunes and seawalls, are increasingly utilized to protect against the impacts of SLR. However, these traditional coastal flood defenses are ineffective against groundwater rise (Rotzoll and Fletcher, 2013) and may potentially force higher groundwater levels by acting as an onshore barrier for groundwater transport (Lee et al., 2019). Ironically, these barriers may increase coastal risk by creating a (larger) groundwater overheight that will (further) amplify runup through the swash–groundwater relationship. Further research is needed to understand how coastal protection structures (including natural solutions such as beach dunes) interact with both coastal surface and subsurface flows to ensure that solutions to protect against one hazard do not exacerbate another.

5.5 Conclusions

The two-phase Eulerian model, SedOlaFlow, was used to numerically investigate the swash runup response to various periodic wave conditions and antecedent groundwater levels. Elevated antecedent groundwater levels resulted in increased runup magnitudes, most significantly for the sand (lower permeability) cases. Rapid exfiltration limits the influence of the beach groundwater table on gravel (higher permeability) beaches, whereas antecedent groundwater levels on lower permeability beaches have a sustained amplifying impact on runup under irregular waves.

A bi-directional relationship between surface and subsurface flows in the swash zone was confirmed in Delisle et al. (in revision). Here, infiltration capacity and beach face saturation are explored to quantify and understand the bi-directional feedback between swash and groundwater. Groundwater levels that exceed the offshore water elevation create a saturated beach face that both reduces infiltration capacity and diminishes beach face turbulence. In combination, these near-bed processes facilitate swash propagation further onshore. The exact contributions and relative dominance of infiltration capacity and beach face turbulence in modulating runup extent have yet to be delineated.

Idealized (e.g., constant beach slope, homogeneous sediment) numerical simulations were necessary to enable the study of complex near-bed processes, however, the results provide useful insights into the general behavior of natural beaches. Lower permeability beaches are expected to be more susceptible to regular runup amplification from elevated groundwater levels while higher permeability beaches may face a more pronounced impact during extreme events. Results suggest that larger wave heights will increase the impacts of elevated groundwater levels on runup. Various other factors may influence the swash–groundwater relationship (e.g., beach slope, wave period), however swash zone processes are often interrelated with one another and it is difficult to deconstruct the exact contributions of each component. The influence of antecedent groundwater levels on swash extent is expected to vary spatially and temporally depending on beach and wave characteristics; understanding which beaches are likely to experience increased runup (and under what conditions) due to beach groundwater interactions is important in developing effective coastal protection strategies.

Coastal hazard assessments have yet to explicitly consider surface-subsurface flow feedback impacts on wave runup and flooding. The swash–groundwater relationship may cause maximum flood vulnerability to coincide with maximum beach groundwater levels rather than high tide. Results suggest that precipitation (especially on lower permeability beaches) that saturates the beach face can temporarily and amplifying effect on runup, similar to ele-

vated groundwater levels. SLR will increase coastal groundwater levels and may cause previously unaffected beaches to become susceptible to increased runup from elevated groundwater levels. Existing coastal protection strategies (e.g., sea walls) may increase groundwater overheights and consequently amplify runup impacts. Beach groundwater impacts on wave runup warrant consideration in coastal flooding predictions.

The analysis presented in this work advances our understanding of coastal processes and provides valuable information to improve coastal vulnerability predictions. However, the numerical simulations are limited to a single beach slope, two sediment sizes, and four wave conditions. Laboratory and field experiments with high-resolution surface and subsurface data are urgently needed to validate numerical models and provide a more comprehensive understanding of the swash–groundwater relationship.

5.6 Acknowledgements

This study was partially supported by the California Department of Parks and Recreation Division of Boating and Waterways (C1670006), the US Coastal Research Program (W912HZ-20-200-004), the Barbara Streisand Foundation, and the Basic Science Research Program through the National Research Foundation of Korea (NRF) funded by the Ministry of Education (NRF-2021R1F1A1062223). Numerical simulations presented in this study were carried out using the Hoffman2 cluster at the University of California, Los Angeles. The SedOlaFlow case setup to reproduce the same results are publicly available on Zenodo: `https://doi.org/10.5281/zenodo.7946612`.

CHAPTER 6

Conclusions and future work

Improved understanding of surface–subsurface swash dynamics is fundamental to characterizing and accurately predicting wave runup, overtopping, and subsequent coastal flooding (e.g., Horn, 2002; Elko et al., 2015; Gallien, 2016; Housego et al., 2021). Previous swash zone research efforts are restricted to surface flows, accounting only for the uni-directional influence of surface flows on beach groundwater behavior, and/or rely on restrictive assumptions and simplifications that prohibit a detailed understanding of swash zone surface-subsurface interactions. The aim of this dissertation is to address a fundamental knowledge gap of how beach groundwater dynamics influence swash flows (i.e., runup, overtopping) and the implications for coastal vulnerability.

A foundation for future model development is built by numerically investigating sheet flow driven by a near-breaking transient wave using SedFoam, a two-phase Eulerian sediment transport model in the OpenFOAM framework. Compared with large-scale wave flume data, good agreements are obtained for streamwise flow velocity profiles, sediment concentration profiles, and the sheet flow layer thickness. Model results show near-bed velocity and sediment profile evolution within the sheet flow layer. Intense sediment suspension trailing the wave crest generates stable density stratification that dampens near-bed turbulent kinetic energy and contributes to decreasing bed shear stress. Results suggest that the buoyant flux dominates turbulent kinetic energy dissipation after the passing of the wave crest, coinciding with the reduction of bed shear stress. The instantaneous upper bound of the sheet flow layer exists in different log-law regimes under the transient wave, giving rise to a near-bed

velocity profile that is highly dependent on the variable sheet flow layer wall unit. The effect of the profile shape parameter on bedload sediment transport is studied where the bedload predicted using the time-varying optimal profile shape parameter yields good agreement compared to the directly modeled bedload. Modeled sediment transport rates demonstrate that reduced bed shear stress caused by density stratification limits bedload and results in a suspended load-dominant mode.

A numerical modeling strategy is developed that simultaneously resolves free surface and porous media flow for a variably saturated subsurface. The novel numerical model, SedOlaFlow, is developed by merging the existing two-phase, Eulerian sediment transport model, SedWaveFoam (Kim et al., 2018), with the surface wave solver, olaFlow (Higuera et al., 2014). SedOlaFlow is validated with large wave flume surface and subsurface data for dam-break driven swash over permeable gravel and sand beaches. Sediment size significantly impacts swash infiltration/exfiltration, subsurface flow, and the swash-groundwater relationship. Model results demonstrate that vertical infiltration into the upper unsaturated beach leads to a delayed groundwater table response to swash in the sand beach. Pressure fluctuations in the sand beach are not directly indicative of the swash depth or groundwater table and exfiltration may occur even when the swash depth is non-zero. Groundwater circulation is non-uniform and highly dynamic in the variably saturated vadose zone. Antecedent groundwater levels are found to impact swash extent and duration, confirming a bi-directional relationship between swash and groundwater flows.

The swash response to various beach characteristics, periodic wave conditions, and antecedent groundwater levels is further investigated using SedOlaFlow. Elevated antecedent groundwater levels increase swash extent, with a more pronounced impact on lower permeability beaches. Infiltration capacity and beach face turbulence are explored as potential mechanisms for the bi-directional feedback between swash and beach groundwater flows. Heightened antecedent groundwater levels are found to (1) create a saturated beach face that (2) reduces infiltration capacity and turbulence which (3) causes runup to travel further

distances. The model results are extended to natural beaches to explore how the swash–groundwater relationship varies with beach and wave conditions. Potential implications on coastal vulnerability are discussed, particularly with regards to temporal dynamics, environmental factors, and sea level rise (SLR). The analysis suggests that coastal hazard planning and modeling that neglect the influence of beach groundwater on swash surface flows may be mistiming and under-predicting coastal risk.

A paucity of laboratory and in-situ observations with simultaneous surface and subsurface flow measurements has limited an understanding of the swash–groundwater relationship. High-resolution flume and field observations are necessary to validate numerical models and advance coastal hazard planning. Laboratory experiments with idealized conditions will enable the contributions of individual factors (e.g., beach slope, wave height, permeability) to the swash–groundwater relationship to be distinguished. Field campaigns will be immensely beneficial in determining the impacts of swash–groundwater dynamics on coastal vulnerability, especially with regards to conditions not currently replicable in a laboratory setting (e.g., water-backed beaches).

SedOlaFlow is an important step in integrating surface and subsurface physics into a single numerical model. Further development should be aimed at increasing applicability to natural scenarios by including sediment mobility, heterogeneous beaches, and variable-density flows for example. The integration of hydrological forcings (e.g., rain) and structures (e.g., seawall) into SedOlaFlow will enable more detailed investigations of compound hazards. Coastal flooding predictions would be improved by incorporating the swash–groundwater relationship into modeling. Given current computational demands, however, it is not currently feasible to used RANS-based, VOF models like SedOlaFlow to model at large (> 100 m) scales. Future research should aim to parameterize the swash–groundwater relationship for inclusion in reduced-complexity models (e.g., XBeach, Delft-3D).

References

Abboud, J., Ryan, M., Osborn, G., 2018. Groundwater flooding in a river-connected alluvial aquifer. Journal of Flood Risk Management 11, e12334. doi:10.1111/jfr3.12334.

Almar, R., Ranasinghe, R., Bergsma, E.W., Diaz, H., Melet, A., Papa, F., Vousdoukas, M., Athanasiou, P., Dada, O., Almeida, L.P., et al., 2021. A global analysis of extreme coastal water levels with implications for potential coastal overtopping. Nature communications 12, 1–9. doi:10.1038/s41467-021-24008-9.

Amoudry, L., Hsu, T.J., Liu, P.L.F., 2008. Two-phase model for sand transport in sheet flow regime. Journal of Geophysical Research: Oceans 113, C03011. doi:10.1029/2007JC004179.

Anarde, K., Figlus, J., Sous, D., Tissier, M., 2020. Transformation of infragravity waves during hurricane overwash. Journal of Marine Science and Engineering 8, 545. doi:10.3390/jmse8080545.

Anderson, D., Cox, D., Mieras, R., Puleo, J.A., Hsu, T.J., 2017. Observations of wave-induced pore pressure gradients and bed level response on a surf zone sandbar. Journal of Geophysical Research: Oceans 122, 5169–5193. doi:10.1002/2016JC012557.

Arns, A., Dangendorf, S., Jensen, J., Talke, S., Bender, J., Pattiaratchi, C., 2017. Sea-level rise induced amplification of coastal protection design heights. Scientific reports 7, 40171. doi:10.1038/srep40171.

Austin, M.J., Masselink, G., 2006a. Observations of morphological change and sediment transport on a steep gravel beach. Marine Geology 229, 59–77. doi:0.1016/j.margeo.2006.02.003.

Austin, M.J., Masselink, G., 2006b. Swash–groundwater interaction on a steep gravel beach. Continental Shelf Research 26, 2503–2519. doi:10.1016/j.csr.2006.07.031.

Bagnold, R.A., 1940. Beach formation by waves; some model experiments in a wave tank. Journal of the Institution of Civil Engineers 15, 27–52.

Bagnold, R.A., 1954. Experiments on a gravity-free dispersion of large solid spheres in a newtonian fluid under shear. Proceedings of the Royal Society of London. Series A, Mathematical and Physical Sciences 225, 49–63. doi:10.1098/rspa.1954.0186.

Bagnold, R.A., 1956. The flow of cohesionless grains in fluids. Philosophical Transactions of the Royal Society of London. Series A, Mathematical and Physical Sciences 249, 235–297. doi:10.1098/rsta.1956.0020.

Bailard, J.A., 1981. An energetics total load sediment transport model for a plane sloping beach. Journal of Geophysical Research: Oceans 86, 10938–10954. doi:10.1029/JC086iC11p10938.

Baird, A.J., Mason, T., Horn, D.P., 1998. Validation of a boussinesq model of beach ground water behaviour. Marine Geology 148, 55–69. doi:10.1016/S0025-3227(98)00026-7.

Bakhtyar, R., Barry, D.A., Yeganeh-Bakhtiary, A., Ghaheri, A., 2009. Numerical simulation of surf–swash zone motions and turbulent flow. Advances in Water Resources 32, 250–263. doi:10.1016/j.advwatres.2008.11.004.

Bakhtyar, R., Brovelli, A., Barry, D.A., Li, L., 2011. Wave-induced water table fluctuations, sediment transport and beach profile change: Modeling and comparison with large-scale laboratory experiments. Coastal Engineering 58, 103–118. doi:10.1016/j.coastaleng.2010.08.004.

Balachandar, S., Eaton, J.K., 2010. Turbulent dispersed multiphase flow. Annual review of fluid mechanics 42, 111–133. doi:10.1146/annurev.fluid.010908.165243.

Baldock, T., Cox, D., Maddux, T., Killian, J., Fayler, L., 2009. Kinematics of breaking

tsunami wavefronts: A data set from large scale laboratory experiments. Coastal Engineering 56, 506–516. doi:10.1016/j.coastaleng.2008.10.011.

Baldock, T., Holmes, P., 1999. Seepage effects on sediment transport by waves and currents, in: Coastal Engineering 1998, pp. 3601–3614. doi:10.1061/9780784404119.274.

Barry, D.A., Barry, S., Parlange, J.Y., 1996. Capillarity correction to periodic solutions of the shallow flow approximation. Technical Report. American Geophysical Union. doi:10.1029/CE050p0496.

Befus, K., Barnard, P.L., Hoover, D.J., Finzi Hart, J., Voss, C.I., 2020. Increasing threat of coastal groundwater hazards from sea-level rise in california. Nature Climate Change 10, 946–952. doi:10.1038/s41558-020-0874-1.

Beji, S., Nadaoka, K., 1996. A formal derivation and numerical modelling of the improved boussinesq equations for varying depth. Ocean Engineering 23, 691–704. doi:10.1016/0029-8018(96)84408-8.

Berberović, E., van Hinsberg, N.P., Jakirlić, S., Roisman, I.V., Tropea, C., 2009. Drop impact onto a liquid layer of finite thickness: Dynamics of the cavity evolution. Physical Review E 79, 036306. doi:10.1103/PhysRevE.79.036306.

Bjerklie, D.M., Mullaney, J.R., Stone, J.R., Skinner, B.J., Ramlow, M.A., 2012. Preliminary investigation of the effects of sea-level rise on groundwater levels in New Haven, Connecticut. Technical Report. US Geological Survey.

Briganti, R., Torres-Freyermuth, A., Baldock, T.E., Brocchini, M., Dodd, N., Hsu, T.J., Jiang, Z., Kim, Y., Pintado-Patiño, J.C., Postacchini, M., 2016. Advances in numerical modelling of swash zone dynamics. Coastal Engineering 115, 26–41. doi:10.1016/j.coastaleng.2016.05.001.

Brocchini, M., Dodd, N., 2008. Nonlinear shallow water equation modeling for coastal engineering. Journal of waterway, port, coastal, and ocean engineering 134, 104–120. doi:10.1061/(ASCE)0733-950X(2008)134:2(104).

Brown, J.D., Spencer, T., Moeller, I., 2007. Modeling storm surge flooding of an urban area with particular reference to modeling uncertainties: A case study of canvey island, united kingdom. Water Resources Research 43. doi:10.1029/2005WR004597.

Butt, T., Russell, P., Turner, I., 2001. The influence of swash infiltration–exfiltration on beach face sediment transport: onshore or offshore? Coastal Engineering 42, 35–52. doi:10.1016/S0378-3839(00)00046-6.

Carnahan, N.F., Starling, K.E., 1969. Equation of state for nonattracting rigid spheres. The Journal of chemical physics 51, 635–636. doi:10.1063/1.1672048.

Cayan, D.R., Bromirski, P.D., Hayhoe, K., Tyree, M., Dettinger, M.D., Flick, R.E., 2008. Climate change projections of sea level extremes along the california coast. Climatic Change 87, 57–73. doi:10.1007/s10584-007-9376-7.

Census, U., 2015b. Pacific population table. US Census Bureau.

Chardón-Maldonado, P., Pintado-Patiño, J.C., Puleo, J.A., 2016. Advances in swash-zone research: Small-scale hydrodynamic and sediment transport processes. Coastal Engineering 115, 8–25. doi:10.1016/j.coastaleng.2015.10.008.

Chauchat, J., 2018. A comprehensive two-phase flow model for unidirectional sheet-flows. Journal of Hydraulic Research 56, 15–28. doi:10.1080/00221686.2017.1289260.

Chauchat, J., Cheng, Z., Nagel, T., Bonamy, C., Hsu, T.J., 2017. Sedfoam-2.0: a 3-d two-phase flow numerical model for sediment transport. Geoscientific Model Development 10, 4367–4392. doi:10.5194/gmd-10-4367-2017.

Chen, C., Wood, P., 1985. A turbulence closure model for dilute gas-particle flows. The Canadian Journal of Chemical Engineering 63, 349–360. doi:10.1002/cjce.5450630301.

Chen, L., Zang, J., Hillis, A.J., Morgan, G.C., Plummer, A.R., 2014. Numerical investigation of wave–structure interaction using openfoam. Ocean Engineering 88, 91–109. doi:10.1016/j.oceaneng.2014.06.003.

Cheng, Z., Hsu, T.J., Calantoni, J., 2017. Sedfoam: A multi-dimensional eulerian two-phase model for sediment transport and its application to momentary bed failure. Coastal Engineering 119, 32–50. doi:10.1016/j.coastaleng.2016.08.007.

Christensen, E.D., Deigaard, R., 2001. Large eddy simulation of breaking waves. Coastal engineering 42, 53–86. doi:10.1016/S0378-3839(00)00049-1.

Church, J.A., Clark, P.U., Cazenave, A., Gregory, J.M., Jevrejeva, S., Levermann, A., Merrifield, M.A., Milne, G.A., Nerem, R.S., Nunn, P.D., Payne, A.J., Pfeffer, W.T., Stammer, D., Unnikrishnan, A.S., 2013. Sea level change. In: Climate Change 2013: The Physical Science Basis. Contribution of Working Group I to the Fifth Assessment Report of the Intergovernmental Panel on Climate Change [Stocker, T.F., D. Qin, G.-K. Plattner, M. Tignor, S.K. Allen, J. Boschung, A. Nauels, Y. Xia, V. Bex and P.M. Midgley (eds.)] .

Conley, D.C., Inman, D.L., 1994. Ventilated oscillatory boundary layers. Journal of Fluid Mechanics 273, 261–284. doi:10.1017/S002211209400193X.

Cowen, E.A., Mei Sou, I., Liu, P.L.F., Raubenheimer, B., 2003. Particle image velocimetry measurements within a laboratory-generated swash zone. Journal of Engineering Mechanics 129, 1119–1129. doi:10.1061/(ASCE)0733-9399(2003)129:10(1119).

Crossett, K., Ache, B., Pacheco, P., Haber, K., 2013. National coastal population report, population trends from 1970 to 2020. NOAA State of the Coast Report Series, US Department of Commerce, Washington .

Dalinghaus, C., Coco, G., Higuera, P., 2022. A predictive equation for wave setup using genetic programming. Natural Hazards and Earth System Sciences Discussions , 1–20doi:10.5194/nhess-2022-221.

Dally, W.R., Dean, R.G., 1984. Suspended sediment transport and beach profile evolution. Journal of Waterway, Port, Coastal, and Ocean Engineering 110, 15–33. doi:10.1061/(ASCE)0733-950X(1984)110:1(15).

Dalrymple, R.A., Rogers, B., 2006. Numerical modeling of water waves with the sph method. Coastal engineering 53, 141–147. doi:10.1016/j.coastaleng.2005.10.004.

Dalya, C.J., Floc'h, F., Almeida, L.P., Almara, R., Jaud, M., 2021. Morphodynamic modelling of beach cusp formation: the role of wave forcing and sediment composition. Geomorphology , 107798doi:10.1016/j.geomorph.2021.107798.

Danon, H., Wolfshtein, M., Hetsroni, G., 1977. Numerical calculations of two-phase turbulent round jet. International Journal of Multiphase Flow 3, 223–234. doi:10.1016/0301-9322(77)90002-7.

Delisle, M.P.C., Kim, Y., Gallien, T.W., in revision. A numerical study of dam-break driven swash and beach groundwater interactions. Journal of Geophysical Research: Oceans .

Delisle, M.P.C., Kim, Y., Mieras, R.S., Gallien, T.W., 2022. Numerical investigation of sheet flow driven by a near-breaking transient wave using sedfoam. European Journal of Mechanics-B/Fluids 96, 51–64. doi:10.1016/j.euromechflu.2022.07.002.

Desombre, J., Morichon, D., Mory, M., 2012. Simultaneous surface and subsurface air and water flows modelling in the swash zone. Coastal Engineering Proceedings , 56–56doi:10.9753/icce.v33.currents.56.

Dibajnia, M., Watanabe, A., 1992. Sheet flow under nonlinear waves and currents, in: Pro-

ceedings of the 23rd International Conference on Coastal Engineering, American Society of Civil Engineers. pp. 2015–2028. doi:10.1061/9780872629332.154.

Dinehart, R.L., 1992. Evolution of coarse gravel bed forms: Field measurements at flood stage. Water Resources Research 28, 2667–2689. doi:doi.org/10.1029/92WR01357.

Ding, J., Gidaspow, D., 1990. A bubbling fluidization model using kinetic theory of granular flow. AIChE Journal 36, 523–538. doi:doi.org/10.1002/aic.690360404.

Dingler, J.R., Inman, D.L., 1976. Wave-formed ripples in nearshore sands, in: Proceedings of the 15th International Conference on Coastal Engineering, American Society of Civil Engineers. pp. 2109–2126. doi:10.1061/9780872620834.123.

Dodd, N., 1998. Numerical model of wave run-up, overtopping, and regeneration. Journal of Waterway, Port, Coastal, and Ocean Engineering 124, 73–81. doi:10.1061/(ASCE)0733-950X(1998)124:2(73).

Dohmen-Janssen, C., Hassan, W., Ribberink, J., 2001. Mobile-bed effects in oscillatory sheet flow. Journal of Geophysical Research: Oceans 106, 27103–27115. doi:doi.org/10.1029/2000JC000513.

Dohmen-Janssen, C.M., Hanes, D.M., 2002. Sheet flow dynamics under monochromatic nonbreaking waves. Journal of Geophysical Research: Oceans 107, 3149. doi:doi.org/10.1029/2001JC001045.

Dohmen-Janssen, C.M., Hanes, D.M., 2005. Sheet flow and suspended sediment due to wave groups in a large wave flume. Continental Shelf Research 25, 333–347. doi:doi.org/10.1016/j.csr.2004.10.009.

Dohmen-Janssen, C.M., Kroekenstoel, D.F., Hassan, W.N., Ribberink, J.S., 2002. Phase lags in oscillatory sheet flow: experiments and bed load modelling. Coastal Engineering 46, 61–87. doi:10.1016/S0378-3839(02)00056-X.

Dominick, T.F., Wilkins Jr, B., Roberts, H., 1971. Mathematical model for beach groundwater fluctuations. Water Resources Research 7, 1626–1635. doi:10.1029/WR007i006p01626.

Dong, P., Zhang, K., 1999. Two-phase flow modelling of sediment motions in oscillatory sheet flow. Coastal Engineering 36, 87–109. doi:10.1016/S0378-3839(98)00052-0.

Drake, T.G., Calantoni, J., 2001. Discrete particle model for sheet flow sediment transport in the nearshore. Journal of Geophysical Research: Oceans 106, 19859–19868. doi:10.1029/2000JC000611.

Drew, D.A., 1983. Mathematical modeling of two-phase flow. Annual review of fluid mechanics 15, 261–291. doi:10.1146/annurev.fl.15.010183.001401.

Duncan, J.R., 1964. The effects of water table and tide cycle on swash-backwash sediment distribution and beach profile development. Marine Geology 2, 186–197. doi:10.1016/0025-3227(64)90039-8.

Egan, G., Manning, A.J., Chang, G., Fringer, O., Monismith, S., 2020. Sediment-induced stratification in an estuarine bottom boundary layer. Journal of Geophysical Research: Oceans 125, e2019JC016022. doi:10.1029/2019JC016022.

Einstein, H.A., 1950. The bed-load function for sediment transportation in open channel flows. Technical Report No. 126. US Department of Agriculture, Soil Conservation Service.

Elfrink, B., Baldock, T., 2002. Hydrodynamics and sediment transport in the swash zone: a review and perspectives. Coastal Engineering 45, 149–167. doi:10.1016/S0378-3839(02)00032-7.

Elko, N., Dietrich, C., Cialone, M., Stockdon, H., Bilskie, M.W., Boyd, B., Charbonneau, B., Cox, D., Dresback, K., Elgar, S., et al., 2019. Advancing the understanding of storm processes and impacts. Shore Beach 87, 37–51.

Elko, N., Feddersen, F., Foster, D., Hapke, C., McNinch, J., Mulligan, R., Ozkan-Haller, H.T., Plant, N., Raubenheimer, B., 2015. The future of nearshore processes research. Shore Beach 83, 13.

Elsayed, S.M., Oumeraci, H., 2016. Combined modelling of coastal barrier breaching and induced flood propagation using xbeach. Hydrology 3, 32. doi:10.3390/hydrology3040032.

Engelund, F., Hansen, E., 1967. A monograph on sediment transport in alluvial streams. Technical University of Denmark Ostervoldgade 10, Copenhagen K .

Faria, A.G., Thornton, E., Stanton, T., 1996. Small-scale morphology related to wave and current parameters over a barred beach, in: Proceedings of the 25th International Conference on Coastal Engineering, pp. 3391–3404. doi:10.1061/9780784402429.262.

Ferry, J., Balachandar, S., 2001. A fast eulerian method for disperse two-phase flow. International journal of multiphase flow 27, 1199–1226. doi:10.1016/S0301-9322(00)00069-0.

Ferry, J., Rani, S.L., Balachandar, S., 2003. A locally implicit improvement of the equilibrium eulerian method. International journal of multiphase flow 29, 869–891. doi:10.1016/S0301-9322(03)00064-8.

Fiedler, J.W., Smit, P.B., Brodie, K.L., McNinch, J., Guza, R.T., 2018. Numerical modeling of wave runup on steep and mildly sloping natural beaches. Coastal Engineering 131, 106–113. doi:10.1016/j.coastaleng.2017.09.004.

FitzGerald, D.M., Fenster, M.S., Argow, B.A., Buynevich, I.V., 2008. Coastal impacts due to sea-level rise. Annu. Rev. Earth Planet. Sci. 36, 601–647. doi:10.1146/annurev.earth.35.031306.140139.

Flores, N.Z., Sleath, J.F., 1998. Mobile layer in oscillatory sheet flow. Journal of Geophysical Research: Oceans 103, 12783–12793. doi:10.1029/98JC00691.

Foster, D., Bowen, A., Holman, R.A., Natoo, P., 2006. Field evidence of pressure gradient induced incipient motion. Journal of Geophysical Research: Oceans 111. doi:10.1029/2004JC002863.

Fox-Kemper, B., Kewitt, H.T., Xiao, C., Aoalgeirsdottir, G., Driffhout, S.S., Edwards, T.L., Golledge, N.R., Hemer, M., Kopp, R.E., Krinner, G., Mix, A., Notz, D., Nowicki, S., Nurhati, I.S., Ruiz, L., Sallee, J.B., Slangen, A.B.A., Yu, Y., 2021. Ocean, cryosphere and sea level change. In: Climate Change 2021: The Physical Science Basis. Contribution of Working Group I to the Sixth Assessment Report of the Intergovernmental Panel on Climate Change [Masson-Delmotte, V., P. Zhai, A. Pirani, S. L. Conners, C. Pean, S. Berger, N. Caud, Y. Chen, L. Goldfarb, M. I. Gomis, M. Huang, K. Leitzell, E. Lonnoy, J. B. R. Matthews, T. K. Maycock, T. Waterfield, O. Yelekci, R. Yu and B. Zhou (eds.)] , 1211–1362.

Fredsøe, J., Sumer, B.M., Kozakiewicz, A., Chua, L.H., Deigaard, R., 2003. Effect of externally generated turbulence on wave boundary layer. Coastal Engineering 49, 155–183. doi:10.1016/S0378-3839(03)00032-2.

Gallagher, E.L., Elgar, S., Guza, R., 1998. Observations of sand bar evolution on a natural beach. Journal of Geophysical Research: Oceans 103, 3203–3215. doi:doi.org/10.1029/97JC02765.

Gallien, T.W., 2016. Validated coastal flood modeling at imperial beach, california: Comparing total water level, empirical and numerical overtopping methodologies. Coastal Engineering 111, 95–104. doi:10.1016/j.coastaleng.2016.01.014.

Gallien, T.W., Sanders, B., Flick, R., 2014. Urban coastal flood prediction: Integrating wave overtopping, flood defenses and drainage. Coastal Engineering 91, 18–28. doi:10.1016/j.coastaleng.2014.04.007.

Geyer, W.R., Smith, J.D., 1987. Shear instability in a highly stratified estuary. Journal of Physical Oceanography 17, 1668–1679. doi:10.1175/1520-0485(1987)017<1668:SIIAHS>2.0.CO;2.

Gidaspow, D., 1994. Multiphase flow and fluidization: continuum and kinetic theory descriptions. Academic press.

Gillham, R., 1984. The capillary fringe and its effect on water-table response. Journal of Hydrology 67, 307–324. doi:10.1016/0022-1694(84)90248-8.

Gonzalez-Rodriguez, D., Madsen, O.S., 2007. Seabed shear stress and bedload transport due to asymmetric and skewed waves. Coastal Engineering 54, 914–929. doi:10.1016/j.coastaleng.2007.06.004.

Gourlay, M.R., 1992. Wave set-up, wave run-up and beach water table: Interaction between surf zone hydraulics and groundwater hydraulics. Coastal Engineering 17, 93–144. doi:10.1016/0378-3839(92)90015-M.

Green, W.H., Ampt, G., 1911. Studies on soil phyics. The Journal of Agricultural Science 4, 1–24. doi:0.1017/S0021859600001441.

Griggs, G., Reguero, B.G., 2021. Coastal adaptation to climate change and sea-level rise. Water 13, 2151. doi:10.3390/w13162151.

Guo, W., Langevin, C.D., 2002. User's guide to SEAWAT; a computer program for simulation of three-dimensional variable-density ground-water flow. Technical Report. U.S. Geological Survey.

Habel, S., Fletcher, C.H., Rotzoll, K., El-Kadi, A.I., 2017. Development of a model to simulate groundwater inundation induced by sea-level rise and high tides in honolulu, hawaii. Water research 114, 122–134. doi:10.1016/j.watres.2017.02.035.

Harrison, W., 1969. Empirical equations for foreshore changes over a tidal cycle. Marine Geology 7, 529–551. doi:10.1016/0025-3227(69)90022-X.

Hauer, M.E., Evans, J.M., Mishra, D.R., 2016. Millions projected to be at risk from sea-level rise in the continental united states. Nature Climate Change 6, 691–695. doi:10.1038/nclimate2961.

Heberger, M., Cooley, H., Herrera, P., Gleick, P.H., Moore, E., 2009. The impacts of sea-level rise on the California coast. Technical Report. California Climate Change Center.

Hegge, B.J., Masselink, G., 1991. Groundwater-table responses to wave run-up: an experimental study from western australia. Journal of Coastal Research , 623–634.

Heiss, J.W., Puleo, J.A., Ullman, W.J., Michael, H.A., 2015. Coupled surface-subsurface hydrologic measurements reveal infiltration, recharge, and discharge dynamics across the swash zone of a sandy beach. Water Resources Research 51, 8834–8853. doi:10.1002/2015WR017395.

Heiss, J.W., Ullman, W.J., Michael, H.A., 2014. Swash zone moisture dynamics and unsaturated infiltration in two sandy beach aquifers. Estuarine, Coastal and Shelf Science 143, 20–31. doi:10.1016/j.ecss.2014.03.015.

Henderson, S.M., Allen, J.S., Newberger, P., 2004. Nearshore sandbar migration predicted by an eddy-diffusive boundary layer model. Journal of Geophysical Research: Oceans 109. doi:10.1029/2003JC002137.

Hibberd, S., Peregrine, D., 1979. Surf and run-up on a beach: a uniform bore. Journal of Fluid Mechanics 95, 323–345. doi:10.1017/S002211207900149X.

Higuera, P., Lara, J.L., Losada, I.J., 2013. Realistic wave generation and active wave absorption for navier–stokes models: Application to openfoam®. Coastal Engineering 71, 102–118. doi:10.1016/j.coastaleng.2012.07.002.

Higuera, P., Lara, J.L., Losada, I.J., 2014. Three-dimensional interaction of waves and porous coastal structures using openfoam®. part i: Formulation and validation. Coastal Engineering 83, 243–258.

Hirt, C.W., Nichols, B.D., 1981. Volume of fluid (vof) method for the dynamics of free boundaries. Journal of computational physics 39, 201–225. doi:10.1016/0021-9991(81)90145-5.

Hoefel, F., Elgar, S., 2003. Wave-induced sediment transport and sandbar migration. Science 299, 1885–1887. doi:10.1126/science.1081448.

Hoggart, S., Hanley, M., Parker, D.J., Simmonds, D., Bilton, D., Filipova-Marinova, M., Franklin, E., Kotsev, I., Penning-Rowsell, E.C., Rundle, S., et al., 2014. The consequences of doing nothing: The effects of seawater flooding on coastal zones. Coastal Engineering 87, 169–182. doi:10.1016/j.coastaleng.2013.12.001.

Hoover, D.J., Odigie, K.O., Swarzenski, P.W., Barnard, P., 2017. Sea-level rise and coastal groundwater inundation and shoaling at select sites in california, usa. Journal of Hydrology: Regional Studies 11, 234–249. doi:10.1016/j.ejrh.2015.12.055.

Horn, D., Li, L., 2006. Measurement and modelling of gravel beach groundwater response to wave run-up: effects on beach profile changes. Journal of Coastal Research 22, 1241–1249. doi:10.2112/06A-0006.1.

Horn, D.P., 2002. Beach groundwater dynamics. Geomorphology 48, 121–146. doi:10.1016/S0169-555X(02)00178-2.

Horn, D.P., 2006. Measurements and modelling of beach groundwater flow in the swash-zone: a review. Continental Shelf Research 26, 622–652. doi:10.1016/j.csr.2006.02.001.

Housego, R., Raubenheimer, B., Elgar, S., Cross, S., Legner, C., Ryan, D., 2021. Coastal

flooding generated by ocean wave-and surge-driven groundwater fluctuations on a sandy barrier island. Journal of Hydrology 603, 126920. doi:10.1016/j.jhydrol.2021.126920.

Hsu, T.J., Elgar, S., Guza, R., 2006. Wave-induced sediment transport and onshore sandbar migration. Coastal Engineering 53, 817–824. doi:10.1016/j.coastaleng.2006.04.003.

Hsu, T.J., Jenkins, J.T., Liu, P.L.F., 2004. On two-phase sediment transport: sheet flow of massive particles. Proceedings of the Royal Society of London. Series A: Mathematical, Physical and Engineering Sciences 460, 2223–2250. doi:10.1098/rspa.2003.1273.

Hsu, T.J., Sakakiyama, T., Liu, P.L.F., 2002. A numerical model for wave motions and turbulence flows in front of a composite breakwater. Coastal Engineering 46, 25–50. doi:10.1016/S0378-3839(02)00045-5.

Hsu, T.W., Shih, D.S., Li, C.Y., Lan, Y.J., Lin, Y.C., 2017. A study on coastal flooding and risk assessment under climate change in the mid-western coast of taiwan. Water 9, 390. doi:10.3390/w9060390.

Hu, K., Mingham, C.G., Causon, D.M., 2000. Numerical simulation of wave overtopping of coastal structures using the non-linear shallow water equations. Coastal engineering 41, 433–465. doi:10.1016/S0378-3839(00)00040-5.

Hubbard, M.E., Dodd, N., 2002. A 2d numerical model of wave run-up and overtopping. Coastal Engineering 47, 1–26. doi:10.1016/S0378-3839(02)00094-7.

Hughes, M., Masselink, G., Hanslow, D., Mitchell, D., 1997. Toward a better understanding of swash zone sediment transport, in: Coastal Dynamics' 97, ASCE. pp. 804–813.

Hughes, M., Turner, I., 1999. The beachface. Handbook of beach and shoreface morphodynamics , 119–144.

Hugo, G., 2011. Future demographic change and its interactions with migration and climate change. Global Environmental Change 21, S21–S33. doi:10.1016/j.gloenvcha.2011.09.008.

Hunt, J., 2005. Inland and coastal flooding: developments in prediction and prevention. Philosophical Transactions of the Royal Society of London A: Mathematical, Physical and Engineering Sciences 363, 1475–1491. doi:10.1098/rsta.2005.1580.

Hunter, J., 2012. A simple technique for estimating an allowance for uncertain sea-level rise. Climatic Change 113, 239–252. doi:10.1007/s10584-011-0332-1.

Jackson, A., 2012. A comprehensive tour of snappyhexmesh, in: 7th OpenFOAM workshop.

Jackson, N.L., Masselink, G., Nordstrom, K.F., 2004. The role of bore collapse and local shear stresses on the spatial distribution of sediment load in the uprush of an intermediate-state beach. Marine Geology 203, 109–118. doi:10.1016/S0025-3227(03)00328-1.

Jacobsen, N.G., Fuhrman, D.R., Fredsøe, J., 2012. A wave generation toolbox for the open-source cfd library: Openfoam®. International Journal for numerical methods in fluids 70, 1073–1088. doi:10.1002/fld.2726.

Jamal, M., Simmonds, D., Magar, V., 2014. Modelling gravel beach dynamics with xbeach. Coastal Engineering 89, 20–29. doi:10.1016/j.coastaleng.2014.03.006.

Jasak, H., 1996. Error analysis and estimation for the finite volume method with applications to fluid flows. Ph.D. thesis. Imperial College London (University of London).

Jenkins, J.T., Savage, S.B., 1983. A theory for the rapid flow of identical, smooth, nearly elastic, spherical particles. Journal of Fluid Mechanics 130, 187–202.

Jensen, B., Jacobsen, N.G., Christensen, E.D., 2014. Investigations on the porous media equations and resistance coefficients for coastal structures. Coastal Engineering 84, 56–72. doi:10.1016/j.coastaleng.2013.11.004.

Jensen, B., Sumer, B., Fredsøe, J., 1989. Turbulent oscillatory boundary layers at high reynolds numbers. Journal of Fluid Mechanics 206, 265–297. doi:10.1017/S0022112089002302.

Johnson, P.C., Jackson, R., 1987. Frictional–collisional constitutive relations for granular materials, with application to plane shearing. Journal of Fluid Mechanics 176, 67–93. doi:10.1017/S0022112087000570.

Kaczmarek, L., 1991. Mathematical model for oscillating sheet flow, in: EUROMECH colloquium on sand transport in rivers, estuaries and the sea. 262, pp. 197–202.

Kamphuis, J.W., 1972. Scale selection for mobile bed wave models, in: Coastal Engineering 1972, pp. 1173–1195.

Kang, H.Y., Nielsen, P., 1996. Watertable dynamics in coastal areas, in: Coastal Engineering 1996, pp. 4601–4612. doi:10.1061/9780784402429.358.

Kang, H.Y., Nielsen, P., 1997. Watertable dynamics in coastal areas, in: Coastal Engineering 1996, pp. 4601–4612. doi:10.1061/9780784402429.358.

Kang, H.Y., Nielsen, P., Hanslow, D.J., 1995. Watertable overheight due to wave runup on a sandy beach, in: Coastal Engineering 1994, pp. 2115–2124. doi:10.1061/9780784400890.154.

Kennedy, A.B., Chen, Q., Kirby, J.T., Dalrymple, R.A., 2000. Boussinesq modeling of wave transformation, breaking, and runup. i: 1d. Journal of waterway, port, coastal, and ocean engineering 126, 39–47. doi:10.1061/(ASCE)0733-950X(2000)126:1(39).

Khayyer, A., Gotoh, H., Shao, S., 2008. Corrected incompressible sph method for accurate water-surface tracking in breaking waves. Coastal Engineering 55, 236–250. doi:10.1016/j.coastaleng.2007.10.001.

Kikkert, G.A., O'Donoghue, T., Pokrajac, D., Dodd, N., 2012. Experimental study of bore-driven swash hydrodynamics on impermeable rough slopes. Coastal Engineering 60, 149–166. doi:10.1016/j.coastaleng.2011.09.006.

Kikkert, G.A., Pokrajac, D., O'Donoghue, T., Steenhauer, K., 2013. Experimental study of bore-driven swash hydrodynamics on permeable rough slopes. Coastal engineering 79, 42–56. doi:10.1016/j.coastaleng.2013.04.008.

Kim, Y., Cheng, Z., Hsu, T.J., Chauchat, J., 2018. A numerical study of sheet flow under monochromatic nonbreaking waves using a free surface resolving eulerian two-phase flow model. Journal of Geophysical Research: Oceans 123, 4693–4719. doi:10.1029/2018JC013930.

Kim, Y., Mieras, R.S., Anderson, D., Gallien, T., 2021. A numerical study of sheet flow driven by skewed-asymmetric shoaling waves using sedwavefoam. Journal of Marine Science and Engineering 9, 936. doi:10.3390/jmse9090936.

Kim, Y., Mieras, R.S., Cheng, Z., Anderson, D., Hsu, T.J., Puleo, J.A., Cox, D., 2019. A numerical study of sheet flow driven by velocity and acceleration skewed near-breaking waves on a sandbar using sedwavefoam. Coastal Engineering 152, 103526. doi:10.1016/j.coastaleng.2019.103526.

Kim, Y., Zhou, Z., Hsu, T.J., Puleo, J.A., 2017. Large eddy simulation of dam-break-driven swash on a rough-planar beach. Journal of Geophysical Research: Oceans 122, 1274–1296. doi:10.1002/2016JC012366.

Klostermann, J., Schaake, K., Schwarze, R., 2012. Numerical simulation of a single rising bubble by vof with surface compression. International Journal for Numerical Methods in Fluids 71, 960–982. doi:10.1002/fld.3692.

Kranenburg, W.M., Hsu, T.J., Ribberink, J.S., 2014. Two-phase modeling of sheet-flow

beneath waves and its dependence on grain size and streaming. Advances in water resources 72, 57–70. doi:10.1016/j.advwatres.2014.05.008.

Krieger, I.M., Dougherty, T.J., 1959. A mechanism for non-newtonian flow in suspensions of rigid spheres. Transactions of the Society of Rheology 3, 137–152. doi:10.1122/1.548848.

Kubota, S., Mizuguchi, M., Takezawa, M., 1993. Prediction of field swash and reflected wave distributions. Coastal Engineering in Japan 36, 111–131. doi:10.1080/05785634.1993.11924576.

Lanckriet, T., Puleo, J.A., Masselink, G., Turner, I.L., Conley, D., Blenkinsopp, C., Russell, P., 2014. Comprehensive field study of swash-zone processes. ii: Sheet flow sediment concentrations during quasi-steady backwash. Journal of Waterway, Port, Coastal, and Ocean Engineering 140, 29–42. doi:10.1061/(ASCE)WW.1943-5460.0000209.

Lanckriet, T., Puleo, J.A., Waite, N., 2013. A conductivity concentration profiler for sheet flow sediment transport. IEEE Journal of Oceanic Engineering 38, 55–70. doi:10.1109/JOE.2012.2222791.

Lara, J., Losada, I., Guanche, R., 2008. Wave interaction with low-mound breakwaters using a rans model. Ocean engineering 35, 1388–1400. doi:10.1016/j.oceaneng.2008.05.006.

Larson, M., Kubota, S., Erikson, L., 2004. Swash-zone sediment transport and foreshore evolution: field experiments and mathematical modeling. Marine geology 212, 61–79. doi:10.1016/j.margeo.2004.08.004.

Lee, W.D., Yoo, Y.J., Jeong, Y.M., Hur, D.S., 2019. Experimental and numerical analysis on hydraulic characteristics of coastal aquifers with seawall. Water 11, 2343. doi:10.3390/w11112343.

Li, L., Barry, D., 2000. Wave-induced beach groundwater flow. Advances in Water Resources 23, 325–337. doi:10.1016/S0309-1708(99)00032-9.

Li, L., Barry, D., Parlange, J.Y., Pattiaratchi, C., 1997. Beach water table fluctuations due to wave run-up: Capillarity effects. Water Resources Research 33, 935–945. doi:10.1029/96WR03946.

Li, L., Barry, D., Pattiaratchi, C., Masselink, G., 2002. Beachwin: modelling groundwater effects on swash sediment transport and beach profile changes. Environmental Modelling & Software 17, 313–320. doi:https://doi.org/10.1016/S1364-8152(01)00066-4.

Li, L., Barry, D.A., Parlange, J.Y., Pattiaratchi, C.B., 1999. Reply (to nielsen 1999). Water Resources Research 35, 1325–1327. doi:https://doi.org/10.1029/1998WR900025.

Lin, N., Emanuel, K., Oppenheimer, M., Vanmarcke, E., 2012. Physically based assessment of hurricane surge threat under climate change. Nature Climate Change 2, 462–467. doi:10.1038/nclimate1389.

Lin, P., Chang, K.A., Liu, P.L.F., 1999. Runup and rundown of solitary waves on sloping beaches. Journal of waterway, port, coastal, and ocean engineering 125, 247–255. doi:10.1061/(ASCE)0733-950X(1999)125:5(247).

Lin, P., Liu, P.L.F., 1998a. A numerical study of breaking waves in the surf zone. Journal of fluid mechanics 359, 239–264. doi:10.1017/S002211209700846X.

Lin, P., Liu, P.L.F., 1998b. Turbulence transport, vorticity dynamics, and solute mixing under plunging breaking waves in surf zone. Journal of Geophysical Research: Oceans 103, 15677–15694. doi:10.1029/98JC01360.

Liu, P.L.F., Lin, P., Chang, K.A., Sakakiyama, T., 1999. Numerical modeling of wave interaction with porous structures. Journal of waterway, port, coastal, and ocean engineering 125, 322–330. doi:10.1061/(ASCE)0733-950X(1999)125:6(322).

Longuet-Higgins, M.S., 1953. Mass transport in water waves. Philosophical Transactions of

the Royal Society of London. Series A, Mathematical and Physical Sciences 245, 535–581. doi:10.1098/rsta.1953.0006.

Longuet-Higgins, M.S., 1983. Wave set-up, percolation and undertow in the surf zone. Proceedings of the Royal Society of London. A. Mathematical and Physical Sciences 390, 283–291.

Ludka, B.C., Guza, R.T., O'Reilly, W., 2018. Nourishment evolution and impacts at four southern california beaches: A sand volume analysis. Coastal Engineering 136, 96–105. doi:10.1016/j.coastaleng.2018.02.003.

Lynett, P.J., 2006. Nearshore wave modeling with high-order boussinesq-type equations. Journal of waterway, port, coastal, and ocean engineering 132, 348–357. doi:10.1061/(ASCE)0733-950X(2006)132:5(348).

Madsen, O.S., 1994. Spectral wave-current bottom boundary layer flows, in: Proceedings of the 24th International Conference on Coastal Engineering, American Society of Civil Engineers. pp. 384–398. doi:10.1061/9780784400890.030.

Madsen, O.S., Grant, W.D., 1976. Quantitative description of sediment transport by waves, in: Proceedings of the 15th International Conference on Coastal Engineering, American Society of Civil Engineers. pp. 1093–1112. doi:10.1061/9780872620834.065.

Madsen, P.A., Bingham, H., Liu, H., 2002. A new boussinesq method for fully nonlinear waves from shallow to deep water. Journal of Fluid Mechanics 462, 1–30. doi:10.1017/S0022112002008467.

Madsen, P.A., Murray, R., Sørensen, O.R., 1991. A new form of the boussinesq equations with improved linear dispersion characteristics. Coastal engineering 15, 371–388. doi:10.1016/0378-3839(91)90017-B.

Madsen, P.A., Sørensen, O., Schäffer, H., 1997. Surf zone dynamics simulated by a boussinesq type model. part ii: Surf beat and swash oscillations for wave groups and irregular waves. Coastal Engineering 32, 289–319. doi:10.1016/S0378-3839(97)00029-X.

Martin, C.S., Aral, M.M., 1971. Seepage force on interfacial bed particles. Journal of the Hydraulics Division 97, 1081–1100. doi:10.1061/JYCEAJ.0003016.

Masselink, G., Hughes, M., 1998. Field investigation of sediment transport in the swash zone. Continental Shelf Research 18, 1179–1199. doi:10.1016/S0278-4343(98)00027-2.

Masselink, G., Li, L., 2001. The role of swash infiltration in determining the beachface gradient: a numerical study. Marine Geology 176, 139–156. doi:10.1016/S0025-3227(01)00161-X.

Masselink, G., Turner, I., 2012. Large-scale laboratory investigation into the effect of varying back-barrier lagoon water levels on gravel beach morphology and swash zone sediment transport. Coastal Engineering 63, 23–38. doi:10.1016/j.coastaleng.2011.12.007.

Mastrandrea, M.D., Luers, A.L., 2012. Climate change in california: scenarios and approaches for adaptation. Climatic Change 111, 5–16. doi:10.1007/s10584-011-0240-4.

Mathieu, A., Chauchat, J., Bonamy, C., Nagel, T., 2019. Two-phase flow simulation of tunnel and lee-wake erosion of scour below a submarine pipeline. Water 11, 1727. doi:10.3390/w11081727.

McCall, R.T., De Vries, J.V.T., Plant, N., Van Dongeren, A., Roelvink, J., Thompson, D., Reniers, A., 2010. Two-dimensional time dependent hurricane overwash and erosion modeling at santa rosa island. Coastal Engineering 57, 668–683. doi:10.1016/j.coastaleng.2010.02.006.

McCall, R.T., Masselink, G., Roelvink, D., Russell, P., Davidson, M., Poate, T., 2012.

Modelling overwash and infiltration on gravel barriers. Coastal Engineering Proceedings 1, 34. doi:10.9753/icce.v33.currents.34.

McGranahan, G., Balk, D., Anderson, B., 2007. The rising tide: assessing the risks of climate change and human settlements in low elevation coastal zones. Environment and urbanization 19, 17–37. doi:10.1177/0956247807076960.

Merkens, J.L., Reimann, L., Hinkel, J., Vafeidis, A.T., 2016. Gridded population projections for the coastal zone under the shared socioeconomic pathways. Global and Planetary Change 145, 57–66. doi:10.1016/j.gloplacha.2016.08.009.

Mieras, R.S., Puleo, J., Cox, D., Hsu, T.J., 2018. Sandbar sediment transport. doi:10.17603/DS2BW9W.

Mieras, R.S., Puleo, J.A., Anderson, D., Cox, D.T., Hsu, T.J., 2017. Large-scale experimental observations of sheet flow on a sandbar under skewed-asymmetric waves. Journal of Geophysical Research: Oceans 122, 5022–5045. doi:doi.org/10.1002/2016JC012438.

Mieras, R.S., Puleo, J.A., Anderson, D., Hsu, T.J., Cox, D.T., Calantoni, J., 2019. Relative contributions of bed load and suspended load to sediment transport under skewed-asymmetric waves on a sandbar crest. Journal of Geophysical Research: Oceans 124, 1294–1321. doi:10.1029/2018JC014564.

Miles, J.W., 1961. On the stability of heterogeneous shear flows. Journal of Fluid Mechanics 10, 496–508.

Miller, J.L., Gardner, L., 1981. Sheet flow in a salt-marsh basin, north inlet, south carolina. Estuaries 4, 234–237. doi:10.2307/1351482.

Morris, S., Cobby, D., Parkes, A., 2007. Towards groundwater flood risk mapping. Quarterly Journal of Engineering Geology and Hydrogeology 40, 203–211. doi:10.1144/1470-9236/05-035.

Nadaoka, K., Yagi, H., 1991. Single-phase fluid modelling of sheet-flow toward the development of "numerical mobile bed", in: Proceedings of the 22nd International Conference on Coastal Engineering, American Society of Civil Engineers. pp. 2346–2359. doi:10.1061/9780872627765.179.

Nagel, T., Chauchat, J., Bonamy, C., Liu, X., Cheng, Z., Hsu, T.J., 2020. Three-dimensional scour simulations with a two-phase flow model. Advances in Water Resources 138, 103544. doi:10.1016/j.advwatres.2020.103544.

Neumann, B., Vafeidis, A.T., Zimmermann, J., Nicholls, R.J., 2015. Future coastal population growth and exposure to sea-level rise and coastal flooding-a global assessment. PloS one 10, e0118571. doi:10.1371/journal.pone.0118571.

Nicholls, R.J., 2004. Coastal flooding and wetland loss in the 21st century: changes under the sres climate and socio-economic scenarios. Global Environmental Change 14, 69–86. doi:10.1016/j.gloenvcha.2003.10.007.

Nielsen, P., 1988. Wave setup and the water table in sandy beaches. Public Works Department, Coastal Branch.

Nielsen, P., 1990. Tidal dynamics of the water table in beaches. Water resources research 26, 2127–2134. doi:10.1029/WR026i009p02127.

Nielsen, P., 1992. Coastal bottom boundary layers and sediment transport. volume 4. World Scientific.

Nielsen, P., 2006. Sheet flow sediment transport under waves with acceleration skewness and boundary layer streaming. Coastal Engineering 53, 749–758. doi:10.1016/j.coastaleng.2006.03.006.

Nielsen, P., Aseervatham, R., Fenton, J.D., Perrochet, P., 1997. Groundwater waves in

aquifers of intermediate depths. Advances in Water Resources 20, 37–43. doi:10.1016/S0309-1708(96)00015-2.

Nielsen, P., Callaghan, D.P., 2003. Shear stress and sediment transport calculations for sheet flow under waves. Coastal Engineering 47, 347–354. doi:10.1016/S0378-3839(02)00141-2.

Nielsen, P., Perrochet, P., 2000. Watertable dynamics under capillary fringes: experiments and modelling. Advances in Water Resources 23, 503–515. doi:10.1016/S0309-1708(99)00038-X.

Nielsen, P., Robert, S., Møller-Christiansen, B., Oliva, P., 2001. Infiltration effects on sediment mobility under waves. Coastal Engineering 42, 105–114. doi:10.1016/S0378-3839(00)00051-X.

Noda, E.K., 1972. Equilibrium beach profile scale-model relationship. Journal of the Waterways, Harbors and Coastal Engineering Division 98, 511–528.

Nwogu, O., 1993. Alternative form of boussinesq equations for nearshore wave propagation. Journal of waterway, port, coastal, and ocean engineering 119, 618–638. doi:10.1061/(ASCE)0733-950X(1993)119:6(618).

O'Donoghue, T., Wright, S., 2004a. Concentrations in oscillatory sheet flow for well sorted and graded sands. Coastal Engineering 50, 117–138. doi:10.1016/j.coastaleng.2003.09.004.

O'Donoghue, T., Wright, S., 2004b. Flow tunnel measurements of velocities and sand flux in oscillatory sheet flow for well-sorted and graded sands. Coastal Engineering 51, 1163–1184. doi:10.1016/j.coastaleng.2004.08.001.

Orszaghova, J., Borthwick, A.G., Taylor, P.H., 2012. From the paddle to the beach–a

boussinesq shallow water numerical wave tank based on madsen and sørensen's equations. Journal of Computational Physics 231, 328–344. doi:10.1016/j.jcp.2011.08.028.

Ouda, M., Toorman, E.A., 2019. Development of a new multiphase sediment transport model for free surface flows. International Journal of Multiphase Flow 117, 81–102. doi:10.1016/j.ijmultiphaseflow.2019.04.023.

Ozdemir, C.E., Hsu, T.J., Balachandar, S., 2010. A numerical investigation of fine particle laden flow in an oscillatory channel: the role of particle-induced density stratification. Journal of Fluid Mechanics 665, 1. doi:10.1017/S0022112010003769.

Packwood, A., 1983. The influence of beach porosity on wave uprush and backwash. Coastal Engineering 7, 29–40. doi:10.1016/0378-3839(83)90025-X.

Packwood, A.R., Peregrine, D.H., 1979. The propagation of solitary waves and bores over a porous bed. Coastal engineering 3, 221–242. doi:10.1016/0378-3839(79)90022-X.

Park, H., Tomiczek, T., Cox, D.T., van de Lindt, J.W., Lomonaco, P., 2017. Experimental modeling of horizontal and vertical wave forces on an elevated coastal structure. Coastal Engineering 128, 58–74. doi:10.1016/j.coastaleng.2017.08.001.

Parlange, J.Y., Brutsaert, W., 1987. A capillarity correction for free surface flow of groundwater. Water Resources Research 23, 805–808. doi:10.1029/WR023i005p00805.

Passalacqua, A., Fox, R.O., 2011. Implementation of an iterative solution procedure for multi-fluid gas–particle flow models on unstructured grids. Powder technology 213, 174–187. doi:10.1016/j.powtec.2011.07.030.

Passalacqua, A., Fox, R.O., 2012. Simulation of mono-and bidisperse gas-particle flow in a riser with a third-order quadrature-based moment method. Industrial & Engineering Chemistry Research 52, 187–198. doi:10.1021/ie300424m.

Peregrine, D.H., 1967. Long waves on a beach. Journal of fluid mechanics 27, 815–827. doi:10.1017/S0022112067002605.

Perera, E., Zhu, F., Dodd, N., Briganti, R., Blenkinsopp, C., Turner, I.L., 2019. Surface-groundwater flow numerical model for barrier beach with exfiltration incorporated bottom boundary layer model. Coastal Engineering 146, 47–64. doi:10.1016/j.coastaleng.2018.12.002.

Petti, M., Longo, S., 2001. Turbulence experiments in the swash zone. Coastal Engineering 43, 1–24. doi:10.1016/S0378-3839(00)00068-5.

Pezza, D.A., White, J.M., 2021. Impact of the duration of coastal flooding on infrastructure. Public Works Management & Policy 26, 144–163. doi:10.1177/1087724X20915918.

Pintado-Patiño, J.C., Torres-Freyermuth, A., Puleo, J.A., Pokrajac, D., 2015. On the role of infiltration and exfiltration in swash zone boundary layer dynamics. Journal of Geophysical Research: Oceans 120, 6329–6350. doi:doi.org/10.1002/2015JC010806.

Poate, T.G., McCall, R.T., Masselink, G., 2016. A new parameterisation for runup on gravel beaches. Coastal Engineering 117, 176–190. doi:10.1016/j.coastaleng.2016.08.003.

Pope, S.B., 2000. Turbulent Flows. Cambridge University Press.

Price, M., 1996. Introducing groundwater. Psychology Press.

Prime, T., Brown, J.M., Plater, A.J., 2015. Physical and economic impacts of sea-level rise and low probability flooding events on coastal communities. PLoS One 10, e0117030. doi:10.1371/journal.pone.0117030.

Pugh, F.J., Wilson, K.C., 1999. Velocity and concentration distributions in sheet flow above plane beds. Journal of Hydraulic Engineering 125, 117–125. doi:10.1061/(ASCE)0733-9429(1999)125:2(117).

Puleo, J., Beach, R., Holman, R.A., Allen, J., 2000. Swash zone sediment suspension and transport and the importance of bore-generated turbulence. Journal of Geophysical Research: Oceans 105, 17021–17044. doi:10.1029/2000JC900024.

Puleo, J.A., Farhadzadeh, A., Kobayashi, N., 2007. Numerical simulation of swash zone fluid accelerations. Journal of Geophysical Research: Oceans 112. doi:10.1029/2006JC004084.

Puleo, J.A., Holland, K.T., 2001. Estimating swash zone friction coefficients on a sandy beach. Coastal engineering 43, 25–40. doi:10.1016/S0378-3839(01)00004-7.

Puleo, J.A., Holland, K.T., Slinn, D.N., Smith, E., Webb, B.M., 2002. Numerical modelling of swash zone hydrodynamics, in: Coastal Engineering 2002: Solving Coastal Conundrums. World Scientific, pp. 968–979. doi:10.1142/9789812791306_0082.

Puleo, J.A., Krafft, D., Pintado-Patiño, J.C., Bruder, B., 2017. Video-derived near bed and sheet flow sediment particle velocities in dam-break-driven swash. Coastal Engineering 126, 27–36. doi:10.1016/j.coastaleng.2017.04.008.

Puleo, J.A., Lanckriet, T., Wang, P., 2012. Near bed cross-shore velocity profiles, bed shear stress and friction on the foreshore of a microtidal beach. Coastal Engineering 68, 6–16. doi:10.1016/j.coastaleng.2012.04.007.

Raubenheimer, B., Elgar, S., Guza, R., 2004. Observations of swash zone velocities: A note on friction coefficients. Journal of Geophysical Research: Oceans 109. doi:10.1029/2003JC001877.

Raubenheimer, B., Guza, R., 1996. Observations and predictions of run-up. Journal of Geophysical Research: Oceans 101, 25575–25587. doi:10.1029/96JC02432.

Raubenheimer, B., Guza, R., Elgar, S., 1999. Tidal water table fluctuations in a sandy ocean beach. Water Resources Research 35, 2313–2320. doi:10.1029/1999WR900105.

Rego, J.L., Li, C., 2010. Nonlinear terms in storm surge predictions: Effect of tide and shelf geometry with case study from hurricane rita. Journal of Geophysical Research: Oceans 115. doi:10.1029/2009JC005285.

Ribberink, J.S., 1998. Bed-load transport for steady flows and unsteady oscillatory flows. Coastal Engineering 34, 59–82. doi:10.1016/S0378-3839(98)00013-1.

Ribberink, J.S., Al-Salem, A.A., 1994. Sediment transport in oscillatory boundary layers in cases of rippled beds and sheet flow. Journal of Geophysical Research: Oceans 99, 12707–12727. doi:10.1029/94JC00380.

Ribberink, J.S., Al-Salem, A.A., 1995. Sheet flow and suspension of sand in oscillatory boundary layers. Coastal engineering 25, 205–225. doi:10.1016/0378-3839(95)00003-T.

Ribberink, J.S., van der Werf, J.J., O'Donoghue, T., Hassan, W., 2008. Sand motion induced by oscillatory flows: Sheet flow and vortex ripples. Journal of Turbulence 9, N20. doi:10.1080/14685240802220009.

Robinson, C., Baldock, T., Horn, D., Gibbes, B., Hughes, M., Nielsen, P., Li, L., 2006. Measurement of groundwater and swash interactions on a sandy beach, in: Coastal Dynamics 2005: State of the Practice, pp. 1–12. doi:10.1061/40855(214)104.

Rodi, W., 1993. Turbulence models and their application in hydraulics. CRC Press.

Roelvink, D., Reniers, A., Van Dongeren, A., De Vries, J.V.T., McCall, R., Lescinski, J., 2009. Modelling storm impacts on beaches, dunes and barrier islands. Coastal engineering 56, 1133–1152. doi:10.1016/j.coastaleng.2009.08.006.

Roelvink, J.A., Brøker, I., 1993. Cross-shore profile models. Coastal Engineering 21, 163–191. doi:10.1016/0378-3839(93)90049-E.

Rotzoll, K., El-Kadi, A.I., 2008. Estimating hydraulic properties of coastal aquifers using wave setup. Journal of Hydrology 353, 201–213. doi:10.1016/j.jhydrol.2008.02.005.

Rotzoll, K., Fletcher, C.H., 2013. Assessment of groundwater inundation as a consequence of sea-level rise. Nature Climate Change 3, 477. doi:10.1038/nclimate1725.

Ruessink, B., Blenkinsopp, C., Brinkkemper, J., Castelle, B., Dubarbier, B., Grasso, F., Puleo, J., Lanckriet, T., 2016. Sandbar and beach-face evolution on a prototype coarse sandy barrier. Coastal Engineering 113, 19–32. doi:10.1016/j.coastaleng.2015.11.005.

Ruessink, B., Kuriyama, Y., Reniers, A., Roelvink, J., Walstra, D., 2007. Modeling cross-shore sandbar behavior on the timescale of weeks. Journal of Geophysical Research: Earth Surface 112. doi:10.1029/2006JF000730.

Ruggiero, P., Holman, R.A., Beach, R., 2004. Wave run-up on a high-energy dissipative beach. Journal of Geophysical Research: Oceans 109. doi:10.1029/2003JC002160.

Rusche, H., 2003. Computational fluid dynamics of dispersed two-phase flows at high phase fractions. Ph.D. thesis. Imperial College London (University of London).

Schretlen, J.L.M., 2012. Sand transport under full-scale progressive surface waves. Ph.D. thesis. University of Twente, Netherlands.

Scott, C.P., Cox, D.T., Maddux, T.B., Long, J.W., 2005. Large-scale laboratory observations of turbulence on a fixed barred beach. Measurement Science and Technology 16, 1903. doi:10.1088/0957-0233/16/10/004.

Scott, N.V., Hsu, T.J., Cox, D., 2009. Steep wave, turbulence, and sediment concentration statistics beneath a breaking wave field and their implications for sediment transport. Continental Shelf Research 29, 2303–2317. doi:10.1016/j.csr.2009.09.008.

Shao, S., Ji, C., Graham, D.I., Reeve, D.E., James, P.W., Chadwick, A.J., 2006. Simulation of wave overtopping by an incompressible sph model. Coastal engineering 53, 723–735. doi:10.1016/j.coastaleng.2006.02.005.

Shi, F., Kirby, J.T., Harris, J.C., Geiman, J.D., Grilli, S.T., 2012. A high-order adaptive time-stepping tvd solver for boussinesq modeling of breaking waves and coastal inundation. Ocean Modelling 43, 36–51. doi:10.1016/j.ocemod.2011.12.004.

Shiach, J.B., Mingham, C.G., Ingram, D.M., Bruce, T., 2004. The applicability of the shallow water equations for modelling violent wave overtopping. Coastal Engineering 51, 1–15. doi:10.1016/j.coastaleng.2003.11.001.

Shields, A., 1936. Application of similarity principles and turbulence research to bed-load movement. Ph.D. thesis. Technical University, Berlin.

Shih, T.H., Povinello, L.A., Lumley, J.L., 1999. A generalized wall function. Technical Report. National Aeronautics and Space Administration.

Simonin, O., 1991. Prediction of the dispersed phase turbulence in particle-laden jets, in: Proceedings of the 4th International Symposium on Gas-Solid Flows, ADME FED. pp. 197–206.

Sleath, J.F.A., 1987. Turbulent oscillatory flow over rough beds. Journal of Fluid Mechanics 182, 369–409. doi:10.1017/S0022112087002374.

Smit, P., Janssen, T., Holthuijsen, L., Smith, J., 2014. Non-hydrostatic modeling of surf zone wave dynamics. Coastal Engineering 83, 36–48. doi:10.1016/j.coastaleng.2013.09.005.

Soulsby, R.L., Damgaard, J.S., 2005. Bedload sediment transport in coastal waters. Coastal Engineering 52, 673–689. doi:10.1016/j.coastaleng.2005.04.003.

Sous, D., Lambert, A., Rey, V., Michallet, H., 2013. Swash–groundwater dynamics in a sandy beach laboratory experiment. Coastal engineering 80, 122–136. doi:10.1016/j.oceaneng.2009.03.003.

Srivastava, A., Sundaresan, S., 2003. Analysis of a frictional–kinetic model for gas–particle flow. Powder technology 129, 72–85. doi:10.1016/S0032-5910(02)00132-8.

Stansby, P.K., 2003. Solitary wave run up and overtopping by a semi-implicit finite-volume shallow-water boussinesq model. Journal of Hydraulic Research 41, 639–647. doi:10.1080/00221680309506896.

Steenhauer, K., Pokrajac, D., O'Donoghue, T., Kikkert, G.A., 2011. Subsurface processes generated by bore-driven swash on coarse-grained beaches. Journal of Geophysical Research: Oceans 116. doi:10.1029/2010JC006789.

Sumer, B.M., Kozakiewicz, A., Fredsøe, J., Deigaard, R., 1996. Velocity and concentration profiles in sheet-flow layer of movable bed. Journal of Hydraulic Engineering 122, 549–558. doi:10.1061/(ASCE)0733-9429(1996)122:10(549).

Suzuki, T., Altomare, C., Veale, W., Verwaest, T., Trouw, K., Troch, P., Zijlema, M., 2017. Efficient and robust wave overtopping estimation for impermeable coastal structures in shallow foreshores using swash. Coastal Engineering 122, 108–123. doi:10.1016/j.coastaleng.2017.01.009.

Swart, D.H., 1974. Offshore sediment transport and equilibrium beach profiles. Delft Hydraulics Laboratory Publication No. 131.

Sweby, P.K., 1984. High resolution schemes using flux limiters for hyperbolic conservation laws. SIAM journal on numerical analysis 21, 995–1011. doi:10.1137/0721062.

Taherkhani, M., Vitousek, S., Barnard, P.L., Frazer, N., Anderson, T.R., Fletcher, C.H., 2020. Sea-level rise exponentially increases coastal flood frequency. Scientific reports 10, 1–17. doi:10.1038/s41598-020-62188-4.

Thomas, A., Dietrich, J., Asher, T., Bell, M., Blanton, B., Copeland, J., Cox, A., Dawson, C., Fleming, J., Luettich, R., 2019. Influence of storm timing and forward speed on tides

and storm surge during hurricane matthew. Ocean Modelling 137, 1–19. doi:10.1016/j.ocemod.2019.03.004.

Thomas, S., Cox, D., 2012. Influence of finite-length seawalls for tsunami loading on coastal structures. Journal of waterway, port, coastal, and ocean engineering 138, 203–214. doi:10.1061/(ASCE)WW.1943-5460.0000125.

Tissier, M., Bonneton, P., Marche, F., Chazel, F., Lannes, D., 2012. A new approach to handle wave breaking in fully non-linear boussinesq models. Coastal Engineering 67, 54–66. doi:10.1016/j.coastaleng.2012.04.004.

Titov, V.V., Synolakis, C.E., 1995. Modeling of breaking and nonbreaking long-wave evolution and runup using vtcs-2. Journal of Waterway, Port, Coastal, and Ocean Engineering 121, 308–316. doi:10.1061/(ASCE)0733-950X(1995)121:6(308).

Tonelli, M., Petti, M., 2009. Hybrid finite volume–finite difference scheme for 2dh improved boussinesq equations. Coastal Engineering 56, 609–620. doi:10.1016/j.coastaleng.2009.01.001.

Tonelli, M., Petti, M., 2012. Shock-capturing boussinesq model for irregular wave propagation. Coastal Engineering 61, 8–19. doi:10.1016/j.coastaleng.2011.11.006.

Torres-Freyermuth, A., Puleo, J.A., Pokrajac, D., 2013. Modeling swash-zone hydrodynamics and shear stresses on planar slopes using reynolds-averaged navier–stokes equations. Journal of Geophysical Research: Oceans 118, 1019–1033. doi:10.1002/jgrc.20074.

Trowbridge, J., Kineke, G., 1994. Structure and dynamics of fluid muds on the amazon continental shelf. Journal of Geophysical Research: Oceans 99, 865–874. doi:10.1029/93JC02860.

Trowbridge, J., Young, D., 1989. Sand transport by unbroken water waves under sheet

flow conditions. Journal of Geophysical Research: Oceans 94, 10971–10991. doi:10.1029/JC094iC08p10971.

Turner, I., 1993. The total water content of sandy beaches. Journal of Coastal Research , 11–26.

Turner, I.L., Coates, B.P., Acworth, R.I., 1997a. Tides, waves and the super-elevation of groundwater at the coast. Journal of Coastal Research , 46–60.

Turner, I.L., Coates, B.P., Acworth, R.I., 1997b. Tides, waves and the super-elevation of groundwater at the coast. Journal of Coastal Research , 46–60.

Turner, I.L., Masselink, G., 1998. Swash infiltration-exfiltration and sediment transport. Journal of Geophysical Research: Oceans 103, 30813–30824. doi:10.1029/98JC02606.

Turner, I.L., Nielsen, P., 1997. Rapid water table fluctuations within the beach face: Implications for swash zone sediment mobility? Coastal Engineering 32, 45–59. doi:10.1016/S0378-3839(97)00015-X.

Van Der Ham, R., Fontijn, H.L., Kranenburg, C., Winterwerp, J.C., 2001. Turbulent exchange of fine sediments in a tidal channel in the ems/dollard estuary. part i: Turbulence measurements. Continental Shelf Research 21, 1605–1628. doi:10.1016/S0278-4343(01)00010-3.

Van Der Zanden, J., Alsina, J.M., Cáceres, I., Buijsrogge, R.H., Ribberink, J.S., 2015. Bed level motions and sheet flow processes in the swash zone: Observations with a new conductivity-based concentration measuring technique (ccm+). Coastal Engineering 105, 47–65. doi:10.1016/j.coastaleng.2015.08.009.

Van Rijn, L., Tonnon, P., Sánchez-Arcilla, A., Cáceres, I., Grüne, J., 2011. Scaling laws for beach and dune erosion processes. Coastal Engineering 58, 623–636. doi:10.1016/j.coastaleng.2011.01.008.

Van Rijn, L.C., 1984. Sediment transport, part iii: bed forms and alluvial roughness. Journal of Hydraulic Engineering 110, 1733–1754. doi:10.1061/(ASCE)0733-9429(1984)110:12(1733).

Van Rijn, L.C., 1987. Mathematical modelling of morphological processes in the case of suspended sediment transport. Ph.D. thesis. Delft University of Technology.

Van Rijn, L.C., 2007. Unified view of sediment transport by currents and waves. i: Initiation of motion, bed roughness, and bed-load transport. Journal of Hydraulic Engineering 133, 649–667. doi:10.1061/(ASCE)0733-9429(2007)133:6(649).

Van Rijn, L.C.V., Ribberink, J.S., Werf, J.V.D., Walstra, D.J.R., 2013. Coastal sediment dynamics: recent advances and future research needs. Journal of Hydraulic Research 51, 475–493. doi:10.1080/00221686.2013.849297.

Villarroel-Lamb, D., Hammeken, A., Simons, R., 2014. Quantifying the effect of bed permeability on maximum wave runup, in: 34th International Conference on Coastal Engineering, Seoul, South Korea.

Vitousek, S., Barnard, P.L., Fletcher, C.H., Frazer, N., Erikson, L., Storlazzi, C.D., 2017. Doubling of coastal flooding frequency within decades due to sea-level rise. Scientific reports 7, 1–9. doi:10.1038/s41598-017-01362-7.

Von Kármán, T., 1931. Mechanical similitude and turbulence. Technical Report 611. National Advisory Committee on Aeronautics.

Waddell, E., 1973. Dynamics of Swash and Implication to Beach Response. Technical Report. Louisiana State University Baton Rouge Coastal Studies Institute.

Waddell, E., 1976. Swash—groundwater—beach profile interactions. Beach and Nearshore Sedimentation 24, 115–125. doi:10.2110/pec.76.24.

Wahl, T., Jain, S., Bender, J., Meyers, S.D., Luther, M.E., 2015. Increasing risk of compound flooding from storm surge and rainfall for major us cities. Nature Climate Change 5, 1093–1097. doi:10.1038/nclimate2736.

Wang, Y.H., 2007. Formula for predicting bedload transport rate in oscillatory sheet flows. Coastal Engineering 54, 594–601. doi:10.1016/j.coastaleng.2006.12.003.

Wang, Y.H., Yu, G.H., 2007. Velocity and concentration profiles of particle movement in sheet flows. Advances in Water Resources 30, 1355–1359. doi:10.1016/j.advwatres.2006.11.012.

Watanabe, Y., Saeki, H., 1999. Three-dimensional large eddy simulation of breaking waves. Coastal Engineering Journal 41, 281–301. doi:10.1142/S0578563499000176.

Watson, G., Barnes, T., Peregrine, D., 1995. The generation of low-frequency waves by a single wave group incident on a beach, in: Coastal Engineering 1994, pp. 776–790. doi:10.1061/9780784400890.058.

Weller, H.G., 2008. A new approach to vof-based interface capturing methods for incompressible and compressible flow. OpenCFD Ltd., Report TR/HGW 4, 35.

Werner, A.D., Lockington, D.A., 2003. Influence of hysteresis on tidal capillary fringe dynamics in a well-sorted sand. Advances in Water Resources 26, 1199–1204. doi:10.1016/S0309-1708(03)00107-6.

Whiting, P.J., Dietrich, W.E., Leopold, L.B., Drake, T.G., Shreve, R.L., 1988. Bedload sheets in heterogeneous sediment. Geology 16, 105–108. doi:10.1130/0091-7613(1988)016<0105:BSIHS>2.3.CO;2.

Willmott, C.J., 1981. On the validation of models. Physical geography 2, 184–194. doi:10.1080/02723646.1981.10642213.

Wilson, K.C., 1989. Friction of wave-induced sheet flow. Coastal Engineering 12, 371–379. doi:10.1016/0378-3839(89)90013-6.

Wilson, K.C., 2005. Rapid increase in suspended load at high bed shear. Journal of Hydraulic Engineering 131, 46–51. doi:10.1061/(ASCE)0733-9429(2005)131:1(46).

Wu, Y.T., Higuera, P., Liu, P.L.F., 2021. On the evolution and runup of a train of solitary waves on a uniform beach. Coastal Engineering 170, 104015. doi:10.1016/j.coastaleng.2021.104015.

Yin, J., Yu, D., Lin, N., Wilby, R.L., 2017. Evaluating the cascading impacts of sea level rise and coastal flooding on emergency response spatial accessibility in lower manhattan, new york city. Journal of Hydrology 555, 648–658.

Yu, X., Hsu, T.J., Hanes, D.M., 2010. Sediment transport under wave groups: Relative importance between nonlinear waveshape and nonlinear boundary layer streaming. Journal of Geophysical Research: Oceans 115. doi:10.1029/2009JC005348.

Yu, Z., Niemeyer, H.D., Bakker, W.T., 1990. Site investigation on sand concentration in the sheet-flow layer, in: Proceedings of the 22nd International Conference on Coastal Engineering, American Society of Civil Engineers. pp. 2360–2371. doi:10.1061/9780872627765.180.

Zhang, Q., Liu, P.L.F., 2008. A numerical study of swash flows generated by bores. Coastal Engineering 55, 1113–1134. doi:10.1016/j.coastaleng.2008.04.010.

Zhao, Q., Tanimoto, K., 1999. Numerical simulation of breaking waves by large eddy simulation and vof method, in: Coastal Engineering 1998, pp. 892–905. doi:10.1061/9780784404119.066.

Zhou, Z., Hsu, T.J., Cox, D., Liu, X., 2017. Large-eddy simulation of wave-breaking in-

duced turbulent coherent structures and suspended sediment transport on a barred beach. Journal of Geophysical Research: Oceans 122, 207–235. doi:10.1002/2016JC011884.

Zijlema, M., Stelling, G., Smit, P., 2011. Swash: An operational public domain code for simulating wave fields and rapidly varied flows in coastal waters. Coastal Engineering 58, 992–1012. doi:10.1016/j.coastaleng.2011.05.015.

Zscheischler, J., Westra, S., Van Den Hurk, B.J., Seneviratne, S.I., Ward, P.J., Pitman, A., AghaKouchak, A., Bresch, D.N., Leonard, M., Wahl, T., et al., 2018. Future climate risk from compound events. Nature Climate Change 8, 469–477. doi:10.1038/s41558-018-0156-3.